DENSITY FUNCTIONAL THEORY AND MOLECULAR DYNAMICS
SIMULATIONS OF CARBON NANOTUBES, POLYETHERETHERKETONE
AND THEIR INTERFACES

A THESIS SUBMITTED TO
THE GRADUATE SCHOOL OF NATURAL AND APPLIED SCIENCES
OF
MIDDLE EAST TECHNICAL UNIVERSITY

BY

GÖZDENUR TORAMAN

IN PARTIAL FULFILLMENT OF THE REQUIREMENTS
FOR
THE DEGREE OF MASTER OF SCIENCE
IN
PHYSICS

AUGUST 2018

Approval of the thesis:

DENSITY FUNCTIONAL THEORY AND MOLECULAR DYNAMICS SIMULATIONS OF CARBON NANOTUBES, POLYETHERETHERKETONE AND THEIR INTERFACES

submitted by **GÖZDENUR TORAMAN** in partial fulfillment of the requirements for the degree of **Master of Science in Physics Department, Middle East Technical University** by,

Prof. Dr. Halil Kalıpçılar
Dean, Graduate School of **Natural and Applied Sciences**   _____

Prof. Dr. Altuğ Özpineci
Head of Department, **Physics**   _____

Assoc. Prof. Dr. Hande Toffoli
Supervisor, **Physics Department, METU**   _____

Assoc. Prof. Dr. Ercan Gürses
Co-supervisor, **Aerospace Engineering Dept., METU**   _____

Examining Committee Members:

Assoc. Prof. Dr. Emine Deniz Tekin
Mechanical Engineering Department, THK University   _____

Assoc. Prof. Dr. Hande Toffoli
Physics Department, METU   _____

Assoc. Prof. Dr. Ercan Gürses
Aerospace Engineering Department, METU   _____

Assoc. Prof. Dr. Alpan Bek
Physics Department, METU   _____

Assoc. Prof. Dr. Demirkan Çöker
Aerospace Engineering Department, METU   _____

Date: _____

I hereby declare that all information in this document has been obtained and presented in accordance with academic rules and ethical conduct. I also declare that, as required by these rules and conduct, I have fully cited and referenced all material and results that are not original to this work.

Name, Last Name: GÖZDENUR TORAMAN

Signature   :

ABSTRACT

DENSITY FUNCTIONAL THEORY AND MOLECULAR DYNAMICS SIMULATIONS OF CARBON NANOTUBES, POLYETHERETHERKETONE AND THEIR INTERFACES

Toraman, Gözdenur

M.S., Department of Physics

Supervisor : Assoc. Prof. Dr. Hande Toffoli

Co-Supervisor : Assoc. Prof. Dr. Ercan Gürses

August 2018, 109 pages

Carbon nanotubes are allotropes of carbon with a cylindrical nanostructure. A nanotube can roughly be described as a rolled-up graphene sheet, which is a two dimensional hexagonal arrangement of carbon atoms, often referred to as a honeycomb lattice. Carbon nanotubes, much like their parent material graphene, are characterized by high strength, high Young modulus, durability and tunable electronic behavior. As a result of these superior properties, CNTs have been used in diverse technologically relevant applications over the decades since their successful synthesis. In particular, CNT-polymer composites have gained considerable interest in the materials research community in recent years. The testing, manipulating and design of viable mixtures of nanotubes and polymers presents challenges from an experimental point of view. For this reason, numerical modeling of nanotubes and nanotube reinforced polymers is important.

The main objective of this thesis is to examine mechanical properties of carbon nanotubes, Poly Ether Ether Ketone (PEEK) polymer and physical properties of their

interface by using Density Functional Theory (DFT) and Molecular Dynamics (MD) techniques. PEEK is a semi-crystalline thermoplastic polymer which has remarkable mechanical properties with a Young modulus of 3.6 GPa and a rather high melting temperature $\sim 370°C$ (when it is reinforced with CNTs this melting point can reach $390°C$). Thanks to these properties, PEEK is suitable for use in extreme conditions, such as spacecraft, nuclear power plants, petroleum and geothermal wells.

Keywords: Carbon Nanotubes, Polymer, Interface, Molecular Dynamics, Density Functional Theory

ÖZ

KARBON NANOTÜPLERİN, POLİETERETERKETON VE ARAYÜZLERİNİN YOĞUNLUK FONKSİYONELİ TEORİSİ VE MOLEKÜLER DİNAMİK SİMULASYONLARI

Toraman, Gözdenur

Yüksek Lisans, Fizik Bölümü

Tez Yöneticisi   : Doç. Dr. Hande Toffoli

Ortak Tez Yöneticisi   : Doç. Dr. Ercan Gürses

Ağustos 2018 , 109 sayfa

Silindirik nanoyapısı ile karbon elementinin bir allotropu olan karbon nanotüpler, 2 boyutlu karbon atomlarının altıgen şeklinde dizilmesiyle oluşan bir grafen katmanının, silindir şeklinde bükülerek uçlarının birleştirildiği bir yapı olarak da tanımlanabilir. Karbon nanotüpler tıpkı ana malzemesi olan grafen gibi sağlam bir malzeme olup yüksek elastisite modülüsüne ve ayarlanabilir elektronik özelliklere sahiptir. Bu üstün özellikleri ve başarılı bir şekilde sentezlenebilmesi KNTleri son yıllarda geniş teknoloji uygulamalarında kullanılabilir bir malzeme yapmaktadır. Özellikle, son yıllarda karbon nanotüp-polimer kompozitler malzeme araştırma komünitelerince büyük önem kazanmıştır. Deneysel açıdan test edilmesi, üretilmesi ve nanotüp-polimer karışımlarının uygulanması bazı zorluklar içerdiğinden, nanotüplerin ve nanotüplerle güçlendirilmiş polimer kompozitlerin nümerik modellemesi büyük önem taşımaktadır.

Bu tezin temel amacı, karbon nanotüplerin ve Poli Eter Eter Keton (PEEK) polimerinin mekanik özelliklerini, bunun yanı sıra KNT/PEEK arayüz etkileşimlerinin doğasını,

Yoğunluk Fonksiyoneli Teorisi (YFT) ve Moleküler Dinamik (MD) tekniği kullanarak incemelektir. PEEK polimeri 3.6 GPa seviyelerinde yüksek elastisite modülüne ve $\sim 370°C$ gibi yüksek erime sıcaklığına sahip olan (bu değer KNTler ile güçlendirildiğinde 390°C seviyelerine ulaşabilmektedir) termoplastik bir malzeme olup, bu özellikleri sayesinde uzay araçları, nükleer reaktörler, petrol ve jeotermal kuyular gibi zorlu koşullarda kullanıma uygundur.

Anahtar Kelimeler: Karbon Nanotüpler, Polimer, Arayüz, Moleküler Dinamik, Yoğunluk Fonksiyoneli Teorisi

To my dear family

ACKNOWLEDGMENTS

I owe a very deep gratitude to my uncle Serkan Toraman and his lovely wife Seray Toraman for their guidance and support in every aspect of my life. Without their help, I could not achieve.

The final and the biggest thanks go to my parents Gül and Serdar Toraman and my brother Gökay for their endless support, love and encouragement throughout my whole life. I am very lucky to have such a great family.

So long and thanks for all the fish..

TABLE OF CONTENTS

LIST OF TABLES

TABLES

xvii

LIST OF FIGURES

FIGURES

xxiii

LIST OF ABBREVIATIONS

AIREBO   Adaptive Intermolecular Reactive Emprical Bond Order

CNT   Carbon Nanotube

DFT   Density Functional Theory

GGA   Generalized Gradient Approximation

FF   Force Field

fs   femtosecond

LDA   Local Density Approximation

LJ   Lennard-Jones

MC   Monte Carlo

MD   Molecular Dynamics

ns   nanosecond

NH   Nosé-Hoover

PBE   Perdew-Burke-Ernzerhof

PEEK   Polyetheretherketone

ps   picosecond

ReaxFF   Reactive Force Field

Ryd   Rydberg

QM   Quantum Mechanics

CHAPTER 1

INTRODUCTION

Among the many allotropes of carbon, graphene [1] and CNT [2] are considered as breakthrough discoveries in materials community based upon their remarkable thermal, electronical and mechanical properties. They can be used in various applications in different disciplines such as device technology [3], drug delivery [4], field emission [5, 6], air and water filtration. Because of their light weight nature, extraordinary elastic and electronic properties, they also serve as additives to improve various properties of different matrices. Of particular importance is the CNT/polymer composites that find increasing use in the aerospace industry [7]. In this chapter, we introduce the two component of these composites, namely CNT and polymers. As carbon nanotubes originate structurally from graphene, we also briefly present structural properties of graphene.
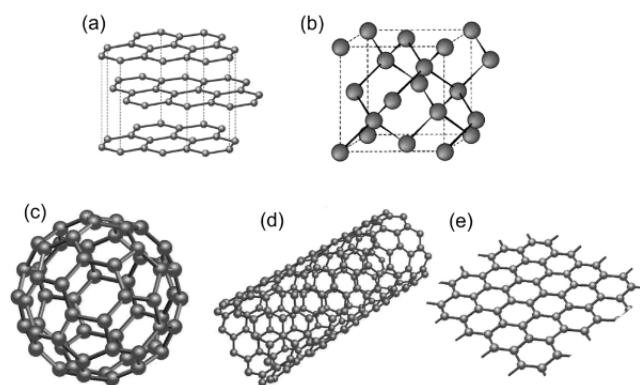
Figure 1.1: Structural forms of carbon. (a) graphite, (b) diamond, (c) fullerene, (d) CNT and (e) graphene. Reprinted from [3]

1.1 Graphene and Carbon Nanotubes(CNTs)

1.1.1 Graphene

Graphene is a 2D allotrope of carbon that has a honeycomb lattice structure due to sp^2 hybridization carbon of atoms. Because of their extraordinary mechanical properties, graphene and graphene-based materials are used in composite materials as reinforcement.
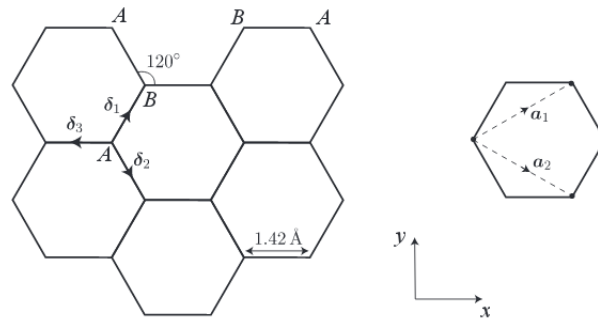
Figure 1.2: Honeycomb lattice structure of graphene sheet

In Figure 1.2 , $\vec{a}_1$ and $\vec{a}_2$ are lattice vectors of graphene sheet

$$\vec{a}_1 = \frac{a}{2}(3, \sqrt{3})$$
$$\vec{a}_2 = \frac{a}{2}(3, -\sqrt{3})$$

where a is the bond length between two carbon atoms ($\approx$ 1.42 Å) . Reciprocal lattice vectors of this graphene sheet satisfy the condition

$$\vec{a}_i \cdot \vec{b}_j = 2\pi\delta_{ij}$$

and given as

$$\vec{b}_1 = \frac{2\pi}{3a}(1, \sqrt{3})$$
$$\vec{b}_2 = \frac{2\pi}{3a}(1, -\sqrt{3})$$

2

Graphene not only has excellent mechanical properties (Young's modulus $\approx$ 1 TPa) but also has remarkable thermal conductivity in the order of 5000 M/mk [8] high electron mobility at room temperature (250,000 cm^2/V s) [9], good electrical conductivity. This variety of exceptional properties make graphene a viable nominee for plenty of potential applications such as reinforcing agents in composite materials [10], solar cells [11, 12], sensors, electronic circuits, display screens.

There are numerous experimental and computational studies in literature that concern mechanical properties of graphene. Lee and co-workers [14] investigated elastic properties of mono-layer graphene by nanoindentation in an atomic force microscope and reported Young's modulus of 1.0 TPa. Besides, Jiang et al [15] studied same properties by using molecular dynamics (MD) and reported Young's modulus results of graphene increasing from 0.95 to 1.1 TPa with increasing size and it shows very good agreement with the ones in experiment done by Lee and co-workers.

1.1.2   Carbon Nanotubes (CNTs)

Carbon nanotubes (CNTs) are 1D allotropes of carbon discovered by Iijima in 1991 [2]. Their cylindrical structure can roughly be visualized as a rolled-up graphene sheet, which is a two-dimensional hexagonal arrangement of carbon atoms, often referred to as a honeycomb lattice. The diameter of these CNTs is on the order of a nanometer, while their length can extend to several micrometers. CNTs, much like their parent material graphene, are characterized by high strength, high Young's modulus, durability and tunable electronic behavior.

As a result of these superior properties, CNTs have attrached considerable attention from the materials community. They have been used in various applications in many different scientific disciplines, such as energy storage, memory chips, sensors, biological applications [13]. In addition to these, CNTs are commonly used as reinforcements in composite materials. Especially, in the field of aviation, CNT reinforced polymer composites are important because of their light-weight nature, high stiffness and axial strength. CNTs are therefore a very powerful candidate for future aircraft and space vehicles. For instance, in 2012, NASA published a roadmap for future potential usage of nanomaterials especially CNTs [16] where the impacts of nanotechnology in aeronautics, planetary science, and space exploration are mentioned.

They emphasize the imminent advantages of utilizing CNTs such as reduced vehicle mass, improved functionality and durability, enhanced damage tolerance, improved self-healing characteristics, enhanced thermal protection, and control.

Due to its remarkable properties and potential applications, a large body of research has been dedicated to the mechanical properties of CNTs. Nonetheless, there is sizable scatter in the results depending on methods used and parameters such as chirality, aspect ratio (length / diamater) of tube, wall thickness/number. Treacy et al. [19] studied Young's modulus of eleven different CNTs with different aspect ratio by using transmission electron microscopy (TEM) and reported average Young's modulus as 1.8 TPa which is several times higher than that of diamond. Another study conducted by Wong et al. [20] by using AFM tips found a Young's modulus value of MWCNTs 1.287 ± 0.59 TPa. Apart from the experimental studies, there are also computational ones in literature that consider mechanical properties of CNTs. Young's modulus results in computational studies range from 0.5 to 5 TPa by using different methods such as Molecular Dynamics (MD), emprical force constant model, density functional theory (DFT) and tight-binding model [21].

1.1.2.1   Classification of CNTs

CNTs are divided into three groups according to their chirality; zig-zag, armchair and chiral. In simple terms, chirality can be defined as the angle with which the graphene sheet is rolled up into a CNT. Chiral vector of a CNT is defined as

$$\vec{C}_h = n\vec{a}_1 + m\vec{a}_2$$

where n and m are integers. The angle between $\vec{a}_1$ and $\vec{a}_2$, chiral angle designated by n and m values determines the type of CNT i.e. the applying simple geometric considerations, the chiral angle of a CNT can be calculated as

$$tan\theta = \frac{n - m}{\sqrt{3}(n + m)}$$
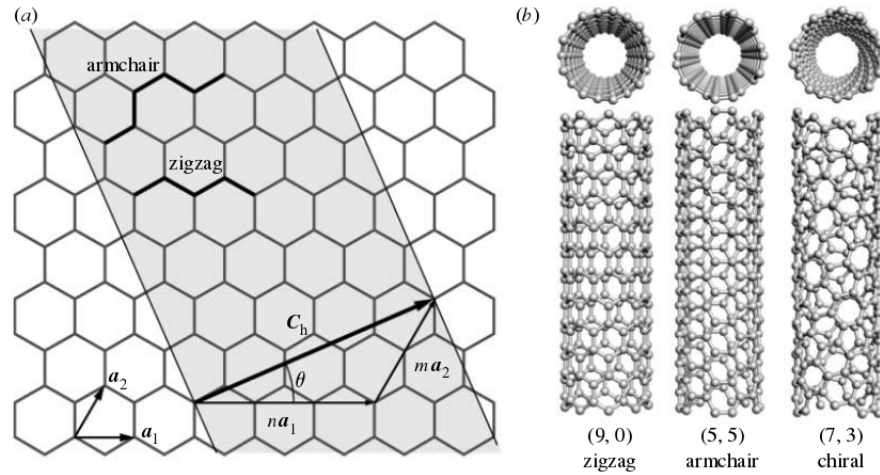
Figure 1.3: (a) Chiral vector and chiral angle, (b) three types of CNTs. Reprinted from [17]

Through similar considerations, the diameter of a CNT can also be calculated by using *n* and *m* :

$$d = \frac{a}{\pi}\sqrt{n^2 + m^2 + nm}$$

Chilarity of a CNT also determines its electronic properties. Due to discretization of the Bloch wave vector which arises because of the cyclic boundary conditions around the nanotube, for some chiralities the Fermi point of graphene does not coincide with any states. As a result, CNTs may display metallic or semiconducting properties. In particular, zigzag CNTs show metallic properties while armchair ones are semiconducting. In addition, for the chiral ones, when the difference between *n* and *m* is a multiple of three, CNT shows metallic properties.

The CNT fabrication process gives rise CNTs of different characters beyond conductivity. CNTs may be simple cylinders with a single wall, called single-walled nanotubes (SWCNTs) or may be composed of concentric cylinders forming multi-walled nanotubes (MWCNTs) like in Figure 1.4. In the case of MWCNTs, the walls are held together by van der Waals forces.

5

Figure 1.4: Single-walled and multi-walled CNTs. Reprinted from [18]

1.2 Polymers

Polymers are large molecular structures that consists of many repeated sub-units called monomers. The monomers vary in atomic number, number of atomic species involved and structural complexity, however, polymers are generally characterized by chain-like structures with carbon atoms in the backbone. They are low-density materials that have good corrosion resistance and low friction coefficient. Due to these properties and their well-established production techniques, polymers are very good candidates that can be used in different fields of industry. Polymers can be classified according to several different properties. According to their chemical structure, they may fall into the category of homopolymers and co-polymers. Homopolymers consist of a single type of monomer in the polymer chain while co-polymers consist of two or more different types. They are further categorized as linear, branched and cross-linked based on the spatial arrangement of the monomers. As it can be seen from Figure 1.5 (b), in branched polymers there is a side chain that is connected to the main chain while there is an interconnection between main chains in cross-linked polymers. Another classification of polymers is according to their tacticity. Tacticity is the sterochemical arrangement of the monomer units in a main polymer chain. In isotactic polymers, side groups of monomers line up on the same plane whereas in atactic polymers they have irregular arrangement. For the syndiotactic case, they are arranged in an alternating pattern. Figure 1.5 shows types of polymers (a) according to their chemical structure, (b) polymeric structure and (c) tacticity.

6
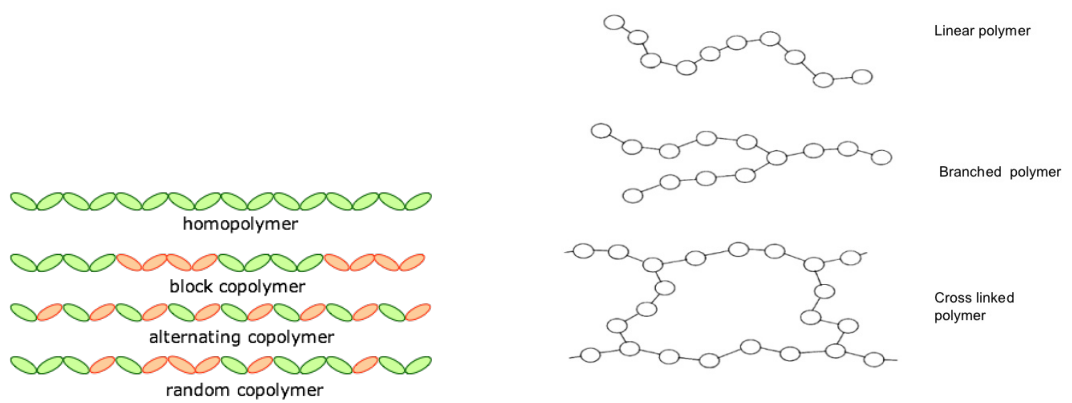
(a) according to chemical structure

(b) according to polymeric structure
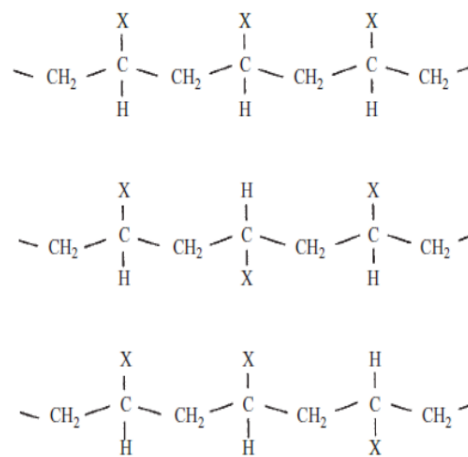
(c) according to arrangement of monomers. Respectively, isotactic, syndiotactic and atactic

Figure 1.5: Types of Polymers

Polymers are further classified according to their behaviour at high temperatures. Thermoplastic polymers melt at high temperatures and they solidify upon cooling. Therefore, they are reusable/recyclable and environment-friendly materials. Poly vinyl chloride (PVC), poly methyl methacrylate (PMMA), polyetylene (PE) are well known examples of thermoplastics. On the other hand, thermoset polymers do not show melting behaviour at high temperatures. Instead, the bonds between chains are stimulated and the material burns. The reason behind this behaviour of thermosets is that they possess high-degree of cross-linking that cause irreversible chemical reaction causing material's flame rather than melt. Epoxy resins, polyester resins and melamine resins are common examples of thermosetting polymers. Finally, elastomers are the types of polymers that have very weak inter-molecular forces, generally having low Young's modulus and high failure strain compared with other materials. The most common example for elastomers is rubber.

In our study, we choose a thermoplastic polymer which is called PEEK (Poly-Ether-Ether-Ketone) due to its excellent mechanical properties and environmental friendly nature. PEEK has been declared to have lowest smoke and poisonous gas emission of any other plastics [22]. It is a semi-crystalline, colorless, high-performance thermoplastic that has remarkable mechanical properties. Its commercial supplier Victrex Inc. reported its elastic modulus as 4.0 GPa. It also has relatively high melting point typically 370°C for unreinforced case and when it is reinforced this value reach to 390°C [22]. PEEK is suitable for use in harsh conditions such as nuclear power plants, geothermal wells and high-pressure steam valves [22]. It is also a biocompatible material and used in some medical applications such as prosthetics and dental fillings. Therefore, these extraordinary properties as well as its high fatigue resistance and resistance to radiation make PEEK an appropriate material to be used in aerospace applications. Based on these properties mentioned above, we decide PEEK as our matrix material to be used in CNT reinforced nanocomposite.

1.3 CNT/Polymer Nanocomposites

A composite material combines two or more different types of material. When are they combined, the resultant has properties different from their individual compo-

nents. Many composites consist of only two different types of materials; the material that makes up the bulk of the composite and hosts the other materials is referred to as the matrix while the materials that is added to modify the properties is called the dispersed material or reinforcement. In particular, nanocomposites are mixtures of matrix materials and strengthening agents with the latter having nanoscale dimension [23]. In the aerospace industry, there is great interest in structural materials that have low densities with good mechanical properties and resistance to corrosion. As it is challenging to find a single material to meet these demands, composite materials become popular in this industry. The main idea behind this type of materials is to improve combinations of mechanical properties such as stiffness, toughness, ambient and high-temperature strength [23] . Carbon fiber reinforced polymer composites (CFRPs) are one of the most popular types of composite materials due to their high stiffness and tensile strength and low weight. Typically, the diameters of carbon fibers are in the order of micro-meter. With the development of nanotechnology, carbon nanotubes gained considerable attention from materials community because they have higher strength-to-weight ratio than that of carbon fibers. Consequently, CNT/Polymer nanocomposites have begun to replace thicker fibers in aerospace industry because of their comparable mechanical properties and lightweight nature that increase fuel efficiency and reduce emissions [24] as mentioned earlier. With this growing interest in CNTs and their composites in different fields and experimental difficulties in measurements of their properties arising from their nano-scale dimensions, simulation of CNTs and their composites come into prominence [43]

In this thesis, we aim to investigate mechanical properties of CNTs and physical properties of CNT/Polymer interface to pave the way for creating a composite material to improve mechanical properties of the PEEK polymer matrix by using CNTs as reinforcement. First, the mechanical properties of CNTs are examined using Density Functional Theory (DFT) and Molecular Dynamics (MD). Following this initial stage, a series of MD simulations are performed on PEEK chains to test thermostats and interatomic potentials. Lastly, the physical properties of interface is investigated again by both DFT and MD approaches.

Methods that we used in the calculations will be discussed in Chapter 2 and results of the simulations will be given in the following chapters.

CHAPTER 2

METHODS

2.1 The Importance of Computer Simulations

Today, computer simulations act as a bridge between theory and experiment and they are crucial for understanding real world processes. One can test the accuracy of a theory by performing computer simulations on the same system. Also, with computer simulations, extreme conditions that are hard or even impossible to prepare in laborotaries such as very high temperatures and pressures can be tested [34]. Hence, computer simulations can also bring new perceptions into mechanisms of processes that may not be understood by real-time experiments. Even if sometimes it has some limitations, generally making simulations are cheaper and faster than performing experiments [35]. Performing experiments at the nano-scale to measure constitutive properties of systems such as Young's modulus, shear modulus and Poisson's ratio is a challenging issue and one can resort to computer simulations for the calculation of these material properties [36]. Various computer simulation techniques have been developed over the years to accommodate different length and time scales. These techniques range from the atomistic scale to the continuum scale. The complexity of computer simulations for materials properties increases with the desired level of accuracy. The density functional theory (DFT) method, for instance, yields accurate results for such properties as elastic, electronic, vibrational, magnetic properties since it explicity takes into account the electronic degrees of freedom. However, its high computational demand limits its applicability to only a few hundreds (up to thousand in the most optimistic case) atoms. Fortunately, in the case of elastic properties, methods of lower accuracy that make use of empirical potentials work almost as well.

In fact, the mechanical properties of materials have been modeled in the engineering community for decades using much less demanding continuum models [37, 38]. The combination of atomistic and continuum scale techniques provide a much more efficient way to investigate mechanical properties of nano-scaled systems [39]. Molecular Dynamics (MD) simulations are effective candidates to be used for this purpose at the nano-scale [40].

In this chapter, the two techniques that we use in this thesis, namely DFT and MD methods will be summarized briefly.

2.2 Density Functional Theory (DFT)

Density Functional Theory (DFT) is an ab-inito simulation technique for investigating properties of many-body systems that is based on electron density. The focus is shifted from the complex many-body wavefunction to the much simpler electronic density. In this section, this transition will be demonstrated starting from the many-particle Schrodinger equation and proceeding to the density via the so-called Kohn-Sham ansatz.

2.2.1 The Many-body Hamiltonian

In the quantum mechanical description of nature, it is thought that all desired knowledge about the system is stored in wave-function which is obtained as a solution of the Schrödinger equation. The Schrödinger equation in operator form can be written as

$$\hat{H}\Psi = E\Psi \tag{2.1}$$

where $\hat{H}$ corresponds to Hamiltonian of system, Ψ and E are the wavefunction and energy eigenvalue respectively. Many-body Hamiltonian of a system,

$$\hat{H} = \hat{T} + \hat{V} \tag{2.2}$$

is composed of the kinetic ($\hat{T}$) and potential ($\hat{V}$) terms. The potential term includes three types of interaction; *nucleus-nucleus*, *electron-electron* and *nucleus-electron*. Including two terms coming from kinetic energy of nuclei and electrons, many-body

Hamiltonian consists of five terms,

$$\hat{H} = \hat{T}_n + \hat{T}_e + \hat{V}_{ee} + \hat{V}_{en} + \hat{V}_{nn} \qquad (2.3)$$

Explicity, these terms can be written as

$$\hat{H} = \frac{-\hbar^2}{2m_n} \sum_I^{N_n} \nabla^2_{\vec{R}_I} - \frac{\hbar^2}{2m_e} \sum_i^{N_e} \nabla^2_{\vec{R}_I} + \frac{1}{2} \frac{e^2}{4\pi\epsilon_0} \sum_i^{N_e} \sum_{j\neq i}^{N_e} \frac{1}{|\vec{r_i} - \vec{r_j}|}$$

$$+ \frac{1}{2} \frac{e^2}{4\pi\epsilon_0} \sum_I^{N_n} \sum_{J\neq I}^{N_n} \frac{Z_I Z_J}{|\vec{R}_I - \vec{R}_J|} - \frac{e^2}{4\pi\epsilon_0} \sum_{i=1}^{N_e} \sum_{I=1}^{N_n} \frac{Z_I}{|\vec{r_i} - \vec{R}_I|} \qquad (2.4)$$

where $\vec{r_i}$, $\vec{R}_I$ represent position of ith electron and I^{th} nucleus and Z_I is the atomic number of Ith nucleus, N_n and N_e are the number of nucleus and electron respectively.

In this equation given in 2.4, SI units are employed. Therefore, each term includes certain cumbersome combinations of fundamental constants $\hbar$, *m*, *e* and ϵ_0. Also, since we are now dealing with a atomic system, SI units can be inconvenient. Hence, working with *atomic units (a.u)* simplifies the expression. In a.u, $\hbar = m = \frac{1}{4\pi\epsilon_0} = 1$ and the fundamental energy in terms of Hartree which is the ground state energy of the electron in the hydrogen atom. The length is measured in terms of the Bohr radius (a_0) which is the average ground state radius.

Since the mass of electron is much smaller than that of nuclei, the nuclei can be treated as classical particles. This is called the Born-Oppenheimer approximation [25]. By taking advantage of this approximation, the wavefunction can be separated into a nuclear part and an electronic part. Thus, electronic part of Hamiltonian just consist of kinetic energy of electron, electron-electron and electron-nuclei interaction terms. Then, electronic Hamiltonian $\hat{H}_e$ expressed as:

$$\hat{H}_e = \hat{T}_e + \hat{V}_{ee} + \hat{V}_{en} \qquad (2.5)$$

Expressed in a.u., the Hamiltonian in Eq. 2.5 reduces to

$$H = -\frac{1}{2} \sum_i^{N_e} \nabla^2_i + \frac{1}{2} \sum_i^{N_e} \sum_{j\neq i}^{N_e} \frac{1}{|\vec{r_i} - \vec{r_j}|} - \sum_{i,I} \frac{Z_I}{|\vec{r_i} - \vec{R}_I|} \qquad (2.6)$$

13

2.2.2 Definition of Density

Since the direct solution of the Schrödinger equation is a difficult task even for the Helium atom, some alternative solutions needed to be developed for its numerical solution for many-body systems. One possible solution, that gave rise to the development of DFT, proposed by Hohenberg and Kohn in 1964 [26] states the electronic energy can be written as a functional of electronic density. Functional can roughly be defined as a real-valued function meaning that it maps a function to a number. The electronic density operator is defined as a measure of contributions from each electron described by

$$\hat{n}(\vec{r}) = \sum_i^N \delta(\vec{r} - \vec{r_i}) \tag{2.7}$$

Expectation value of this operator can be found as

$$< n(\vec{r}) >= \int \Psi^*(\vec{r_1}, ..., \vec{r_N}) \sum_i \delta(\vec{r} - \vec{r_i}) \Psi(\vec{r_1}, ..., \vec{r_N}) d\vec{r_1}...d\vec{r_N}$$

$$= \int |\Psi(\vec{r}, \vec{r_2}..., \vec{r_N})|^2 d\vec{r_2} d\vec{r_3}...d\vec{r_N} + \int |\Psi(\vec{r_1}, \vec{r}..., \vec{r_N})|^2 d\vec{r_1} d\vec{r_3}...d\vec{r_N}$$

$$= N \int \Psi(\vec{r_1}, ..., \vec{r_N})|^2 d\vec{r_1}...d\vec{r_N} \tag{2.8}$$

As a result of the assumption of a normalized wavefunction, the integral of $n(\vec{r})$ over the entire space must yield the number of electrons.

$$\int n(\vec{r}) d\vec{r} = N \tag{2.9}$$

2.2.3 Energy in terms of Density

The main goal of DFT is to eliminate wavefunction by expressing all terms in the electronic Hamiltonian in terms of density. With the aim to minimize the total electronic energy with respect to the density, the ground state energy and the corresponding electronic density can be obtained. This is made possible by the Hohenberg-Kohn theorem and the basics of this theorem will be discussed in the following subsection.

14

The electronic energy can be written as

$$E_e = \langle \hat{H}_e \rangle = \int \Psi^* \hat{H}_e \Psi \qquad (2.10)$$

We shall now tackle each term in Eq. 2.6. separately and attempt to convert each corresponding energy term into a functional of density. We shall start with the nucleus-electron energy. This term is the simplest one to handle since it does not containt any derivatives and two-particle interaction.

$$E_{ext} = \int \Psi^*(\vec{r}_1, \vec{r}_2, ..., \vec{r}_N) \sum_i v_{ext}(\vec{r}_i) \Psi(\vec{r}_1, \vec{r}_2, ..., \vec{r}_N) d\vec{r}_1...d\vec{r}_N$$

$$= \int v_{ext}(\vec{r}_i) |\Psi(\vec{r}_1, \vec{r}_2, ..., \vec{r}_N)|^2 d\vec{r}_1 + ... \qquad (2.11)$$

By manipulating this integral, keeping in mind that the variables of integration are interchangeable, we obtain the exact equation

$$E_{ext}[n] = \int n(\vec{r}) v_{ext}(\vec{r}) d\vec{r} \qquad (2.12)$$

The electron-electron interaction can similarly be written as

$$E_{ee} = \int \Psi^*(\vec{r}_1, \vec{r}_2, ..., \vec{r}_N) \hat{V}_{ee} \Psi(\vec{r}_1, \vec{r}_2, ..., \vec{r}_N) d\vec{r}_1 d\vec{r}_2...d\vec{r}_N \qquad (2.13)$$

We know the form of $\hat{V}_{ee}$ from Eq. 2.6, substituting this term into Eq. 2.13, we have

$$E_{ee} = \frac{1}{2} \sum_{i \neq j} \int \Psi^*(\vec{r}_1, \vec{r}_2, ..., \vec{r}_N) \frac{1}{|\vec{r}_i - \vec{r}_j|} \Psi(\vec{r}_1, \vec{r}_2, ..., \vec{r}_N) \qquad (2.14)$$

Writing terms explicity in the sum and rearranging terms the integral becomes:

$$E_{ee} = \int \frac{1}{|\vec{r}_1 - \vec{r}_2|} d\vec{r}_1 d\vec{r}_2 \left(\frac{1}{2} \int |\Psi(\vec{r}_1, \vec{r}_2, ..., \vec{r}_N)|^2 d\vec{r}_3 d\vec{r}_4...d\vec{r}_N \right)$$

$$+ \int \frac{1}{|\vec{r}_1 - \vec{r}_3|} d\vec{r}_1 d\vec{r}_3 \left(\frac{1}{2} \int |\Psi(\vec{r}_1, \vec{r}_2, ..., \vec{r}_N)|^2 d\vec{r}_2 d\vec{r}_4...d\vec{r}_N \right) + ... \qquad (2.15)$$

There are $N(N-1)$ terms in this sum and it can easily be demonstrated that they are all equal. With this E_{ee} reduces to

$$E_{ee} = \frac{N(N-1)}{2} \int \frac{1}{|\vec{r} - \vec{r'}|} d\vec{r} d\vec{r'} \left(\int \Psi(\vec{r}, \vec{r'}, ..., \vec{r}_N)|^2 d\vec{r}_3 d\vec{r}_4..d\vec{r}_N \right) \qquad (2.16)$$

The resulting expression in Eq. 2.16 can not be further simplified into a form in terms of the single-particle electronic density. Instead, the two particle density can be used to reduce it to Eq. 2.17.

$$n^{(2)}(\vec{r}, \vec{r'}) = \frac{n(\vec{r})n(\vec{r'})}{2}$$

In an actual system, however, correlations exist even though they are ordinarily small in the solid state. At the moment, we handle the presence of such correlations by means of separating the two-particle density into a fully uncorrelated part and an undetermined correction term:

$$n^{(2)}(\vec{r}, \vec{r'}) = \frac{n(\vec{r})n(\vec{r'})}{2} + \triangle n^{(2)}(r, r')$$

With this final form of the two-particle density, E_{ee} becomes:

$$E_{ee}[n] = \frac{1}{2} \int \frac{n(\vec{r})n(\vec{r'})}{|\vec{r} - \vec{r'}|} d\vec{r} d\vec{r'} + \int \frac{\triangle n^{(2)}(r, r')}{|\vec{r} - \vec{r'}|} d\vec{r} d\vec{r'} \qquad (2.17)$$

In this equation, the first term is called the Hartree energy which is nothing other than the classical potential energy of a continuous charge distributions and the second term contains all the quantum mechanical correlations. Lastly, expectation value of the final term that is the kinetic energy of the electronic Hamiltonian can be written as

$$T = -\frac{1}{2} \int \Psi^*(\vec{r}_1, \vec{r}_2, ..., \vec{r}_N) \bigtriangledown_i^2 \Psi(\vec{r}_1, \vec{r}_2, ..., \vec{r}_N) d\vec{r}_1 ... d\vec{r}_N \qquad (2.18)$$

This term is the one that hardest to deal with since it contains a derivative operator. In order to make a connection with the electronic density, a methodology that relies on single-particle operators must be made. Such an approach was proposed by Kohn-Sham [27] that states that for every N-particle system, one can find an auxilary system of non-interacting electrons such that the true ground state electron density is equal to the sum norm squares of single-particle orbitals corresponding to the independent electrons, called *Kohn-Sham* orbitals

$$n(\vec{r}) = \sum_{i=1}^{N} |\Phi_i(\vec{r})|^2 \qquad (2.19)$$

By placing Eq. 2.19 into Eq. 2.18, we obtain the kinetic energy of non-interacting particles. Obviously, this is not equal to the kinetic energy of the real, interacting

system. Therefore, we once again express kinetic energy as single-particle energy plus a correction term.

$$T = -\frac{1}{2} \int \Phi_n^*(\vec{r}) \, \triangledown^2 \, \Phi_n(\vec{r}) d\vec{r} + \Delta T \tag{2.20}$$

In the end, putting all terms together, we obtain the ground state energy as:

$$E = -\frac{1}{2} \sum_n^{N_e} \int \Phi_n^*(\vec{r}) \, \triangledown^2 \, \Phi_n(\vec{r}) d\vec{r} + \int n(\vec{r}) v_{ext}(\vec{r}) d\vec{r}$$

$$+\frac{1}{2} \int \frac{n(\vec{r})n(\vec{r'})}{|\vec{r} - \vec{r'}|} d\vec{r} d\vec{r'} + \Delta T + \Delta E_{ee} \tag{2.21}$$

The last two correction terms is defined as *the exchange-correlation energy* and plays a very crucial role in DFT by determining the accuracy of calculation.

2.2.4 Hohenberg-Kohn Theorems & Kohn-Sham Equations

The two fundamental theorems that set the foundations of DFT were proposed and proved by Hohenberg and Kohn in 1964 [26]. Their first theorem states that there is a one-to-one correspondence between ground state electronic density and the external potential. In other words, no two unequal potentials can cause the same ground state density.

The second theorem, which derives from the variational principle, states that a universal functional of energy can be defined in terms of the density. The exact ground state is the global minimum of this functional.

$$\frac{\delta E}{\delta n} = 0 \tag{2.22}$$

To apply the second theory, in practice, functional derivative of Eq. 2.22 should be taken with respect to the orbitals of the auxiliary system of non-interacting particles in order to minimize ground state energy. Functional derivative gives :

$$\frac{\delta E}{\delta \Phi_i^*(\vec{r})} = \frac{\delta E}{\delta n(\vec{r})} \frac{\delta n(\vec{r})}{\Phi_i^*(\vec{r})} = \frac{\delta T_e}{\Phi_i^*(\vec{r})} + \left[\frac{\delta E_{ext}}{\delta n(\vec{r})} + \frac{\delta E_{Hartree}}{\delta n(\vec{r})} + \frac{\delta E_{xc}}{\delta n(\vec{r})} \right] \frac{\delta n(\vec{r})}{\Phi_i^*(\vec{r})} \tag{2.23}$$

Applying the orthonormality condition of the Kohn-Sham orbitals by defining Lagrange multipliers, obtain a Schrödinger-like system referred to as the Kohn-Sham equations

$$[\hat{T}_e + \hat{V}_{ext} + \hat{V}_H + \hat{V}_{xc}]\Phi_i = \epsilon_i \Phi_i \qquad (2.24)$$

Here, the terms in square brackets form Kohn-Sham Hamiltonian and the eigenvalues ϵ_i terms are Kohn-Sham energies. Since, all the potential terms in the Kohn-Sham equations depend on the density, the equation needs to be solved self-consistently.

2.2.5   van der Waals corrections

As it is mentioned in the section 2.2.3, expressing the ground state energy in terms of the electronic density is the central idea of the DFT method. In Eq. 2.21, explicit form of this ground state energy is given and this energy expression is formally exact except the exchange-correlation energy term. For this term, commonly used approximations techniques are the local density approximation (LDA) and the generalized gradient approximation (GGA). While LDA depends solely on the density variable, GGA necessitates not only the density but also its gradient. With these techniques, DFT rapidy became successful in a wide range of applications [28]. However, due to the nature of these approximations, they neglect long-range and non-local interactions which is the origin of the van der Waals (vdW) forces. In physical chemistry, vdW forces are usually an umbrella term given to the collection of three forces between molecules; permanent dipole-dipole, permanent dipole-induced dipole and two instantaneously induced dipoles (generally known as London dispersion force) [28]. The vdW forces are implemented in DFT as a correction to the expression of the exchange correlation energy in terms of the electronic density, $E_{xc}[n]$. The correction can be introduced essentially in one of two ways. The classical, nondispersive portions of the vdW interaction is already taken into account by conventional DFT. Dispersion corrections on the other hand, require dynamic correlation, which are absent and must be handled separately. The more straightforward method of correcting for the long-range dispersion contribution developed in several works such as Scoles [29, 30] and Grimme [31] involves an empirical correction with the form C_6/r_{ij}^6 with a short-range truncation to avoid singularities. In these approaches, usually termed DFT-D, C_6 is an atom-

dependent coefficient to the well-known $1/r^6$ term in the instantaneous dipole-dipole interactions. While straightforward to implement and calculate, the atom-specific coefficient presents a problem in the DFT-D approaches. To introduce more generality, self-consistent exchange-correlation that include non-local, long-range van der Waals corrections have been introduced. Among the many renditions of such schemes, we emply in particular the exchange-correlation functional names vdW-DF-C09, where C09 refers to the Cooper correction [32], which corrects the overbinding due to the DFT-DF correction.

Our DFT calculations were performed in Quantum Espresso software distributed free under the GNU Public Licence [33].

2.3 Molecular Dynamics (MD)

Molecular Dynamics (MD) is a many-body simulation technique based on Newtonian mechanics. The key concept in MD simulations is the interatomic potentials. These potential describe how a collection of atoms interact with each other. For reasons of efficiency, the interatomic potentials in question only depend upon nuclear coordinates, with the effects of the electrons taken into account through an adequate number of parameters. Instead of solving quantum electronic problem, one can introduce another strategy by expressing the electron-nuclei interaction by using an empirical potential whose parameters are obtained by results of quantum mechanical computations or experiments [35].

The force on the ith atom can be determined from the derivative of these potentials as:

$$\vec{F}_i = -\nabla U_i(\vec{r}_1, \vec{r}_2, ..., \vec{r}_N) \tag{2.25}$$

where F_i and r_i the force on the $i^t h$ atom and the coordinate of the $i^t h$ atom, respectively.

In MD, trajectories of interacting atoms are found by the numerical solutions of the

Newtonian equations of motion. Newton's 2nd law can be written as:

$$\vec{F}_i = m_i \frac{\mathrm{d}^2 \vec{r}_i}{\mathrm{d}t^2} \tag{2.26}$$

In order to initiate the numerical integration of Eq. 2.26, initial positions and velocities are needed. By updating positions and velocities in time, thermodynamic averages can be calculated. The most commonly used integration techniques are the so-called Verlet [41] and Velocity Verlet algorithms. The details of these algorithms will be discussed in the following subsection. Our MD simulations performed using LAMMPS (Large-scale Atomic/Molecular Massively Parallel Simulator) an open source code under GNU Public License called distributed freely by Sandia National Laboratories [49].

2.3.1 Main Algorithms of MD

Most integration schemes them use Taylor expansion to numerically update positions and velocities of the atoms. Euler, Verlet-Velocity Verlet, Leapfrog and Predictor-Corrector algorithms are widely used Taylor-based integration schemes in MD simulations. An algorithm should be fast, memory and storage requirements, time-reversible and reveal small divergence from the exact particle trajectories. These are main desired features of an algorithm. Among the algorithms mentioned above, Verlet and velocity Verlet algorithms are default integration schemes used in the LAMMPS code and will be discussed briefly in the following two subsections.

2.3.1.1 Verlet Algorithm

This algorithm was first developed by Loup Verlet in 1967 [41]. By expanding the position of the ith particle around an arbitrary moment in time using a small time increment Δt, we obtain

$$\vec{r}_i(t + \Delta t) = \vec{r}_i(t) + \dot{\vec{r}}_i(t)\Delta t + \frac{1}{2}\ddot{\vec{r}}_i(t)\Delta t^2 + \frac{1}{3!}\dddot{\vec{r}}_i(t)\Delta t^3 + .. \tag{2.27}$$

$$\vec{r}_i(t - \Delta t) = \vec{r}_i(t) - \dot{\vec{r}}_i(t)\Delta t + \frac{1}{2}\ddot{\vec{r}}_i(t)\Delta t^2 - \frac{1}{3!}\dddot{\vec{r}}_i(t)\Delta t^3 + .. \tag{2.28}$$

Adding Eq. 2.27 and 2.28 eliminates all odd-powered Δt terms reducing the equations to :

$$\vec{r_i}(t + \Delta t) = 2\vec{r_i}(t) - \vec{r_i}(t - \Delta t) + \ddot{\vec{r_i}}\Delta t^2 = 2\vec{r_i}(t) - \vec{r_i}(t - \Delta t) + \frac{F_i(t)}{m_i}\Delta t^2 \quad (2.29)$$

In this algorithm, the error is in the order of Δt^4. Hence, a smaller time step indicates higher accuracy. This is a very basic, precise and stable algorithm and most of the MD codes use it as a default algorithm. However, it does not calculate velocities of atoms. Velocities, which are necessary for fundamental functions such as temperature control, require an extra calculation, increasing the computational cost.

2.3.1.2 Velocity Verlet Algorithm

The Verlet algorithm can be adapted to yield the velocities all at once, resulting in the velocity Verlet algorithm. The velocity Verlet algorithm is also based on the Taylor expansion of the position given in Eq. 2.27 and 2.28. This time by subtracting these two equations yields

$$\vec{r}(t + \Delta t) - \vec{r}(t - \Delta t) = 2\ddot{\vec{r}}(t)\Delta t + O(\Delta t^3) \quad (2.30)$$

Here, velocity at time t basically found as:

$$\vec{v}(t) = \frac{\vec{r}(t + \Delta t) - \vec{r}(t - \Delta t)}{2\Delta t} + O(\Delta t^2) \quad (2.31)$$

Accuracy in this scheme is up to order Δt^2. Important property of these two algorithms is that they are time-invariant such that if time is reversed from Δt to $-\Delta t$, algorithms remain same.

2.3.2 Thermodynamic Ensembles

2.3.2.1 Microcanonical Ensemble

Since the total energy is conserved in the Newton's equations of motion, standard MD simulations should in principle obey the microcanonical ensemble. In this ensemble, in addition to total energy of system E, number of particles N and volume V

21

remains constant during the simulation. In the equations of motion, the kinetic energy by itself is not conserved. Therefore, temperature of the system in this ensemble fluctuates with time. Besides, because of the numerical errors during the integration, total energy can fluctuate. Generally, NVE ensembles are not usually preferred since they are not represent experimental conditions. Experiments mostly correspond to isothermal-isobaric (*NPT*), canonical (*NVT*) or grand-canonical (μVT) ensembles [42].

2.3.2.2   Canonical Ensemble

In the canonical ensemble case, in addition to the number of particles *N* and volume *V* temperature *T* is also constant. Constant temperature, in thermodynamical point of view, means putting system in contact with a large heat bath. Practically this is achieved by introducing a thermostat to the system to keep temperature constant in some manner [47]. Details of some well-known thermostats used in MD simulations will be discussed in the following subsections. Temperature in MD simulations is calculated from the kinetic energy by using the following relation:

$$T(t) = \frac{1}{k_B N_f} \sum_i m_i v_i^2(t) \tag{2.32}$$

Here, N_f is the number of degrees of freedom and k_B is the Boltzmann constant.

2.3.2.3   Isothermal-Isobaric Ensemble

In the isothermal-isobaric ensemble, as its name suggests, temperature *T*, pressure *P* and number of particles *N* are constant. In this case, volume is considered as a dynamical variable and changes during the simulation [42]. This ensemble can be a suitable choice when the correct pressure and densities are point of interests in the simulation.

2.3.3   Controlling Temperature in MD Simulations: Thermostat Concept

When performing MD simulations in the NVT or NPT ensemble, a thermostat must be introduced to regulate the temperature of the system at desired values. There are

some well-known thermostats within the context of MD simulations. In this subsection, basic principles of these commonly used thermostat algorithms will be discussed briefly.

2.3.3.1 The Nosé-Hoover Thermostat

The Nosé-Hoover thermostat is an algorithm based on the extended Lagrangian, that is a Lagrangian contains additional, artificial coordinates and velocities, first formulated by Nosé [45] and improved by Hoover [46]. Nosé proposed a real system of N particles with coordinates q_i', momenta p_i', time t' and a fictitious system with coordinates q_i, momenta p_i and time t. The relations between these two systems are given as:

$$q_i' = q_i, \quad p_i' = p_i/s, \quad t' = \int_0^t \frac{dt}{s} \tag{2.33}$$

where s is an additional degree of freedom. By using these relations given in Eq. 2.33, velocity of the real system can be written as:

$$\frac{dq_i'}{dt'} = s\frac{dq_i'}{dt} = s\frac{dq_i}{dt} \tag{2.34}$$

In terms of variables of the fictitious system, the Lagrangian of extended system is given as [45] :

$$L_{Nose} = \sum_i^N \frac{m_i}{2}s^2\dot{q_i}^2 - \phi(q) + \frac{Q}{2}\dot{s}^2 - gkTlnS \tag{2.35}$$

where Q is the effective mass associated with s and g is the number of degrees of freedom of the system. Then this Lagrangian is used to calculate the Hamiltonian and and the equations of motions of the extended system. The Nosé-Hoover is the default thermostat used in LAMMPS and can be applied to a desired group of atoms by defining the initial temperature *Tstart*, final temperature *Tstop* and damping parameter *Tdamp* that defines the frequency with which the thermostat will be activated during the simulation. Corresponding LAMMPS input for this thermostat is given below.

```
##Usage of Nosé-Hoover thermostat in LAMMPS
fix ID group-ID style_name Tstart Tstop Tdamp ...
fix 1 all nvt temp 300.0 300.0 100.0
```

2.3.3.2 Velocity-rescaling

In this technique, velocity scaling is done at every time-step according to following relation:

$$p_i \rightarrow \sqrt{\frac{T_0}{T}} p_i \qquad (2.36)$$

Here, T_0 is the target temperature and T is the temperature calculated from velocities of atoms during simulation. Fluctuations in the temperature are not allowed during the simulation. However, this technique has a disadvantage that is discontinuity in the momentum because of velocity rescaling at each time-step [47].

2.3.3.3 The Berendsen Thermostat

Berendsen [48] introduced a new formulation to the velocity rescaling approach in order to overcome the disadvantage of the traditional velocity rescaling technique. This thermostat aims to correct deviations of actual temperature T from the initial one T_0 multiplying the velocities at each time step by a factor λ and it is given as :

$$\lambda = \sqrt{1 - \frac{\delta t}{\tau} \left(1 - \frac{T_0}{T(t)} \right)} \qquad (2.37)$$

where δt is the time-step, τ is the time constant of coupling parameter, T_0 and $T(t)$ represent thermostat temperature and instantaneous temperature respectively. In the Berendsen algorithm, the system is weakly coupled to an external heat bath to allow temperature fluctuations [47]. Rate of change of temperature is given as

$$\frac{dT}{dt} = \frac{T_0 - T}{\tau} \qquad (2.38)$$

where τ is the coupling parameter that regulates the interaction strength between the heat bath and the system. The Berendsen thermostat is implemented in the LAMMPS code and again can be activated by using similar parameters to those of the Nosé-Hoover thermostat. Corresponding LAMMPS input for this thermostat is given below.

```
##Usage of Berendsen thermostat in LAMMPS
fix ID group-ID temp/berendsen Tstart Tstop Tdamp
fix 1 all temp/berendsen 300.0 300.0 100.0
```

2.3.3.4   The Langevin Thermostat

Langevin dynamics is a stochastic approach developed to model dynamics of molecular systems. The basic idea of Langevin dynamics in a realistic scenario, molecules are in environments with solvent molecules that lead to friction and collisions of these molecules also create a perturbation for this system. Two additional force terms can be appended to the Newton's 2nd law to represent these effects.

$$\vec{F} = \vec{F}_c + \vec{F}_f + \vec{F}_r \tag{2.39}$$

In this equation, $\vec{F}_c$ is the conservative force which is computed from the interatomic potential, $\vec{F}_f$ is the frictional drag term and $\vec{F}_r$ is the force caused by solvent molecules at temperature T that collides with the atoms randomly. In the thermostat implementation of Langevin dynamics, molecules interact randomly with this stochastic heat bath. The usage of the Langevin termostat within the LAMMPS input is given below.

```
##Usage of Langevin thermostat in LAMMPS
fix ID group-ID langevin Tstart Tstop Tdamp seed ...
fix 1 all langevin 300.0 300.0 100.0 48279
```

Since the Langevin thermotat is a stochastic approach in contrast to the Nosé-Hoover and Berendsen thermostats, a random number generator is employed.

Each of these three (Nosé-Hoover, Berendsen and Langevin) thermostats have some advantages and disadvantages depending on the applications they are used. We tested these thermostats on a PEEK chain to decide which thermostat should be used in our

simulations. The difference that we see between them in our test simulations, will be given in the following result chapter.

2.3.3.5   The Flying Ice Cube Artifact

One of the well-known numerical integration errors faced in MD simulations is the so-called flying ice-cube artifact [50]. This unexpected phenomenon is a consequence of numerical errors in MD algorithms. Therefore, it is fully unphysical because of the violation of the energy equipartition.

Harvey et al. in 1998 stated that periodic velocity rescaling leads to an unexpected problem: a gradual bleeding of kinetic energy from high frequency modes such as bond stretching and angle bending into low frequency modes [50]. This causes the system to execute rigid rotations and translations with large angular or linear velocities, at the same time suppressing the internal degrees of freedom. This artifact is mostly encountered in the MD simulations performed in vacuum. There are some alternatives to avoid this artifact. Three of them are discussed in the original paper of Harvey et al [50]. The first alternative is the reassignment of velocities instead of rescaling, as done in the stochastic Andersen thermostat [51]. Velocities are reassigned periodically from Maxwell-Boltzman distribution for the desired temperature. The second choice is making modifications on the algorithms that use velocity rescaling technique. For example, one can reduce the frequency of scaling or increase coupling times in the Berendsen heat bath. The third alternative is the removing the center of mass motion. The translational and rotational motion of center of mass can be removed periodically to avoid this artifact. In our calculations, when we encounter with this problem, we choose to remove the center of mass motion. In LAMMPS, the way of doing it is the fix momentum command that adjusts velocities in every N step by zeroing linear and angular momentum of system. Its usage in the input is given below.

```
## Usage of fix momentum command in LAMMPS
  fix ID group-ID momentum N keyword values ...
  fix 1 all momentum 100 linear 1 1 1 angular
```

2.3.4 Controlling Pressure in MD Simulations: The Barostat Concept

In addition to controlling temperature by using thermostats, a barostat is needed to keep pressure constant during the simulation. The *NPT* ensemble is often preferred in MD simulations because most experiments are performed at constant pressure and temperature. Pressure in MD simulations is calculated by using the Clausius virial theorem. The virial is defined as

$$W^{TOT}(\vec{r}_1, ..., \vec{r}_N) = \sum_{i=1}^{N} \vec{r}_i \cdot \vec{F}_i^{TOT} \tag{2.40}$$

By manipulating this equation using the Newton's second law average virial can be written as:

$$\langle W^{TOT} \rangle = \lim_{\tau \to \infty} \frac{1}{\tau} \int_0^{\tau} \sum_{i=1}^{N} \vec{r}_i(t) \cdot m_i \ddot{\vec{r}}_i(t) dt \tag{2.41}$$

Integration by parts to Eq. 2.41 yields the average virial equal to the twice of the total kinetic energy with a minus sign,therefore, by using the equipartition theorem

$$\langle W^{TOT} \rangle = \langle W^{int} \rangle + \langle W^{ext} \rangle = -2 \langle K.E \rangle = -3Nk_BT \tag{2.42}$$

where W^{int} and W^{ext} is the internal and external virials respectively.

For an enclosed volume with side lengths L_x, L_y and L_z, pressure can be defined as external force per applied area. Therefore, external virial of the system can be written as:

$$\langle W^{ext} \rangle = \sum_{i=1}^{N} \vec{r}_i \cdot \vec{F}_i^{ext} = L_x(-PL_yL_z) + L_y(-PL_xL_z)L_z(-PL_xL_y)$$

$$= -P(3L_xL_yL_z) = -3PV \tag{2.43}$$

Then, by substituting 2.43 into 2.42, pressure for an enclosed volume can be calculated as:

$$P = \frac{Nk_BT}{V} + \frac{1}{3V} \sum_{i=1}^{N} \vec{r}_i \cdot \vec{F}_i^{int} \tag{2.44}$$

Two types of barostating methods are available in the LAMMPS code: Nosé-Hoover barostat and Berendsen barostat. The barostat adjusts volume to keep temperature

constant as in the Berendsen thermostat, this time volume is multiplied by factor λ given as

$$\lambda = \left[1 - \frac{\beta \Delta t}{\tau}\left(P_0 - P\right)\right]^{1/3} \qquad (2.45)$$

where β is the isothermal compressibility, τ is the coupling time, P_0 and P are desired pressure and instantaneous pressure respectively. Corresponding LAMMPS input for this barostat is given below.

```
## Usage of Berendsen barostat in LAMMPS
fix ID group-ID press/berendsen keyword Pstart Pstop Pdamp
fix 1 all press/berendsen iso 1.0 1.0 1000.0
```

When using the Berendsen barostat initial pressure *Pstart*, target pressure *Pstop* and the time scale on which pressure is relaxed *Pdamp* values should be specified.

2.3.5 Interatomic Potentials

Interatomic potentials describe the nature of the interaction between the atoms. There are a variety of interatomic potential functions developed for different purposes [44]. The relevant parameters of these potential functions are obtained either through experiments or through higher accuracy, quantum mechanical methods such as DFT.

In the Eq. 2.46, many-body expansion of an empirical potential is given for the system of N-atoms.

$$U(\vec{r}_1, \vec{r}_2, ..., \vec{r}_N) = \sum_i U_1(\vec{r}_i) + \sum_i \sum_{j>i} U_2(\vec{r}_i, \vec{r}_j)$$

$$+ \sum_i \sum_{j>i} \sum_{k>j} U_2(\vec{r}_i, \vec{r}_j, \vec{r}_k) + ... \qquad (2.46)$$

The first term in the expansion is a one-body term, representing an external field, the second term U_2 represents the pair potential and the third one is the three-body potential term. As we see from this expansion, there are pairwise and many-body

potentials within the MD technique. Some commonly used interatomic potentials can be listed for different types of systems:

Pairwise Potentials

- Lennard-Jones

- Morse

- Buckingham

Many-body potentials for metallic systems

- Embedded Atom Model (EAM)

- Finnis and Sinclair (FS)

Many-body potentials for covalently bonded systems

- Tersoff

- Stillinger-Weber

- Adaptive Reactive Intermolecular Bond Order Potential (AIREBO)

- Force Fields (Molecular Mechanics Potentials)

One of the widely used pairwise potential Lennard-Jones [53] will be discussed briefly in the following subsection. Continuing on this issue, many-body potentials that we use in our calculations Tersoff, AIREBO and Reactive Force Field (ReaxFF) also will be described briefly.

2.3.5.1 Lennard-Jones Potential

Lennard-Jones [52, 53] is one of the simplest potentials that describes basic interaction between neutral atoms and molecules. This potential successfully approximates

van der Waals interactions in specifically in noble gases. The form of this pair potential is given as

$$U_{LJ} = 4\varepsilon \left[\left(\frac{\sigma}{r} \right)^{12} - \left(\frac{\sigma}{r} \right)^{6} \right] \qquad (2.47)$$
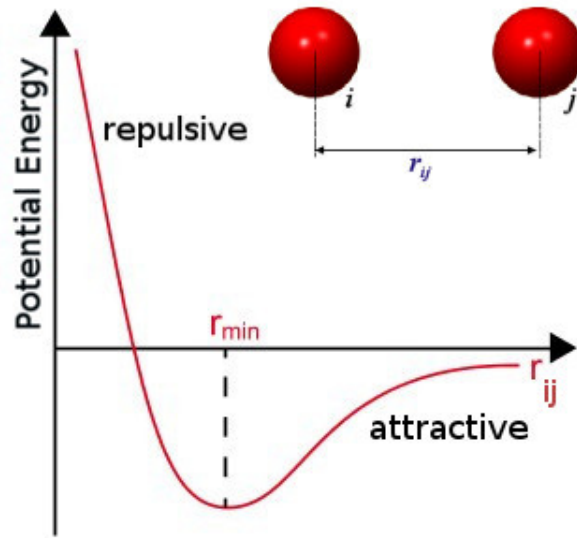
Figure 2.1: Potential Energy graph of Lennard-Jones pair potential

In the Eq. 2.47, first term represents the short range Pauli repulsion term and the second term represents long range attractive van der Waals interaction. The parameters σ and ϵ are related to bond length and bond energy respectively and taken from experimental data for each element.

In Fig.2.1 that shows potential energy graph of the Lennard-Jones, r_{min} is the equilibrium distance between two atoms. Since in the CNT carbon atoms are covalently bonded to each other, LJ is not a good choice to describe interaction of this material. To prescribe the interaction of a CNT, three different interatomic potentials; Tersoff [55], AIREBO [56] and different versions of ReaxFF [58, 61] are tested in our simulations.

30

2.3.5.2 Potentials for Carbon-based Systems

Tersoff Interatomic Potential

Tersoff is a three-body, bond order, empirical potential developed for covalent systems [54, 55]. The main idea of this potential is that in real life, environmental conditions determine the strength of bonding, therefore, in the potential energy term, environmental dependent parameters are used. The parameters are first developed for silicon [54] and then for carbon [55]. It is also parametrized for germanium, that is to say, this potential can be used in group IV semiconductors. In simple form, it is given as:

$$E = \frac{1}{2} \sum_i \sum_{i \neq j} U_{ij} \tag{2.48}$$

In the Eq. 2.48, U_{ij} can be written as:

$$U_{ij} = f_C(r_{ij})[f_R(r_{ij}) + b_{ij} f_A(r_{ij})] \tag{2.49}$$

where $f_R(r_{ij})$ and $f_A(r_{ij})$ are repulsive and attractive pair potentials respectively and $f_C(r_{ij})$ is the cut-off function that is added to limit the potential range and reduce the computational cost. The three-body contributions originate from the b_{ij} term in the Eq.2.49. The b_{ij} term is the term that provides the environmental dependence of this potential, as we expect, increase in the neighbor numbers lowers the strength of bond. It can also be seen from the following definition of b_{ij} :

$$b_{ij} = \frac{1}{(1 + \beta^n \zeta_{ij}^n)^{1/2n}} \tag{2.50}$$

where ζ_{ij} defines the neighbor numbers by considering the distance between them and the bond angle term. Explicit form of this parameter is given as:

$$\zeta_{ij} = \sum_{k \neq i,j} = f_c(r_{ij}) g(\theta_{ijk}) e^{[\lambda_3^3(r_{ij} - r_{ik})^3]} \tag{2.51}$$

In the Eq.2.51, $g(\theta_{ijk})$ is the term that defines the bond angle formed between three atoms. All the parameters for specific elements can be found in the papers. Corresponding LAMMPS input for the Tersoff potential is given below.

```
## Usage of Tersoff potential in LAMMPS
pair_style style
pair_coeff * * Si.tersoff Si ## path, name, element
```

Adaptive Reactive Intermolecular Bond Order Potential (AIREBO)

Bond order AIREBO potential is developed specifically for a system of hydrogen and carbon atoms by Stuart et al. [56]. It consists of three energy terms given in the following form:

$$E_{AIREBO} = \frac{1}{2} \sum_i \sum_{i \neq j} \left(E_{ij}^{REBO} + E_{ij}^{LJ} + \sum_{k \neq i,j} \sum_{l \neq i,j,k} E_{kijl}^{TORSION} \right) \qquad (2.52)$$

In Eq. 2.52, the first energy term is the second generation *REBO* potential developed by Brenner et al. [57], the second term is the simple *LJ* interaction and the last term is four-body torsional interaction energy. The E^{REBO} energy provides reactive part of the AIREBO potential and only defines two-body, short range interaction between C-C, C-H and H-H. The usage of AIREBO potential in LAMMPS input is given below.

```
## Usage of AIREBO potential in LAMMPS
pair_style airebo 3.0
pair_coeff * * CH.airebo C ## path, name, element
```

2.3.5.3 Reactive Force Field (ReaxFF)

Since the traditional potentials do not have the ability of modeling bond breaking and bond formation features, they cannot successively model chemical reactions. Because of this reason, the first version of the ReaxFF [58] was developed for hydrocarbons, later corrected for the London dispersion [62] and improved for condensed phases of carbon [61]. QM based methods offer more realistic results at the electronic level, however, they have high computational cost when considering the full evolution of

systems [63]. Empirical interatomic potentials require less computational cost but they need pre-defined connectivity between atoms [63]. ReaxFF method acts as a connection between these two QM based and classical techniques. In addition to being a bond-order potential, it also describes bond formation and bond breaking without any QM calculation.

Since it is a reactive potential, different from Tersoff and AIREBO, ReaxFF uses a charge calculation scheme in MD simulations. This makes the ReaxFF more expensive than other empirical potentials, although, not as much as QM based ones.

The total potential energy form in ReaxFF is given as :

$$U_{Total} = U_{bond} + U_{over} + U_{angle} + U_{torsion} + U_{vdW} + U_{Coulomb} \qquad (2.53)$$

In the Eq. 2.53, the first term U_{bond} is related to the interatomic distance and defines the energy associated with bond formation between atoms. U_{angle} and U_{tors} terms represent the energies of three-body valence angle strain and four-body torsional angle strain respectively. U_{over} term is called over-coordination energy that represents energy penalty that is based on atomic valence rules. $U_{Coulomb}$ and U_{vdW} terms come from electrostatic and van der Waals interactions. In our calculations, we used three different versions of the ReaxFF, namely ReaxFF$_{CHO}$ [58], ReaxFF$_{C2013}$ [61] and ReaxFF$_{LG}$ [62]. Corresponding LAMMPS input for ReaxFF potential is given below.

```
 ## Usage of the ReaxFF-CHO in LAMMPS
pair_style reax/c lmp_control
pair_coeff * * ffield.reax.cho C H O
 ## Additional charge calculation scheme
fix ID group qeq/reax N cutlo cuthi tolerance params
fix 1 all qeq/reax 100 0.0 10.0 1.0e-6 param.qeq
```

In the charge equilibration scheme (qeq), *Nevery* represents the frequency with which the qeq calculation will be performed, *cutlo, cuthi* are the low and high cutoff for Taper radius, *tolerance* represents the precision to which charges will be equilibrated

and *params* is the file name that contains parameters are taken from the potential file and this file should include one line for each atom type.

2.3.6 Time step in MD

In MD simulations, the equations of motion are integrated by using discrete time steps. One should be careful about choosing the suitable time step when performing simulations. While large time steps reduce the computational expense, they give less accurate results. On the other hand, choosing very small time steps to increase accuracy also increases the computational cost. In LAMMPS, all interatomic potentials work in different unit systems. For example, while Tersoff and AIREBO potentials work in *metal units*, the ReaxFF works in *real units*. Details of metal and real units are given in the list below.

- For metal units:

    - mass = grams/mole

    - distance = Angstrom

    - temperature = Kelvin

    - energy = eV

    - pressure = bars

    - time = picoseconds

- For real units:

    - mass = grams/mole

    - distance = Angstroms

    - temperature = Kelvin

    - energy = Kcal/mole

    - pressure = atmospheres

    - time = femtoseconds

CHAPTER 3

MECHANICAL PROPERTIES OF CARBON NANOTUBES

As mentioned in Chapter 1, CNTs have been used as reinforcements in composite materials in recent applications. In accordance with this purpose, in this chapter, mechanical properties of different CNTs will be examined using DFT and MD techniques. In this chapter, computational details of these simulations and their results will be discussed.

3.1   Mechanical Properties of Carbon Nanotubes by using DFT

3.1.1   Optimized Length Calculation

Our preliminary DFT studies start with the optimized length calculation for the (10,0) zigzag CNT with 40 atoms periodic in the axial z-direction with length 4.26 Å displayed in Figure 3.1. Three different methods namely DFT-D, vdW-DF and vdW-DF-C09 were used to calculate optimized length of this CNT with a PBE(Perdew-Burke-Ernzerhof) pseudopotential. The energy cutoff was set to 40 Rydberg and 1x1x10 k-point mesh was used. In Figure 3.2, the graphs of cell parameter of CNT along
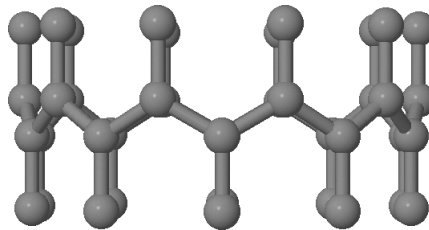
Figure 3.1: Unit cell of (10,0) zigzag CNT

z-direction are given with three different functionals. While DFT-D overestimates length of the CNT, vdW-DF with the exchange of Cooper (vdW-DF-C09) gives the most accurate result for the length of CNT. Therefore, we used this functional in our further DFT studies.

(a) DFT-D

(b) vdW-DF

(c) vdW-DF-C09
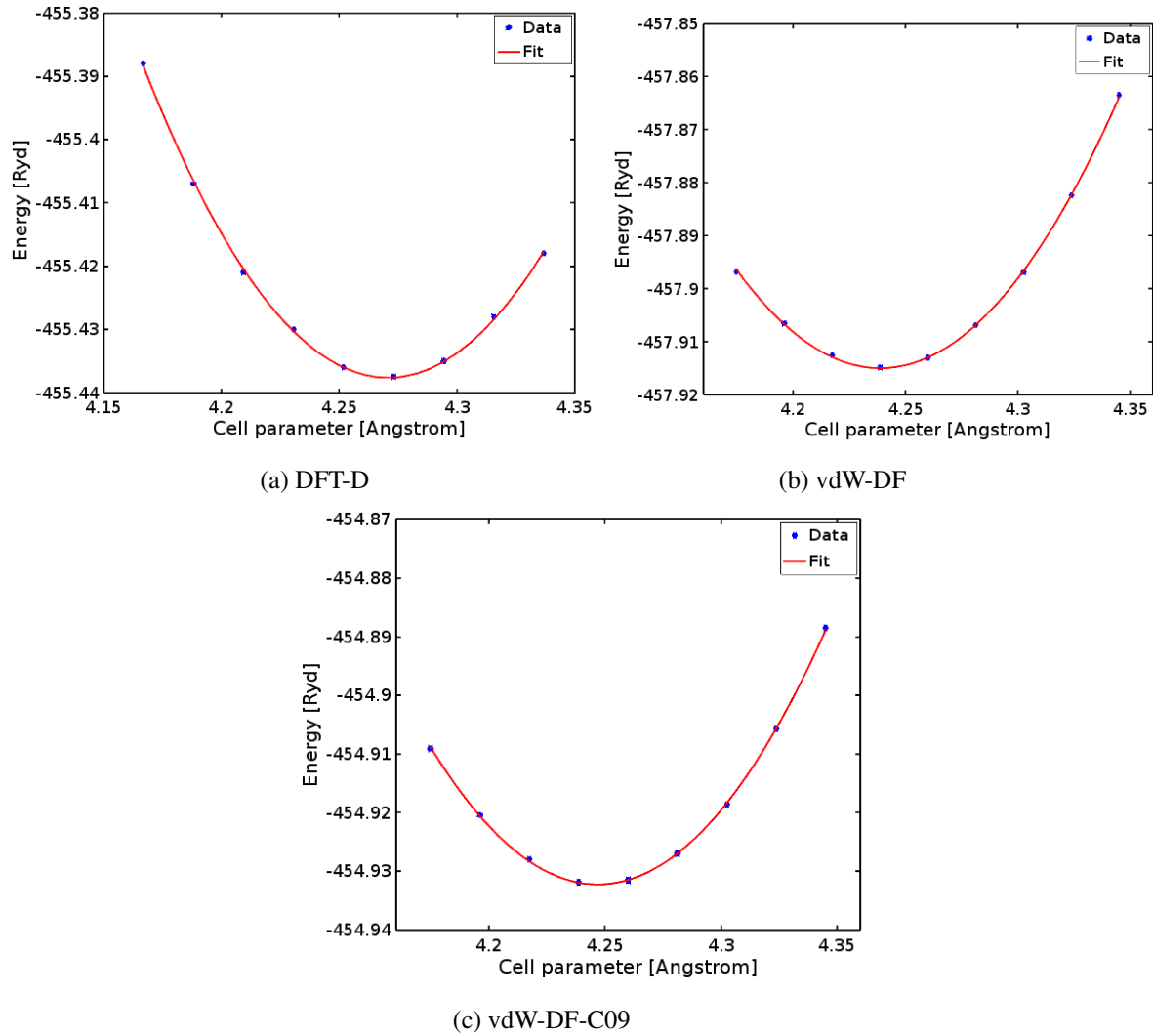
Figure 3.2: Optimized length of (10,0) CNT with different functionals

3.1.2 Young's Modulus and Poisson's Ratio Calculation

Young's modulus (or modulus of elasticity) is related with the response of a material under tension or compression deformations. This property implies the stiffness of material and it can be defined as follows:

$$E = \frac{1}{V_0} \frac{\partial^2 U}{\partial \varepsilon^2} \tag{3.1}$$

where U is the strain energy, ε is the applied strain and V_0 is the equilibrium volume which is defined for a CNT as :

$$V_0 = 2\pi R_0 L_0 h \tag{3.2}$$

where R_0 and L_0 are equilibrium radius and length that corresponds to minimum energy and h is the wall thickness of a CNT which is taken as 0.34 nm [64].

When a material is compressed/stretched in axial direction, it usually tends to expand/contract in the transverse directions. This phenomenon is called the Poisson effect and is measured by the so-called Poisson's ratio. For a CNT Poisson's ratio can be expressed by using the following relation:

$$\nu = -\frac{1}{\varepsilon} \frac{R - R_0}{R_0} \tag{3.3}$$

where ε is the strain along the axial direction, R_0 is the unperturbed radius, and R is the new radius under stress.

Young's modulus calculation for (10,0) CNT is done with the following protocol; first CNT is subjected to a series of compressive and extensive strains in the axial z-direction. For each strain value, the CNT is allowed to evolve under interatomic forces until a new equilibrium is reached. Following this, the graph of strain versus energies corresponding to each strain is plotted as shown in the Figure 3.3 (a) and fitted to a 2nd order polynomial within the -2% and +2% strain limits and Young's modulus is calculated by using the formula given in Eq. 3.1. Also, by using Eq. 3.3 given above Poisson's ratio is calculated within the same strain limits.

By means of a simple measurement of the Young's modulus and Poisson's ratio results for the (10,0) zigzag CNT are shown in Table 3.1. Here, we again compared the three functionals, that are used the optimized length calculation part, for calculating Young's modulus and Poisson's ratio of (10,0) CNT. There are numerous studies that investigate the mechanical properties of CNTs with different methods. In most of the studies, the Young's modulus results vary from 0.5 TPa to 1.5 TPa depending on the methods used. Hernández et al. [65] studied C and $B_xC_yN_z$ composite tubes by using DFT and similar results are obtained with the vdW-DF-C09.

Table 3.1: Young's modulus and Poisson's ratio of a (10,0) one-unit cell CNT with different functionals

Functional	E [TPa]	ν
DFT	0.99	0.173
vdW-DF	1.115	0.175
vdW-DF-C09	1.11	0.176
Hernández et al. [65]	1.22	0.27

(a)   (b)
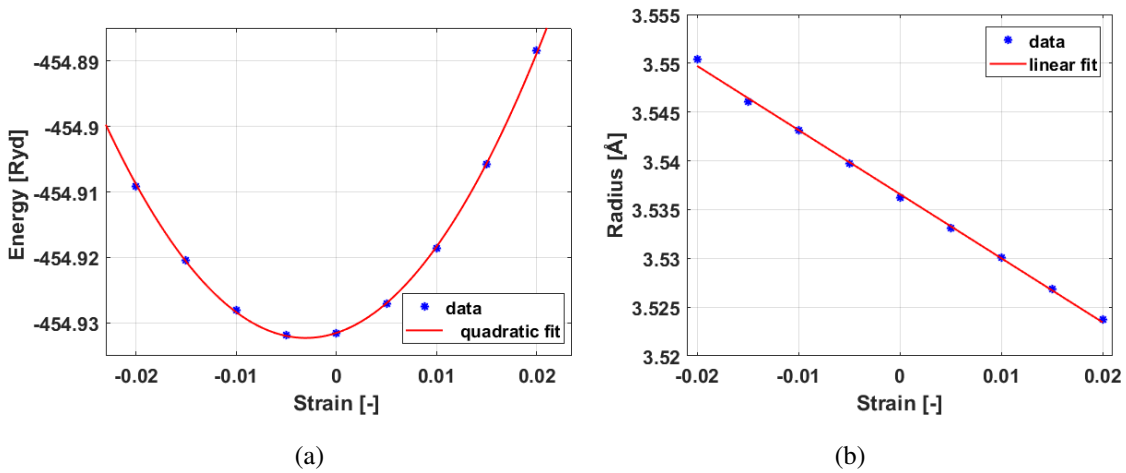
Figure 3.3: The graphs of (a) axial strain versus total energy and (b) axis versus radius change for (10,0) CNT used in Young's modulus calculation

3.2 Mechanical Properties of CNTs by using MD

When characterizating the mechanical properties of CNTs by using molecular dynamics simulation technique, some important parameters must be chosen carefully in order to represent real behaviour of CNTs [43]. The reliability of MD simulations mainly depends on the choice of inter-atomic potential, thermostat, thermostat coupling coefficient and time step. These parameters were already discussed in Chapter 2 in detail. In the literature, instead of a well-defined protocol, there are variety of scattered results regarding the choices of these parameters. When studying CNTs in MD simulations generally Tersoff, AIREBO and ReaxFF interatomic potentials are preferred since these are developed for carbon based systems. We perform MD simulations at 0 K and 300 K to examine mechanical properties of CNT under axial loading. In both static loading (T=0K) and dynamic loading (T=300K), the same procedure is followed with the exception that in finite temperature case, we consider a time average of the property in question. As in the DFT calculations, Young's modulus and Poisson's ratio are calculated in the regions between $-0.02 < \varepsilon < +0.02$ strains.

3.2.1 Elastic Constants Under Static Loading

Our initial mechanical calculations were done using the Tersoff potential which is a 3-body potential function that is widely used for carbon, silicon and germanium elements as discussed before. First, Young's modulus and Poisson's ratio of a (5,0) one unit cell CNT, shown in Figure 3.4, was investigated with the same protocol as was used in DFT calculations. By using the definition in Equation 3.1, Young's modulus of CNTs with different chiralities were calculated and the results are given in Table 3.2. Our findings are in good agreement with previous DFT results and literature. However, Poisson's ratio results for these CNTs are found to be negative. In fact, this is a well-known shortcoming of this potential noted also by Kiselev et al. [66] who studied mechanical properties of graphene with the Tersoff potential reported a negative value for Poisson's ratio. Therefore, we move on our investigations with AIREBO, ReaxFF$_{CHO}$ (developed by Chenoweth et al. [59]) and ReaxFF$_{C2013}$ a revised version of ReaxFF for carbon systems.
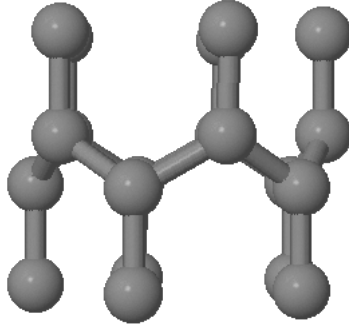
Figure 3.4: Unit cell of (5,0) CNT

(a)

(b)
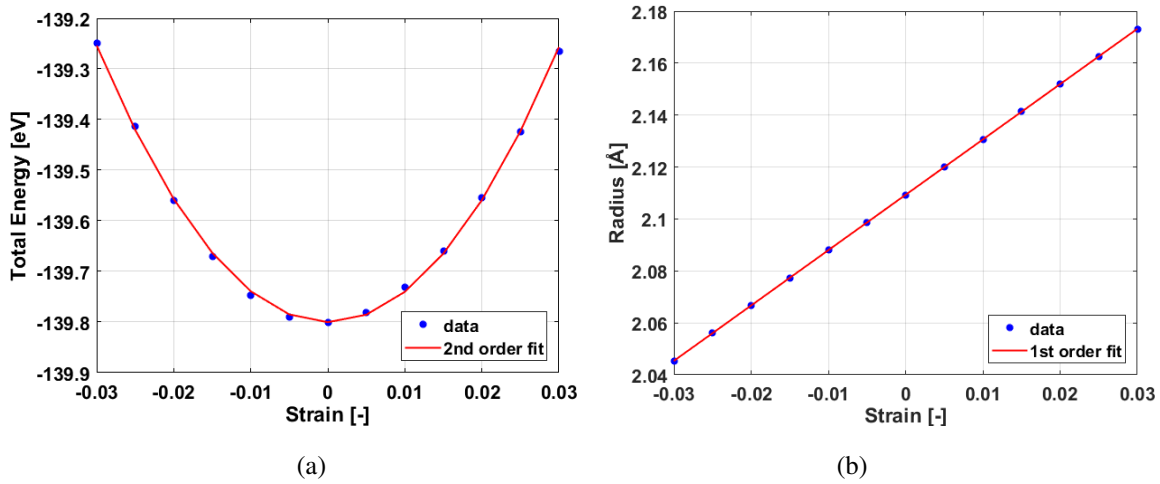
Figure 3.5: (a) Strain versus energy and (b) strain versus radius graphs of (5,0) one unit cell CNT modeled with Tersoff potential

Table 3.2: Young's modulus of different CNTs by using Tersoff Potential

CNT	Type	E [TPa]
(5,0)	Zigzag	0.99
(5,5)	Armchair	1.17
(10,10)	Armchair	1.18
(4,3)	Chiral	1.12
(6,9)	Chiral	1.17

In literature, several examples of successful simulations of graphene and CNTs done using AIREBO can be seen [60, 67]. Nath and Kim [67] studied the nanomechanics of CNTs by using three different potentials namely Tersoff, REBO and AIREBO and

they concluded that AIREBO is much more reliable and accurate than other potentials when calculating elastic properties of CNTs since it includes van der Waals and torsional terms [67]. When we compare Young's modulus and Poisson's ratio results given in Table 3.3 for CNTs with different chiralities displayed in Figure 3.6, we immediately see that while AIREBO results show good agreement with both theoretical and experimental Young's modulus and Poisson's ratio values reported in the literature, the ReaxFF$_{CHO}$ version slightly overestimates the Young's modulus of CNTs and gives Poisson's ratio higher than experimental and theoretical values as stated by Jensen et al. [68]. On the other hand, ReaxFF$_{C2013}$ version, developed for investigating elastic properties and mechanical failure in carbon based materials, gives more accurate results than the ReaxFF$_{CHO}$ parametrization [68].
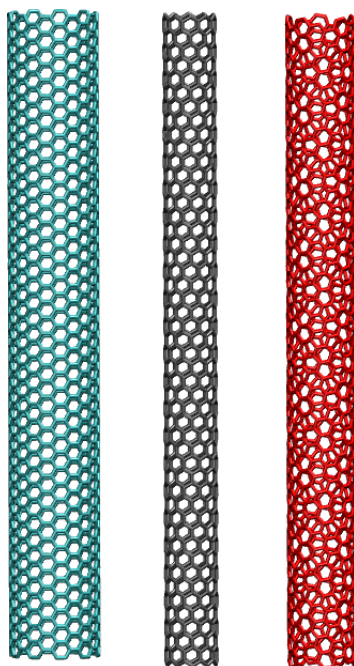
Figure 3.6: 10 nm length CNTs with 3 different chirality used in the calculations. Cyan represents the (10,10) armchair CNT, gray is the (10,0) zigzag and red one is the (5,10) chiral. All of them are generated via Visual Molecular Dynamics (VMD) tool.

| | (a) | | (b) |
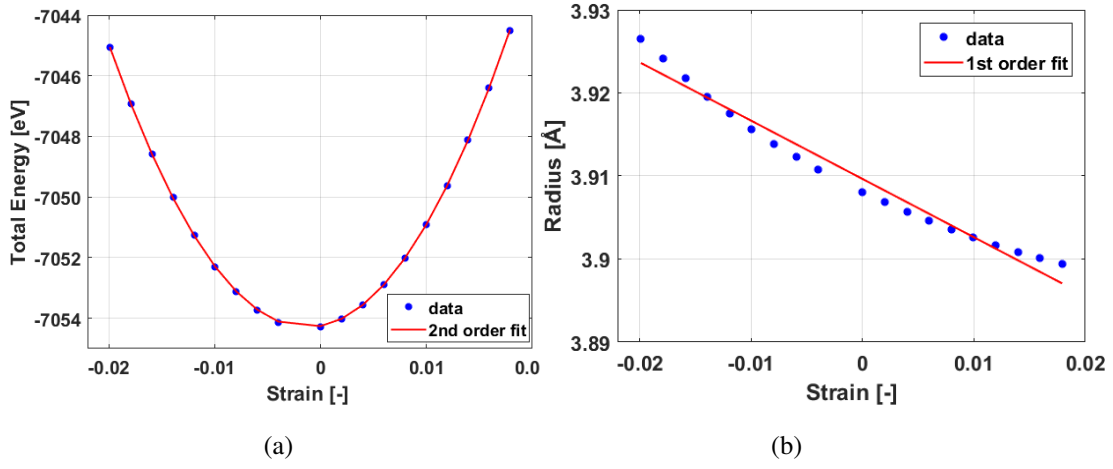
Figure 3.7: (a) Strain versus energy and (b) strain versus radius plots of (10,0) 10 nm zigzag CNT with AIREBO potential

Table 3.3: Young's modulus and Poisson's ratio of three different CNTs by using AIREBO and two different ReaxFF potentials at T=0K

	AIREBO		**ReaxFF**$_{CHO}$		**ReaxFF**$_{C2013}$	
	E [TPa]	ν	E [TPa]	ν	E [TPa]	ν
(10,0)	1.01	0.19	1.15	0.93	0.76	0.53
(5,10)	0.94	0.24	1.23	0.97	0.78	0.54
(10,10)	0.91	0.26	1.27	0.98	0.77	0.52

Buckling Behavior of CNTs

Buckling of a CNT appears as a non-linear response of CNTs to large deformations. A structure is said to be "buckled" when it collapses suddenly under applied load to release excess strain energy. The buckling behavior of a CNT depends on the aspect ratio [21, 70] given as follows:

$$a = \frac{L}{D} \tag{3.4}$$

where L is the length and D is th diameter of CNT.

Two different modes of buckling behavior have been identified in the literature: shell buckling and Euler buckling [70]. While shell buckling behavior is observed in CNTs with small aspect ratios, CNTs with large aspect ratios exhibit Euler buckling characteristics. The buckling patterns of these two modes are given in Figure 3.8.
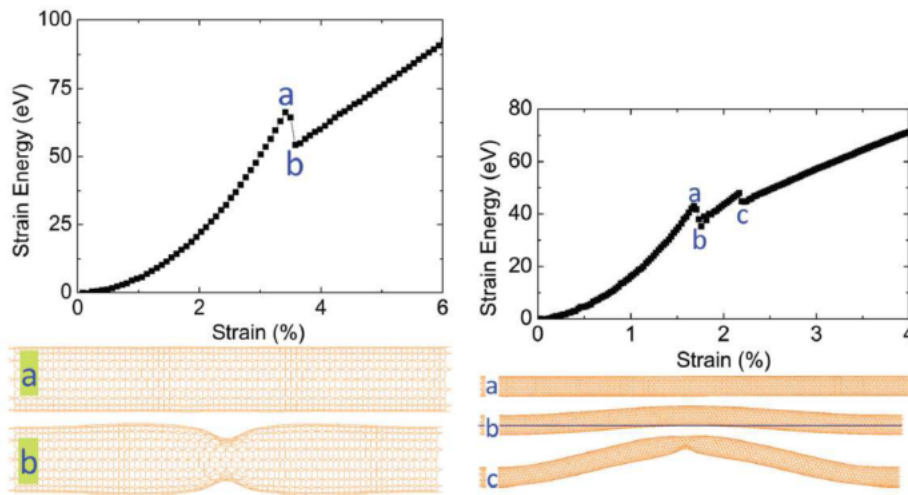
Figure 3.8: Geometry of shell buckling (left) and Euler (right) buckling cases for (10,10) CNT with length of 9.6 nm and 29.5 nm respectively. Redrawn from Ref. [71]

(a)   (b)
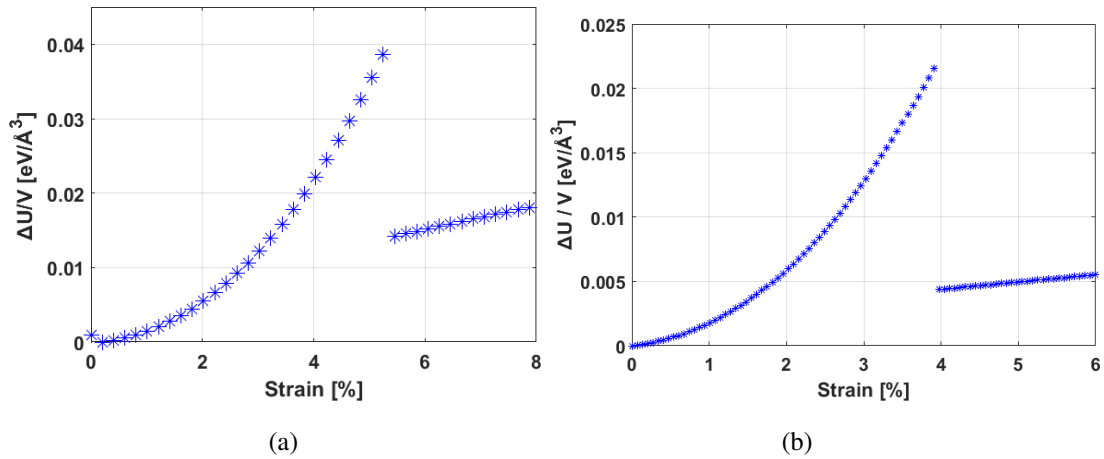
Figure 3.9: Strain versus Energy/Volume graphs of (10,10) CNT under compression with aspect ratio (a) ~7 and (b) ~22 at T=0K
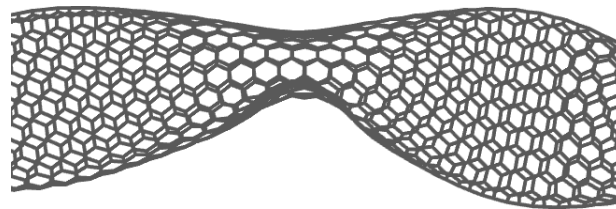
(a) Shell buckling of (10,10) CNT with L=10 nm

(b) Euler buckling of (10,10) CNT with L=30 nm

Figure 3.10: Buckled geometries of (10,10) CNT with two different aspect ratios

In the Figure 3.9, strain versus energy per volume graphs of (10,10) armchair CNTs with two different aspect ratios are given. These two CNTs are chosen for a direct comparison with the study of Feliciano and co-workers [71] who examined (10,10) SWCNTs of lengths 9.6 nm (aspect ratio ~7) and 29.5 nm (aspect ratio ~22) by using MD simulations where the bonding and non-binding interactions were modeled using REBO and LJ potentials [52, 53] respectively. Their simulations were performed at 5 K with the Berendsen thermostat algorithm [48]. For the CNT with small aspect ratio, they observe a shell buckling at the 3.5 % critical strain with a sudden drop in the energy of the system. As seen from Figure 3.9, for the CNT with small aspect

ratio (~7) we observe an abrupt change in the energy at 5 % strain at 0 K temperature. On the other hand, while they observe Euler type of buckling for CNT with larger aspect ratio (~22) at 1.6 % critical strain rate, this behavior is observed around 4 % critical strain in our case (see Figure 3.9 (b)). To compare, in our simulations conducted at 0 K temperature, CNTs with both small and large aspect ratios can sustain compression deformation at higher strain rates than the ones in the study of Feliciano and co-workers [71]. This difference can be explained by different temperatures and interatomic potentials used.

Figure 3.11 shows the behavior of (10,0) CNT with an aspect ratio ~13 under large axial deformations. It can be concluded that, after $-0.02 < \varepsilon < +0.02$ strain limits CNT starts to show non-linear behavior and CNT endures more stretching deformations than compression.
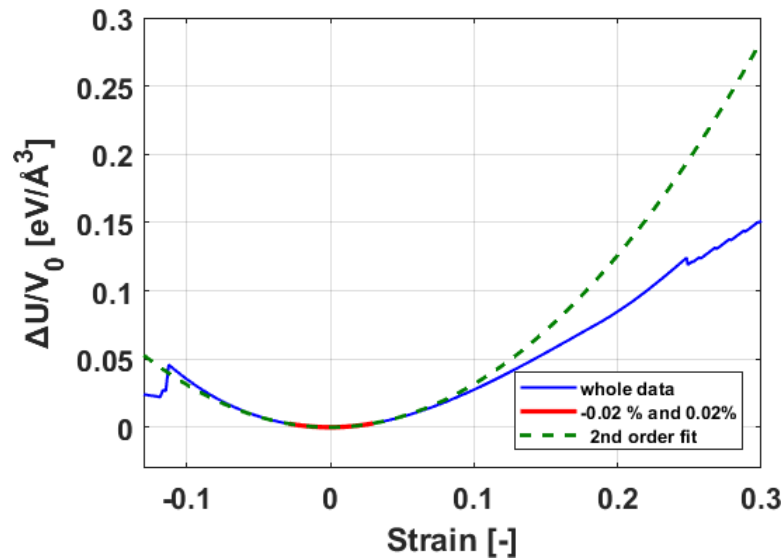
Figure 3.11: The graph of strain versus energy per volume of (10,0) zigzag 10 nm length CNT with AIREBO potential under large deformations at T=0K. Red line shows elastic region that we take into account and the blue line shows the behavior of CNT under larger deformations.

Shear (Torsional) Modulus

In literature, experimental studies on the mechanical properties of SWCNTs are limited, particularly for shear modulus, due to complexity of their characterization at the

nano scale [73]. For this reason, their mechanical properties under torsional loading is generally studied by using computational techniques. There are mainly three different modeling approaches namely atomistic scale simulations including MD, the continuum mechanics and continuum nanomechanics [73, 74]. In our calculations, torsional deformation is applied on four different zigzag CNTs with equilibrium length 6.52 nm and chilarities (5,0), (8,0), (10,0) and (12,0) at 0 K temperature. The energy associated with torsion was calculated by means of twisting either end of the nanotubes in opposite directions and allowing the twisted nanotube to reach equilibrium. Once twisted, the rings at the ends of the CNT are fixed during the equilibration states, as shown in Figure 3.12. The associated energies corresponding to torsion angles were plotted and fitted to 2nd order polynomial as shown in the Figure 3.13. The torsional modulus of these four CNTs are calculated according to the following formula:

$$G = \frac{L}{J}\frac{\mathrm{d}^2 U}{\mathrm{d}\theta^2} \tag{3.5}$$

where L is the length, θ is the rotation angle, U is the energy corresponding to rotation angle and J is the polar moment of inertia which can be defined for a CNT as follows:

$$J = 2\pi h R_0 \left(R_0^2 + \frac{h^2}{4} \right) \tag{3.6}$$

where h is the thickness and R_0 equilibrium radius of a CNT which is assumed as cylindrical shell.

Torsional rigidity (*GJ*), which is explained as material's resistance to twisting deformation, can be found as a multiplication of shear modulus and polar moment of inertia. in Eq.3.5 as

$$GJ = L\frac{\mathrm{d}^2 U}{\mathrm{d}\theta^2} \tag{3.7}$$

According to the results, torsional modulus slightly increases with the increasing radius as shown in Figure 3.14 (a) as stated by Pereira et al. [73] , Wang et al. [75] and Xiong et al. [77]. Torsional rigidity (*GJ*) also increases with increasing radius [73] as in Figure 3.14 (b). This means that larger CNTs show more resistance to twisting deformations.
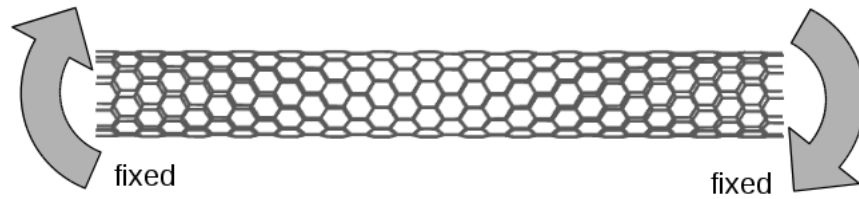
Figure 3.12: Applied torsion type
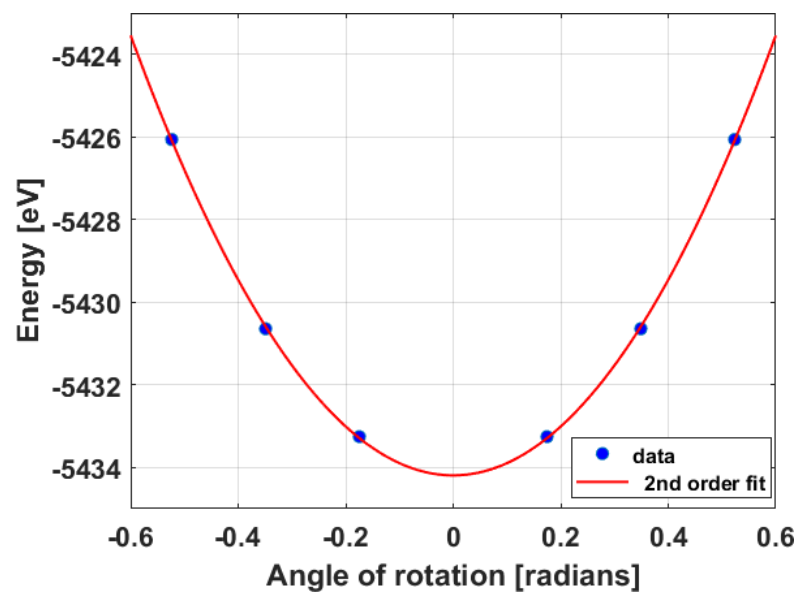
Figure 3.13: The graph of angle of rotation versus energy

Table 3.4: Shear modulus and torsional rigidity of four different CNTs with increasing radius by using AIREBO Potential at 0 K temperature

CNT	Radius [nm]	G [TPa]	GJ [TPaÅ^3]
(5,0)	0.199	0.212	61.47
(8,0)	0.319	0.212	190.29
(10,0)	0.399	0.225	358.24
(12,0)	0.479	0.233	618.32

(a)   (b)
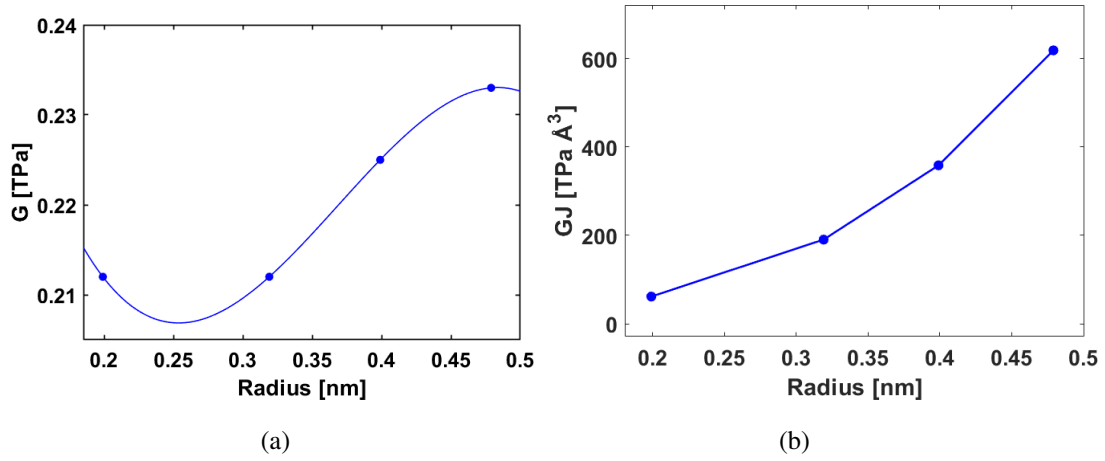
Figure 3.14: (a) The graph of CNT radius versus shear modulus and (b) CNT radius versus torsional rigidity

3.2.2 Elastic Constants Under Dynamic Loading

To calculate the Young's modulus and the Poisson's ratio at 300 K, first, ideally formed CNTs are statically optimized using the conjugate gradient algorithm to find their minimum energy configuration. They are then thermalized at 300K in the NVT ensemble using Nosé-Hoover thermostat. Then, they are subjected to compressive and tensile deformations for 500 ps within the -2 % and 2 % strain ranges with 0.001 ps/Å rate. Since ReaxFF$_{CHO}$ overestimates Poisson's ratio of CNTs at 0 K temperature, AIREBO and ReaxFF$_{C2013}$ versions are used to calculate mechanical properties of CNTs. At the beginning 10 nm-long CNTs were considered, however, buckling behavior was observed at low strain levels at T=300K. Therefore, 5 nm-long (10,0) and (10,10) CNTs were used in the calculations.

Similar work was done by Bialoskórski and Rybicki [78] with the AIREBO potential and Nosé-Hoover thermostat. They studied 400 CNTs of lengths around 170 Å and radii ranging from 4.2 Å to 34.6 Å. In their work, they calculated Young's modulus and Poisson's ratio in the negative (-2 % $< \varepsilon < 0$) and positive ($0 < \varepsilon < 4$ %) strain regions separately and averaged. Their results are given in the Table 3.5 and compared with our results that calculated the ranges of -2 % $< \varepsilon < 0$ compression and $0 < \varepsilon < 2\%$ stretching regions as in Figure 3.15.

Table 3.5: Young's modulus and Poisson's ratio of CNTs calculated by using AIREBO at T=300K

CNT	E_+ [TPa]	E_- [TPa]	E [TPa]	ν_+	ν_-	ν
(10,0)	0.93	0.97	0.95	0.11	0.19	0.15
Ref. [78]	0.83	0.91	0.87	0.09	0.20	0.15
(10,10)	0.87	1.17	1.02	0.22	0.15	0.19
Ref. [78]	0.73	0.93	0.83	0.23	0.17	0.21

As compared with the AIREBO, while the ReaxFF$_{C2013}$ slightly underestimates the Young's modulus, Poisson's ratio values were found to be higher as in Table 3.6.
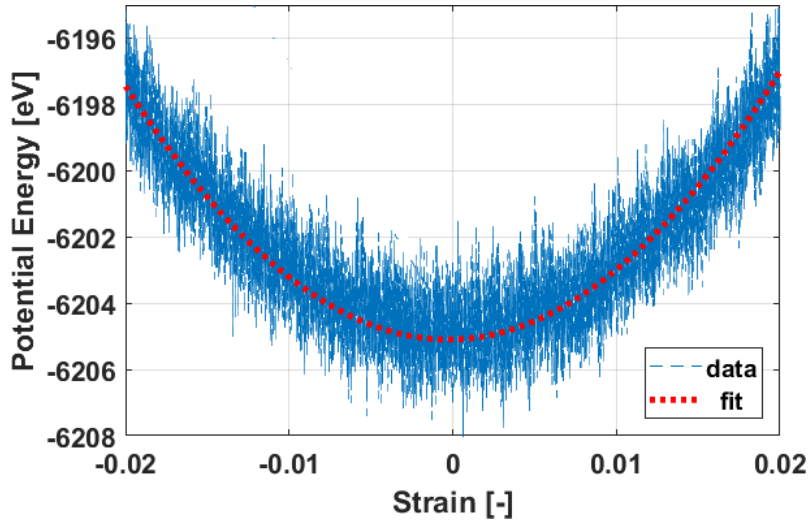
Figure 3.15: Strain versus Potential energy plot of (10,0) CNT with L=5nm by using ReaxFF$_{C2013}$

Table 3.6: Young's modulus and Poisson's ratio of CNTs with two different chiralities by using ReaxFF$_{C2013}$ at T=300K

CNT	E_+ [TPa]	E_- [TPa]	E [TPa]	ν_+	ν_-	ν
(10,0)	0.839	0.829	0.834	0.610	0.599	0.605
(10,10)	0.768	0.739	0.754	0.574	0.539	0.557

CHAPTER 4

MOLECULAR DYNAMICS SIMULATIONS OF PEEK CHAINS

In this chapter, we first examine the conformers of PEEK monomer in vacuum. We conduct a series of simulations with three different thermostats together with ReaxFF$_{CHO}$ and ReaxFF-lg versions of the ReaxFF potential. We will compare our results in addition to the ideal chain model of polymers.

4.1 Single PEEK Monomer in Vacuum

Preliminary MD calculations of PEEK polymer was initiated with the investigation of its conformers in vacuum. In order to systematically search over the conformers of the PEEK monomer, it is divided into 3 parts as shown in the Figure 4.1 and first by keeping ring 2 and 3 fixed, ring 1 is rotated 180° around the x-axis by 1° increments and an energy minimization is conducted following after every rotation. Rotation angle versus energy graph is plotted as in Figure 4.3 and the minimum energy configuration is found at 169° angle .
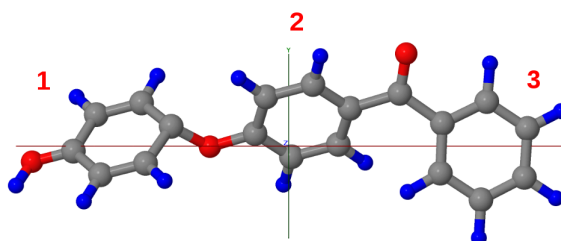
Figure 4.1: Rings of PEEK monomer. Carbons are represented with gray, hydrogens are blue and oxygens are red.

Ring 3 is rotated by keeping ring 1 and 2 fixed to find another possible minimum energy configurations. This time energy minimum is observed at 17° rotated ring 3 configuration. Both minimum configurations of the PEEK monomer are displayed in Figure 4.2.

169° (front view)   169° (top view)

17° (front view)   17° (top view)
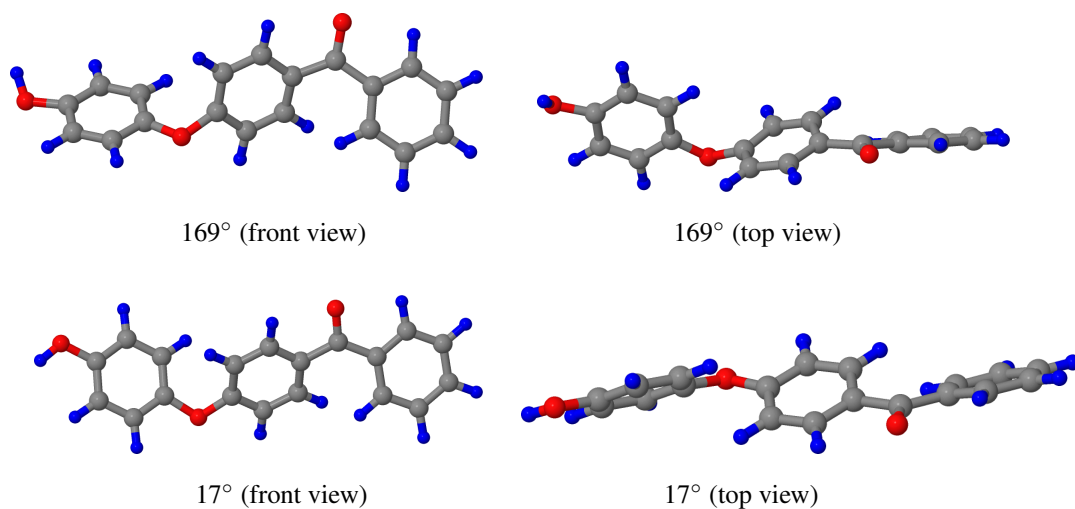
Figure 4.2: Minimum configurations of the PEEK monomer

(a)   (b)
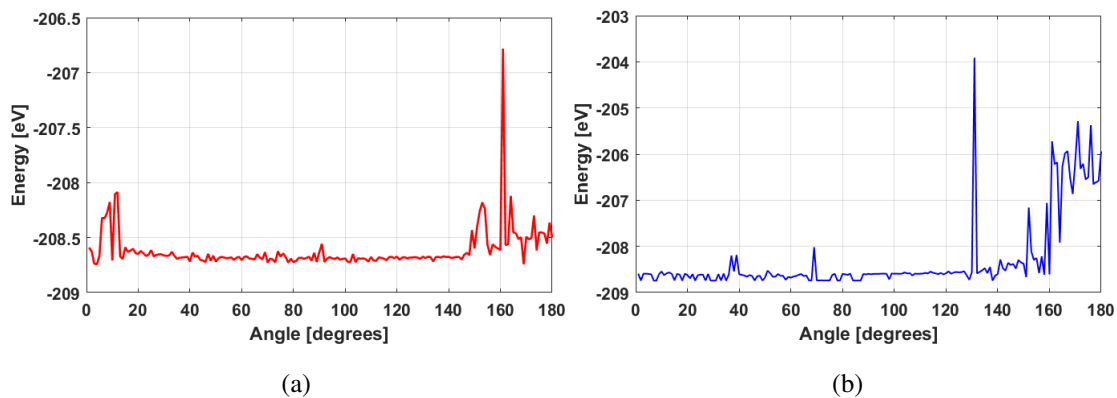
Figure 4.3: Angle vs. Energy plots of PEEK monomer when (a) Ring 1 is rotated (b) Ring 3 is rotated

In Figure 4.3, the highest energy points correspond to the closest distance of the hydrogen atoms found at the joint parts of the sub-units.

4.2 Thermostat and Potential Tests on PEEK Chains

When performing MD simulations, a thorough benchmarking process including the selection and the fine-tuning of the thermostat must be carried out. In literature, a large number of ReaxFF studies are conducted using either the Berendsen or the Nose Hoover thermostat [69, 79]. In contrast, the Langevin thermostat is often not preferred. Jensen et al. [69] tested the Berendsen and Nosé-Hoover thermostats as well as the Langevin to investigate how a stochastic thermostat work with the ReaxFF. These three thermostats with Chenoweth parametrization of the ReaxFF (ReaxFF$_{CHO}$) were tested on mechanical failure of carbon allotropes. They found that thermostat type has no notable influence on mechanical response of carbon allotropes yet damping parameter of thermostat can affect preticted behaviors. To this end, we performed a series of MD simulations with these three thermostat algorithms on PEEK chains with monomer lengths of 3,6 and 9. In addition to ReaxFF$_{CHO}$ version, we also tested ReaxFF-lg version developed by Liu et al [62] which have been reported to give more accurate mechanical properties for the PEEK polymer. Other potentials (AIREBO, Tersoff and ReaxFF$_{C2013}$) used for predicting mechanical properties of CNTs in previous chapter cannot be used when modeling PEEK polymer since they do not contain carbon, hydrogen and oxygen parametrizations at once.

The end-to-end distance and the radius of gyration are two of the basic properties associated with polymer chains. According to The Ideal Chain (or Freely-jointed chain) model, that is the simplest model used for describing the characteristics of polymer chains, the interaction between structural units (i.e. monomers) that create polymer are neglected and they are assumed as a rigid rods with fixed length b that is known as the Kuhn length. Therefore, an unfolded polymer has the length given by following relation:

$$L = Nb \tag{4.1}$$

where N is the number of Kuhn segments.
According to Figure 4.4, $\vec{R}$ can be calculated as a sum of individual components as:

$$\vec{R} = \vec{b}_1 + \vec{b}_2 + .. = \sum_{i=1}^{N} \vec{b}_i \tag{4.2}$$

When a polymer chain is long enough, these randomly oriented vectors cancel each other and mean of end-to-end vector approximates zero.

$$\langle \vec{R} \rangle = \sum_{i=1}^{N} \langle \vec{b_i} \rangle = 0 \tag{4.3}$$

To avoid loss of information the square of end-to-end distance is used [80] and given as:

$$\vec{R^2} = \sum_{i=1}^{N} \vec{b_i} \cdot \sum_{j=1}^{N} \vec{b_j} = nb^2 + 2 \sum \sum_{i<j} \vec{b_i} \cdot \vec{b_j} \tag{4.4}$$

where n is the number of bond vectors.

The second term of the Eq. 4.4, the dot product of the two vectors depend on the bond angle between them, hence :

$$\sum \sum_{i<j} \vec{b_i} \cdot \vec{b_j} = b^2 cos\theta_{ij} \tag{4.5}$$

Since the bond angle between these vector uniformly distributed between 0 to 2π [80], this term does not contribute to Eq. 4.4 and thus it reduces to

$$\langle R^2 \rangle = nb^2 \tag{4.6}$$

The radius of gyration is another quantity that describes the chain size more meaningful than the end-to-end distance since it gives a better understanding of the size of polymer coil and can be measured directly [80, 82]. It also gives an understanding of polymer folding and calculated by using the following formula:

$$\vec{R_g^2} = \frac{1}{M} \sum_i (\vec{r_i} - \vec{r_{cm}})^2 \tag{4.7}$$

where M is the total mass of atoms in the chain and $\vec{r_{cm}}$ is the center of mass position.

According to this formula, a larger radius of gyration is indicative of a more extended polymer whereas a smaller value points towards a folded configuration.
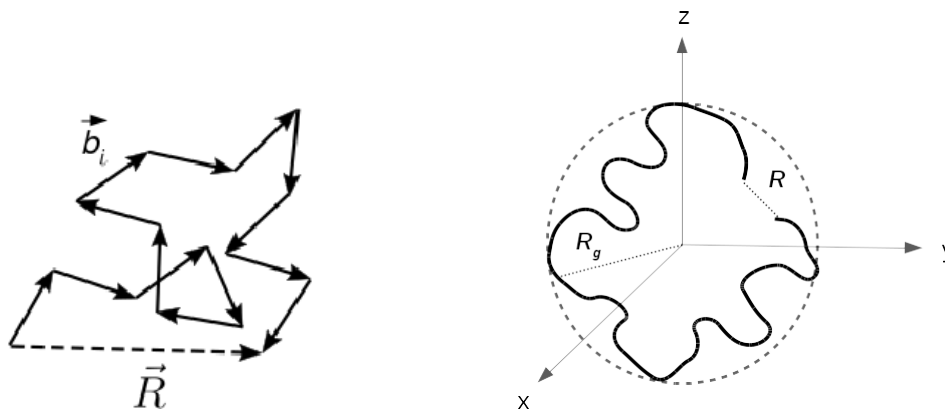
Figure 4.4: End-to-end vector $\vec{R}$ and Kuhn length of an ideal chain (left) and radius of gyration of polymer chain (right)

The general protocol that was used in these MD simulations on the PEEK chains with three different length as follows: The simulation was performed within the NVT ensemble at 10 K temperature with a time step of 0.1 fs for a duration of 1 ns. The thermostat damping parameter was set to 100 (in time units) for all thermostats which means temperature of the system was updated every 10 fs during 1 ns. The end-to-end distance, radius of gyration, potential energy and temperature profiles have been investigated as figures of merit in the comparison of thermostats and potentials.

The step that comes before the actual simulation, namely the creation of the monomer in an acceptable, low energy conformer, is not a trivial task. PEEK chains that consist of 3,6 and 9 monomers were created by using nanoHUB Polymer Modeler tool [81] which in turn uses the configurational bias Monte Carlo (MC) option as shown in the Figure 4.5.

In the following subsection, properties of these PEEK chains that were examined under MD conditions at 10 K temperature, will be compared.

4.2.1 The Nosé-Hoover Thermostat

First, we investigated three different lengths of PEEK chain displayed in Figure 4.5 by using the Nosé-Hoover thermostat with both ReaxFF$_{CHO}$ and ReaxFF-lg potentials. In these calculations in vacuum, we encountered an unexpected numerical integration artifact the so-called *The Flying Ice Cube* that was discussed in detail in Chapter 2.
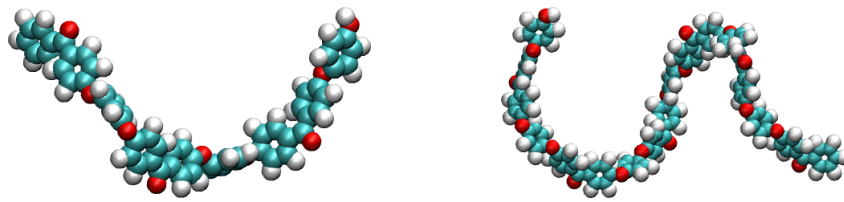
(a) 3 momomer PEEK chain with 104 atoms (b) 6 momomer PEEK chain with 206 atoms
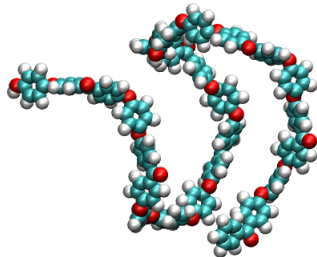
(c) 9 momomer PEEK chain with 308 atoms

Figure 4.5: 3, 6 and 9 monomer PEEK chains created via nanoHUB Polymer Modeler tool [81] by using configurational bias MC chain configurations option. Cyan represents carbon atoms, white represents hydrogen and red ones are oxygen atoms

We faced these problem when we used the Berendsen thermostat as well as the Nosé-Hoover thermostat. This artifact was avoided by using the *fix momentum* command in the LAMMPS software that periodically removes the linear and angular momentum of the system by adjusting the velocities of atoms.

The temperature, energy, end-to-end distance and radius of gyration quantities of the system is recorded in every 500 fs time steps during 1 ns meaning that we collect 2000 data points during the simulations. Final configurations for both ReaxFF$_{CHO}$ and ReaxFF-lg versions are displayed in Figure 4.6 and 4.9 for the initial cases in Figure 4.5. We see that, except the 3-monomer length case, PEEK chains modeled with ReaxFF$_{CHO}$ and ReaxFF-lg potential, polymer chains folded. In Figure 4.8 the potential energy plot of 6-monomer length PEEK is displayed. It can be seen that the polymer chain lowers it potential energy by folding as stated by Lindenmeyer [83]. The energy drops until the 200 ps and then oscillates around equilibrium values over the simulation. Folding of a chain can be understood by end-to-end distance and radius of gyration graphs of chain. For instance, in Figure 4.7 that end-to-end distance and radius of gyration of 3-monomer PEEK chain remains almost constant meaning that chain folding did not occur for this case.

(a) 3-PEEK   (b) 6-PEEK   (c) 9-PEEK
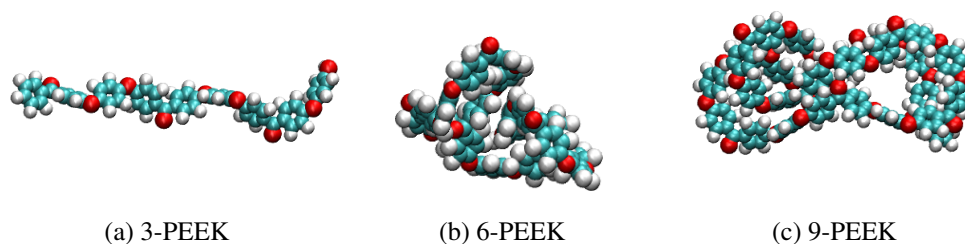
Figure 4.6: Final configurations of 3, 6 and 9-monomer PEEK chains modeled with the ReaxFF-lg version and the Nosé-Hoover thermostat

(a)   (b)
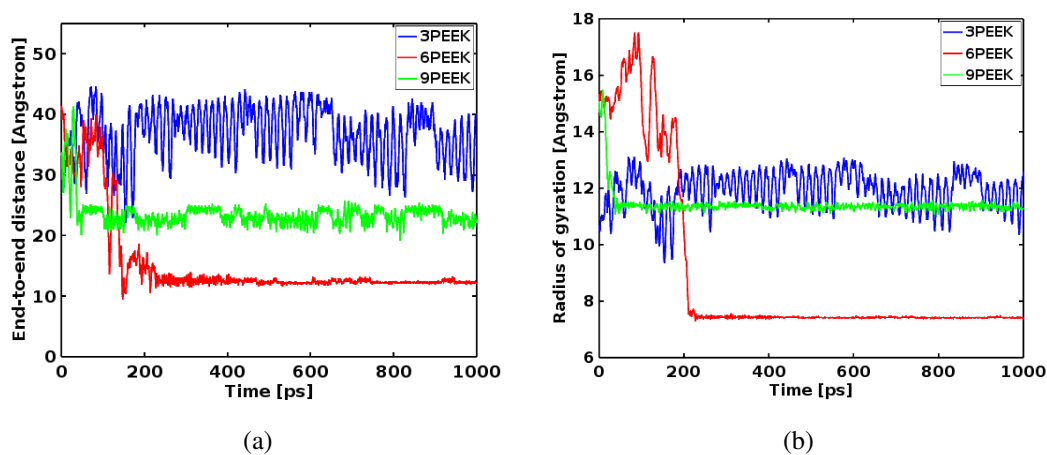
Figure 4.7: (a) End-to-end distance and (b) radius of gyration plots of 3, 6 and 9-monomer PEEK chains modeled with ReaxFF-lg version and the Nosé-Hoover thermostat

There are several important results that should be mentioned from the isolated polymer studies. As can visually be seen in Figure 4.6 and more quantitatively in Figure 4.7, the longer chains are more likely to fold than 3-monomer polymer. For this particular rendition, realized using the ReaxFF-lg version of the ReaxFF potential, the 6-monomer polymer exhibits the smallest radius of gyration, i.e. the largest degree of folding. Both the 6- and the 9-monomer polymers remain stable in their final configurations once they settle into it. The initial transitory period before the final configuration is found larger for the 6-monomer polymer. The behavior of the 3-monomer polymer, on the other hand, is very different. In addition to remaining extended for the entire duration of the simulation, it exhibits small extensional oscillations around an average length. The folding of the larger polymers occur in discrete steps as seen

57

in the potential energy plot of Figure 4.8 for the 6-monomer polymer.

For a comparison between the two versions of the ReaxFF potential, identical calculations were run with the ReaxFF$_{CHO}$ version, starting from the same initial configuration. The final configurations and the graphs of the end-to-end distance and the radius of gyration are presented in Figures 4.9 and 4.10 respectively. The behavior of the polymer chains were found to be similar varying degrees of folding observed at all lengths. However, in this case, the 6-monomer polymer was found to exhibit a more extended configuration while the 3- and 9-monomer polymers collapse into a more compact structure. The fine-scale oscillations are present for the both 3- and the 6-monomer polymers in this case.
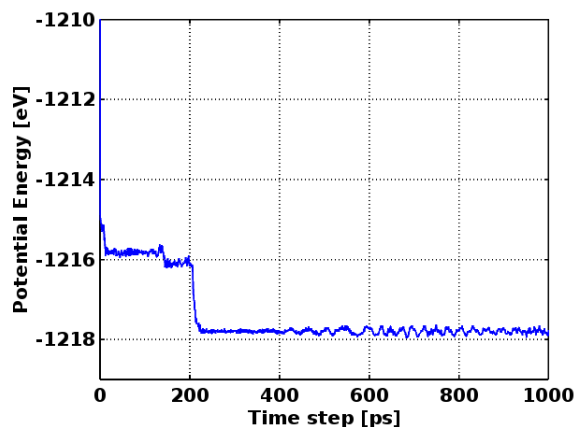
Figure 4.8: Potential energy plot of 6-monomer length PEEK chain modeled with ReaxFF-lg potential and the Nosé-Hoover thermostat

(a) 3-PEEK   (b) 6-PEEK   (c) 9-PEEK
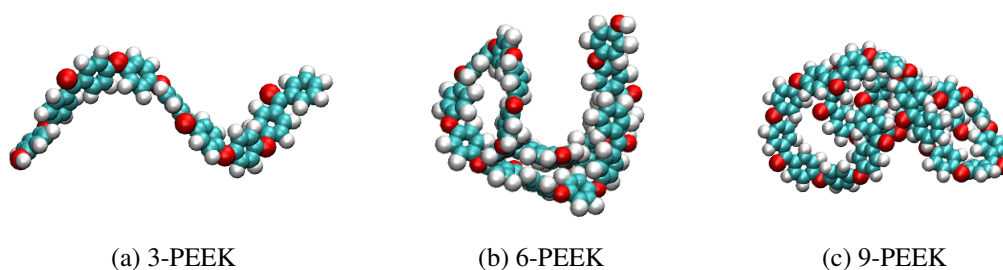
Figure 4.9: Final configurations of 3, 6 and 9-monomer PEEK chains modeled with ReaxFF$_{CHO}$ version and the Nosé-Hoover thermostat

58

(a)	(b)
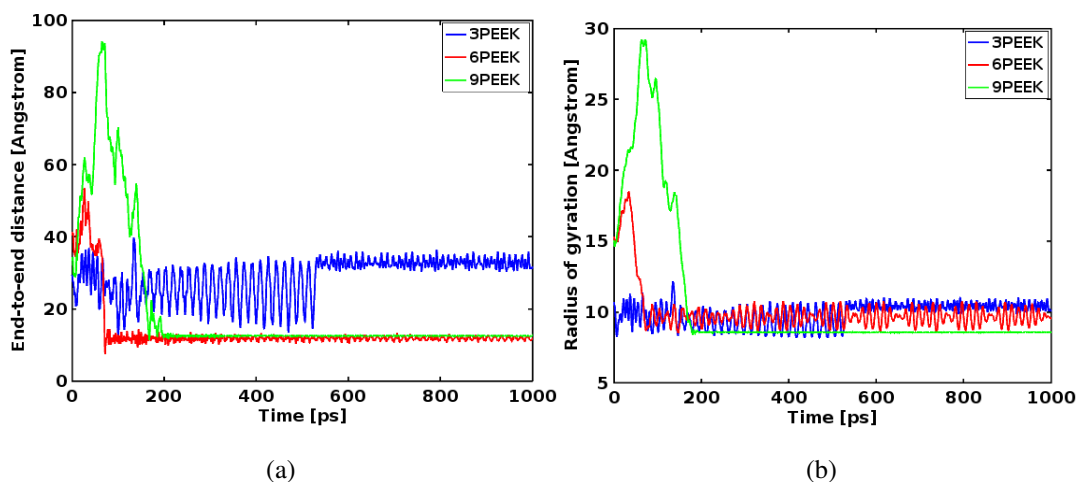
Figure 4.10: (a) End-to-end distance and (b) radius of gyration plots of 3, 6 and 9-monomer PEEK chains modeled with ReaxFF$_{CHO}$ version and the Nosé-Hoover thermostat

Having seen that the two different versions of the potential yield qualitatively similar results, we next explore the effects of the thermostat. In the next two subsections, we repeat the above calculations using two different thermostats and compare the results to those of Nosé-Hoover.

4.2.2 The Berendsen Thermostat

The results obtained with this thermostat are strikingly different from those of Nosé-Hoover. The final configurations and analyses of the calculations performed using the ReaxFF-lg version are displayed in Figures 4.11 and 4.12 while those for the ReaxFF$_{CHO}$ versions are presented in Figures 4.13 and 4.14. The first difference that can be mentioned is in the mode of the collapse. While in the Nosé-Hoover calculations, the folding is done via random coiling mechanism, in the results obtained with the Berendsen thermostat, the folded structures appear more ordered. In this final configurations obtained using the ReaxFF-lg version, bot the 6- and 9-monomer chains are organized in a spiral. For the ReaxFF$_{CHO}$ version, on the other hand, they form ultra-compact stacked structures that appear to be completely determined by the π-π interaction between the aromatic rings of the chains. The behavior of the two versions under this thermostat is therefore wildly different from one to another.

Another interesting result is the fact that these compact, stacked structures seen in the ReaxFF$_{CHO}$ version are reached very early in the simulation. Once the system is trapped in these configurations, it is locked with minimal oscillations.

(a) 3-PEEK   (b) 6-PEEK   (c) 9-PEEK
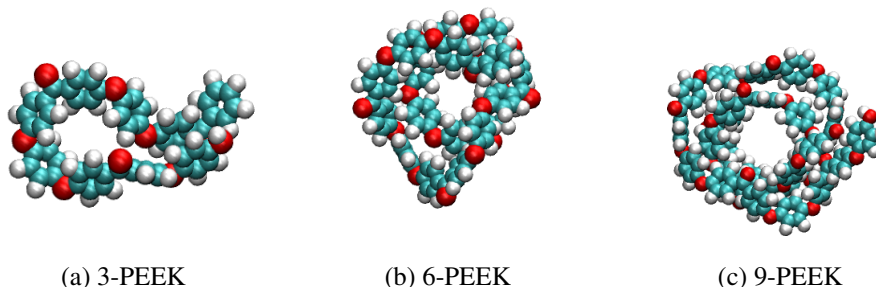
Figure 4.11: Final configurations of 3, 6 and 9-monomer PEEK chains modeled with ReaxFF-lg version and the Berendsen thermostat

(a)   (b)
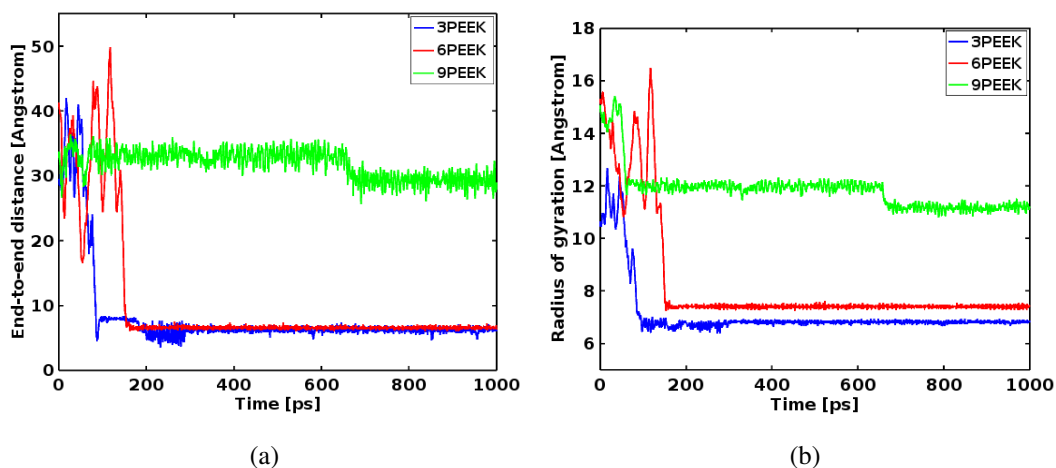
Figure 4.12: (a) End-to-end distance and (b) radius of gyration plots of 3, 6 and 9-monomer PEEK chains modeled with ReaxFF-lg version and the Berendsen thermostat

(a) 3-PEEK   (b) 6-PEEK   (c) 9-PEEK
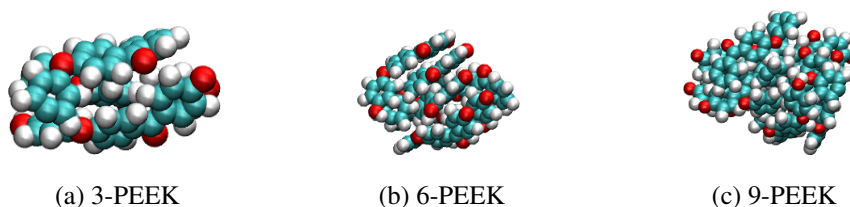
Figure 4.13: Final configurations of 3, 6 and 9-monomer PEEK chains modeled with ReaxFF$_{CHO}$ version and the Berendsen thermostat
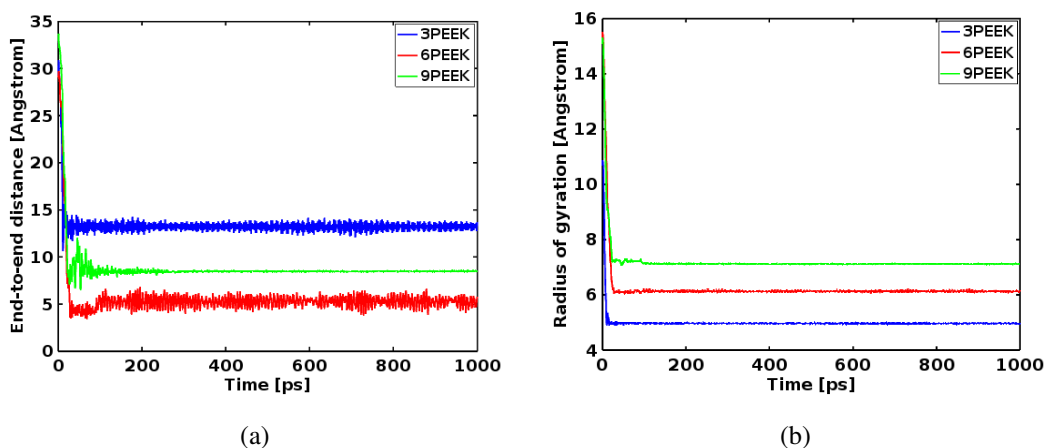
Figure 4.14: (a) End-to-end distance and (b) radius of gyration plots of 3, 6 and 9-monomer PEEK chains modeled with ReaxFF-lg version and the Berendsen thermostat

4.2.3 The Langevin Thermostat

In this section, we repeat our calculations one final time under the stochastic Langevin thermostat (results in Figures 4.15, 4.16, 4.17 and 4.18). Once again, the initial configurations are the same as the other two configurations. This thermostat surprisingly exhibits still more widely different behavior that the previous two. This time, the folding is significantly reduced. In fact, within the duration of the 1 ns simulation, the ReaxFF-lg version did not yield the folded structures. In the case of the Langevin thermostat, at variance with the other two cases, the flying ice cube artifact was not observed. However, the motion of the atoms were found to be rather restricted, as also be observed elsewhere [69]. For the ReaxFF$_{CHO}$ version, a higher degree of folding is observed, although still without a well-defined final state, in which the system is securely trapped.

(a) 3-PEEK   (b) 6-PEEK   (c) 9-PEEK
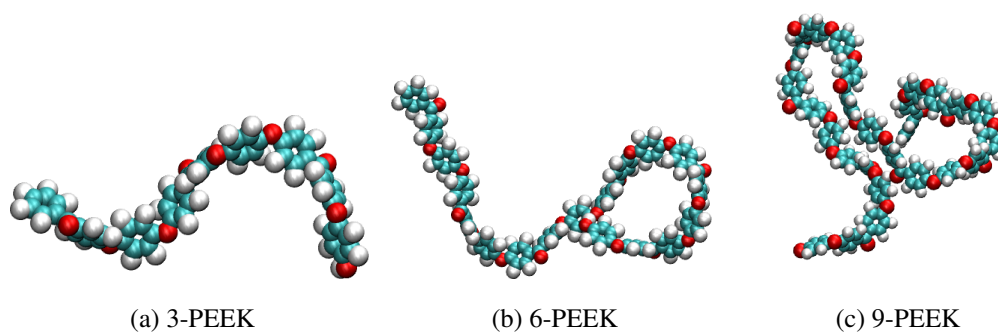
Figure 4.15: Final configurations of 3, 6 and 9-monomer PEEK chains modeled with ReaxFF-lg version and the Langevin thermostat

(a)   (b)
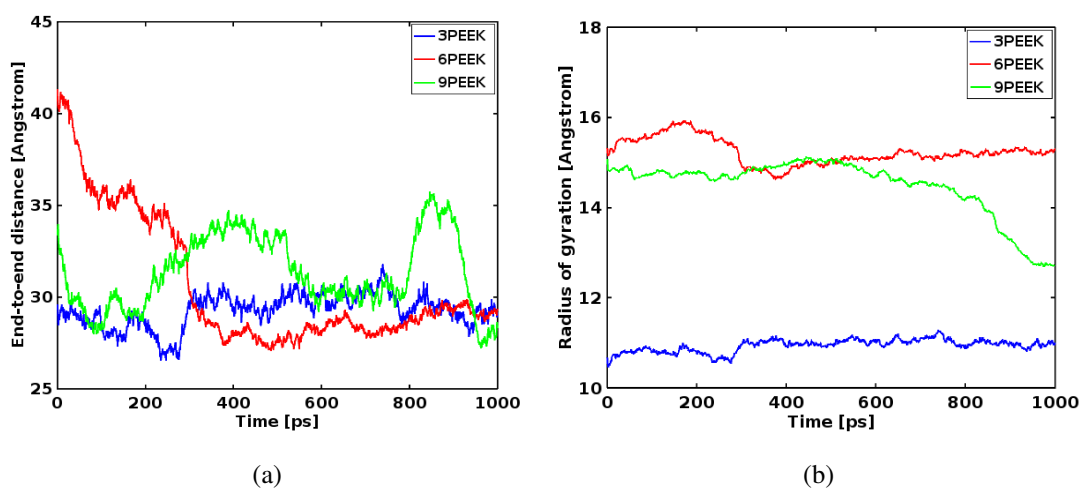
Figure 4.16: (a) End-to-end distance and (b) radius of gyration plots of 3, 6 and 9-monomer PEEK chains modeled with ReaxFF-lg version and the Langevin thermostat

(a) 3-PEEK   (b) 6-PEEK   (c) 9-PEEK
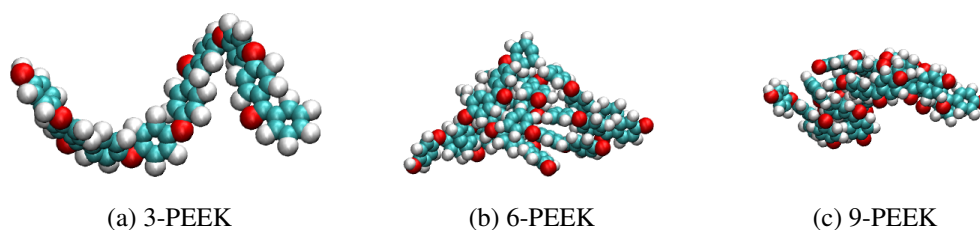
Figure 4.17: Final configurations of 3, 6 and 9-monomer PEEK chains modeled with ReaxFF$_{CHO}$ version and the Langevin thermostat

62
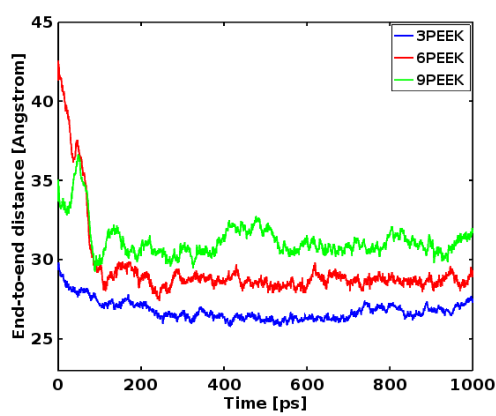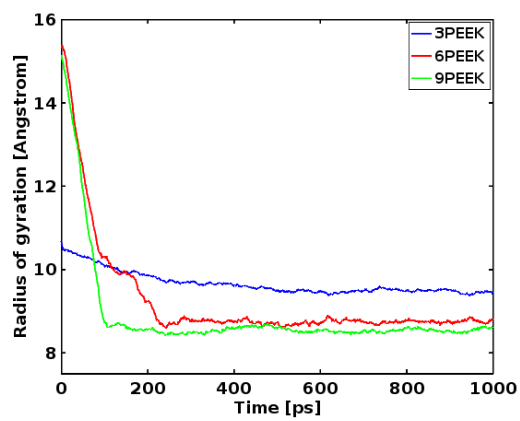
(a)	(b)

Figure 4.18: (a) End-to-end distance and (b) radius of gyration plots of 3, 6 and 9-monomer PEEK chains modeled with ReaxFF-lg version and the Langevin thermostat

4.2.4 Comparison of the thermostats

In this subsection, we present an overall comparison of the three thermostats in terms of temperature fluctuations (Figures 4.19-[**?**]) and tendency to fold. In the same context, we also present a comparison of the two versions of the ReaxFF potential. We first notice that in all cases, the temperature control is successful. After a very brief transient period, the average temperature reaches 10 K and oscillates around this value. Overall, the Berendsen thermostat exhibits the smallest fluctuations, followed closely by the Langevin thermostat. The fluctuations under the Nosé-Hoover scheme is significantly larger and worsens in many cases as the simulation advances. The differences in the amplitude of the fluctuations is much less pronounced, however, for the ReaxFF-lg version. This is counterintuitive since the ReaxFF-lg version also yields less compact structures. This difference may perhaps be attributed to the accumulation of numerical errors, however, more detailed studies would be necessary to come to a definitive conclusion.

(a) ReaxFF-lg   (b) ReaxFF$_{CHO}$
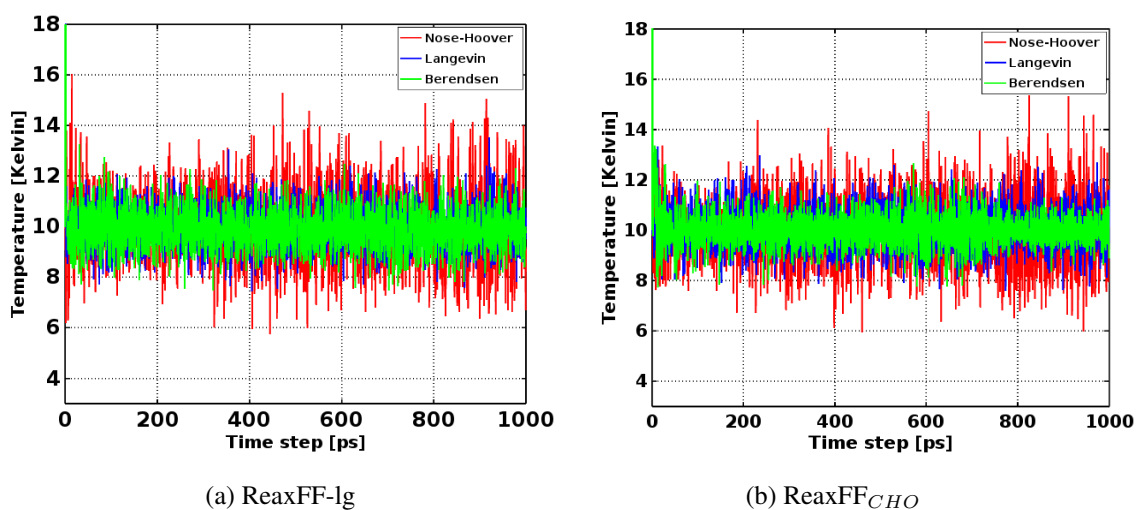
Figure 4.19: Temperature fluctuations of 3-monomer length PEEK chains with three different thermostats when (a) ReaxFF-lg and (b) ReaxFF$_{CHO}$ is used

(a) ReaxFF-lg
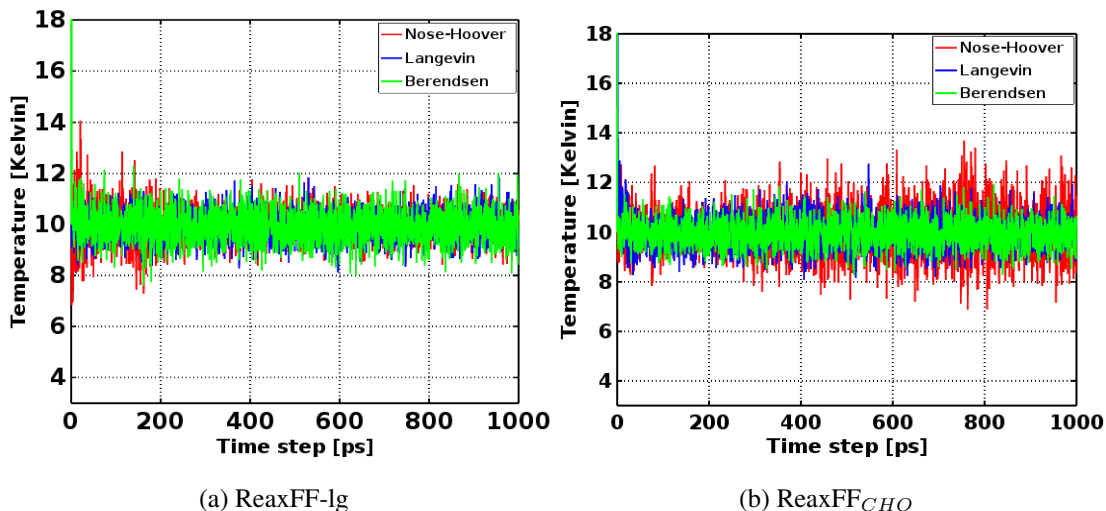
(b) ReaxFF$_{CHO}$

Figure 4.20: Temperature fluctuations of 6-monomer length PEEK chains with three different thermostats when (a) ReaxFF-lg and (b) ReaxFF$_{CHO}$ is used

(a) ReaxFF-lg
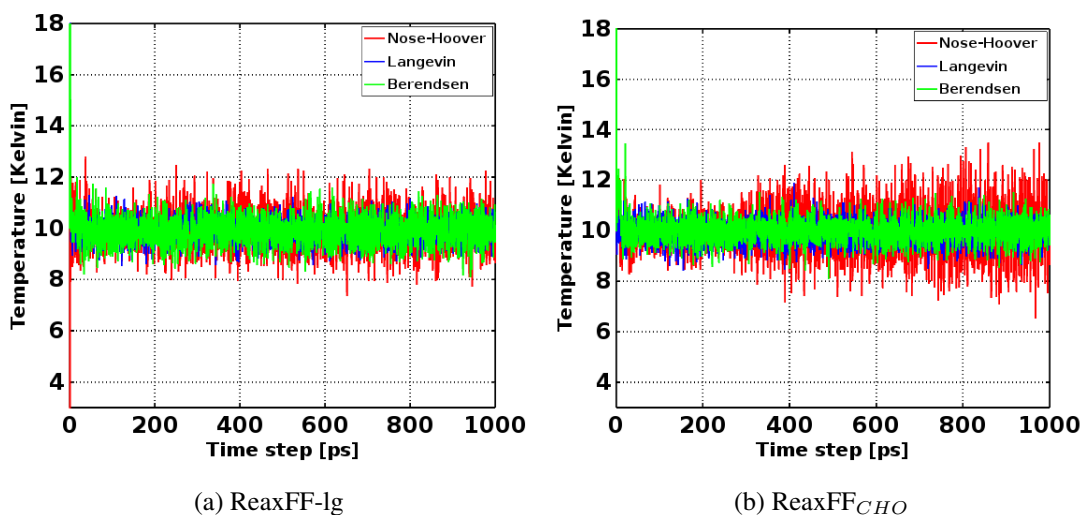
(b) ReaxFF$_{CHO}$

Figure 4.21: Temperature fluctuations of 9-monomer length PEEK chains with three different thermostats when (a) ReaxFF-lg and (b) ReaxFF$_{CHO}$ is used

In Figure 4.22, we present an example (6-monomer chain, ReaxFF-lg, Berendsen) of the fluctuation amplitude as a function of polymer length. As expected from basic thermodynamics, the relative size of the fluctuations are reduced as the atom number in the polymer increases. The differences are of course rather subtle due to low value of the temperature.
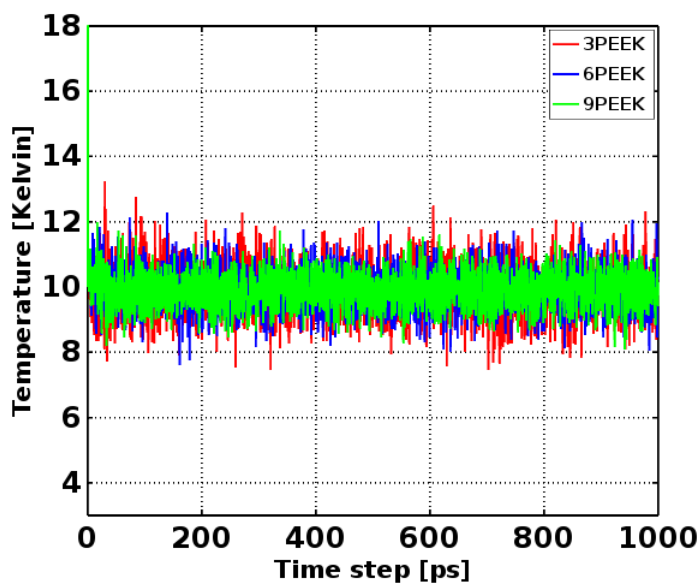
Figure 4.22: Temperature profiles of 3,6 and 9 monomer length PEEK modeled with ReaxFF-lg potential and Berendsen thermostat

Table 4.1: Folding of PEEK chains

	N-H		Berendsen		Langevin	
	LG	CHO	LG	CHO	LG	CHO
3-PEEK	✗	✗	✓	✓	✗	✗
6-PEEK	✓	✓	✓	✓	✗	✓
9-PEEK	✓	✓	✓	✓	✗	✓

We conclude this part on the comparison of thermostats with some final remarks. Surprisingly, the folding tendency of the polymers appear to be dependent upon the choice of the thermostat. A summary of this is given in Table 4.1 where whether the polymer is folded at the end of the simulation is indicated with a check or a cross. In the majority of the cases, folding occurs. A stark exception is the Langevin thermostat used in tandem with the ReaxFF-lg flavor where the final structures are extended for all lengths. The Langevin stochastic thermostat does not cause the Flying ice cube problem as the Nosé-Hoover and Berendsen thermostats. This unphysical phenomena was prevented by periodically removing linear and angular momentum of the system. On the other hand, when the Langevin thermostat is used, atoms move restrictedly.

66

In longer polymer chains, additional folds can provide a further decrease in the energy [83]. As seen from our results, when the chain length is increased from 3 to 9 monomer, chain foldings occur more than once. In some cases, ReaxFF$_{CHO}$ together with the Berendsen and Langevin thermostat, apart from folding, chain aggregation was observed. The importance of this aggregation extends beyond the CNT/polymer interface into the modelling of the bulk polymer. Due to this tendecy to aggregate, model polymer matrices may develop an unreasonably porous structure under strain. An example is provided here from our own calculations (Figure 4.23).

(a)   (b)
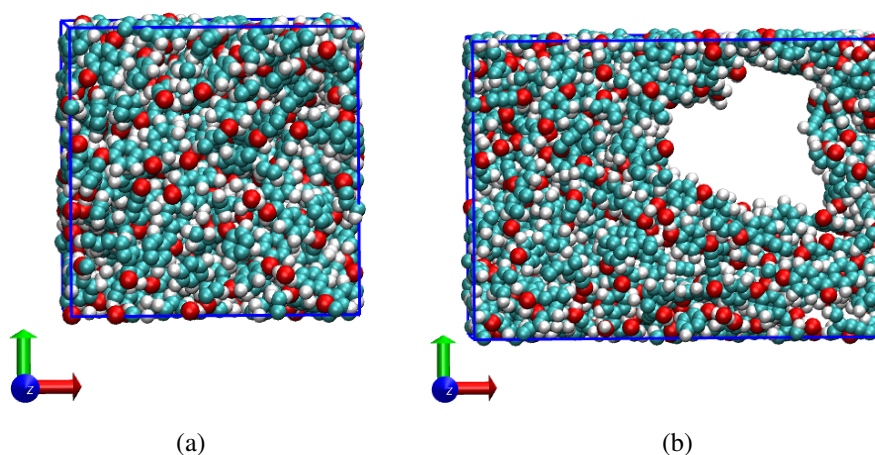
Figure 4.23: Bulk PEEK modeled with Berendsen thermostat and ReaxFF$_{CHO}$ potential at 300K. (a) Equilibrated (b) Strain applied

Since the Berendsen thermostat is the most preferred algorithm together with the ReaxFF and it reduces the magnitude of temperature oscillations, thereby provides more stability [69], we decided to move on our calculations with the Berendsen thermostat together with the ReaxFF-lg version, that is earlier reported to successfully estimates mechanical properties of PEEK [24].

4.2.5   Rod-like Configuration of 3, 6 and 9 monomer PEEK chains

To further investigate the dependence on initial configuration on folding behavior of polymer chains, in this part, PEEK chains are created by using the rod-like configuration option with 0° fixed torsion angles in the nanoHUB Polymer Modeler tool as shown in Figure 4.24. This option maximizes the alignment of the monomers in the polymer chain. This time only the Berendsen thermostat was used with the ReaxFF-

lg potential. Final configurations of chains are shown in Figure 4.25.
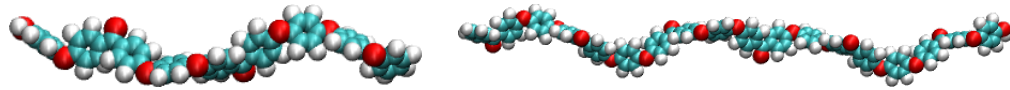
(a) 3 momomer PEEK chain with 104 atoms   (b) 6 momomer PEEK chain with 206 atoms
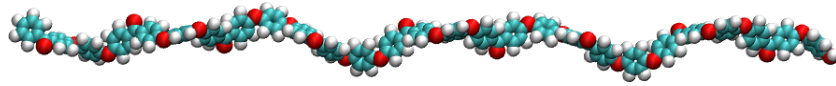
(c) 9 momomer PEEK chain with 308 atoms

Figure 4.24: 3, 6 and 9 monomer PEEK chains created via nanoHUB Polymer Modeler tool [81] by using rod-like configuration option with $0°$ fixed torsion angles

Folding of chains was observed in all three lengths of PEEK chain as can be concluded from their end-to-end distance and radius of gyration plots given in Figure 4.26. These results indicate that folding of polymer chains is independent from their initial configurations at least for this thermostat. The radius of gyration for the polymer is similar to the previous set of initial conditions, although in this case, it takes a longer time to find this final configuration. This is expected since the initial condition represents an extreme limit of extension.
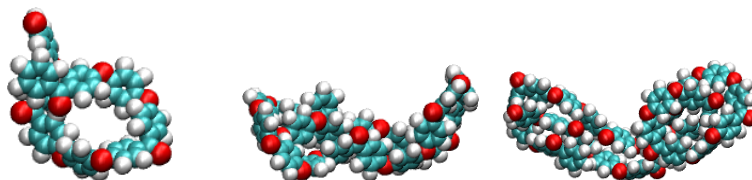
(a) 3-PEEK   (b) 6-PEEK   (c) 9-PEEK

Figure 4.25: Final configurations of rod-like PEEK chains

(a)	(b)
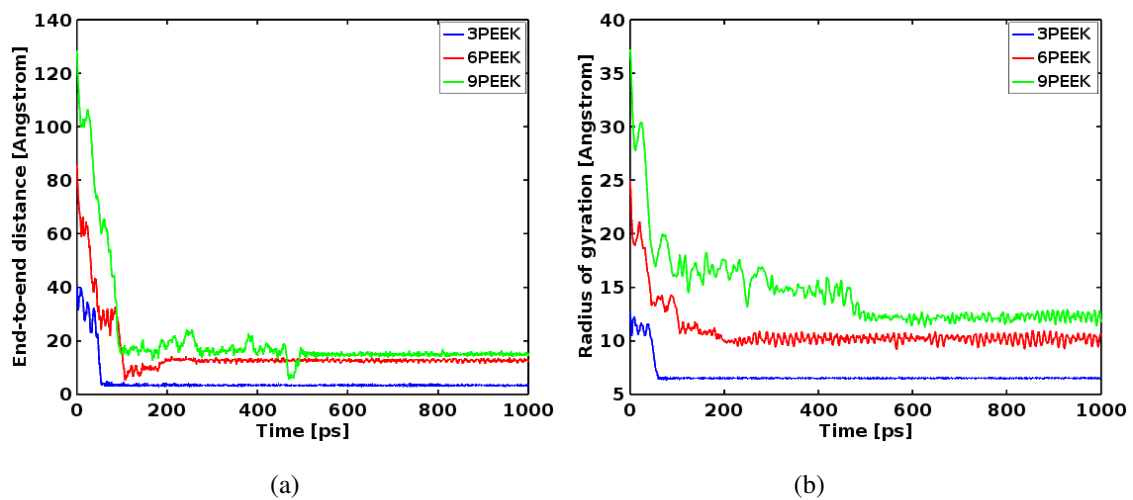
Figure 4.26: (a) End-to-end distance and (b) radius of gyration graphs of 3, 6 and 9-monomer length rod-like PEEK chains

CHAPTER 5

CNT/PEEK INTERFACE

Up to this point in the thesis, we have presented mechanical properties of CNTs with different interatomic potentials under static and dynamical loadings varying the relevant parameters such as chain length, thermostats and potentials. As stated previously, the interfacial properties of the CNT and the polymer strongly affect the mechanical properties of nanocomposite material. In this chapter, we aim to examine the CNT/PEEK interface by using both DFT and MD techniques to lead up to development of their nanocomposites.

5.1 Covalent and Non-covalent Functionalization

As CNTs are used as reinforcing materials in polymer nanocomposites, investigation of the interfacial properties is very crucial for understanding the load transfer between the CNT and polymer components. The interaction between the CNT and the polymer may be realized via covalent [85] or non-covalent [87] bonding. In particular, longer-chain polymers have the ability to wrap around the CNT, forming particularly stable interfaces. Introducing defects on the CNT can induce covalent bonding between CNT and polymer, however, this can cause a deterioration of the mechanical properties [86]. Therefore, noncovalent functionalization is generally preferred when reinforcing mechanical properties of polymer matrices. In addition to the application at hand, it is reported that non-covalent wrapping of polymer chains around CNTs can be used to increase solubility of CNTs in any solvent and organize CNT dispersion in matrix materials [95]. As a means of systematically characterizing the interface and the extent of the noncovalent interactions, we first investigated a single monomer of

PEEK on breaking it down to its constituent aromatic rings on CNTs of different radii and chiralities. The relevant adsorption energies are calculated by using both DFT and MD calculations. ReaxFF-lg was used in all the MD calculations in this chapter. Even though ReaxFF originally developed with an aim to describe reactive cases, its domain was extended to various studies including non-reactive cases [89]. In literature, there are several studies treating CNT/Polymer interface with the ReaxFF [88]. To complement and extend these studies and to ensure that the MD studies utilizing this new parametrization are accurate,we conduct a preliminary benchmark study. Our aim here is to compare DFT results of PEEK sub-units and its monomer with ReaxFF to ensure the accuracy of MD results. Furthermore, this study provides clues regarding the possible anchoring points of the polymer on the CNT ans a way to gain insight into the mechanism of wrapping around the CNT.

5.2 DFT Calculations

We start by dividing the PEEK monomer into its sub-units and studying the interaction of each subunit separately with the CNT. In Figure 5.1, the three subunits of the PEEK are seen, namely the benzene-like ring shown with label 3, $C_6H_4O_2$ ring labeled 1 and $C_6H_6O_2$ between them with label 2. We begin our investigations by calculating the DFT adsorption energies of these three subunits of the PEEK monomer shown in Figure 5.2. Rings are placed 3 Å above the 3-unit cell (10,0) zigzag CNT with length 13.05 Å and rotated by 30°, 60° and 90° to find most favorable configuration as shown in Figures 5.3, 5.4 and 5.5. The adsorption energies were performed according to the formula

$$E_{ads} = E_{system} - E_{CNT} - E_{molecule} \tag{5.1}$$

where E_{ads} is the adsorption energy, E_{system} , E_{CNT} and $E_{molecule}$ are the energies of the system, CNT and molecule respectively. The Quantum Espresso code suite was used with the vdW-DF-C09 functional. The kinetic energy cut-off was set to 30 Ryd and a 1x1x8 k-point mesh was used. Adsorption energies and average distances are given in Table 5.1. It can be seen that 90° rotated configuration has the highest binding energy with the lowest distance.

Also, due to symmetry of benzene ring, 0° and 60° configuration have the same ge-
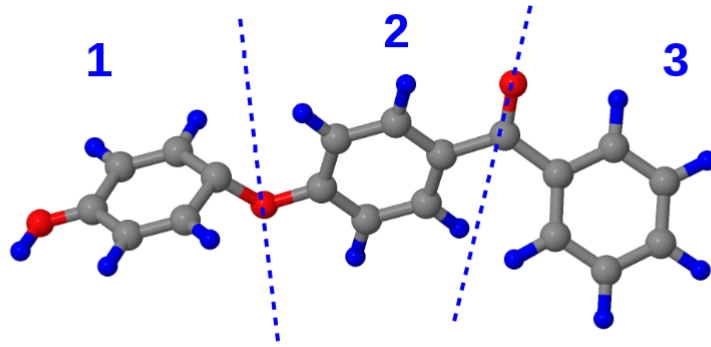
Figure 5.1: Rings of PEEK monomer. Carbons are represented with gray, hydrogens are blue and oxygens are red.

(a) C_6H_6 ring

(b) $C_6H_4O_2$ ring
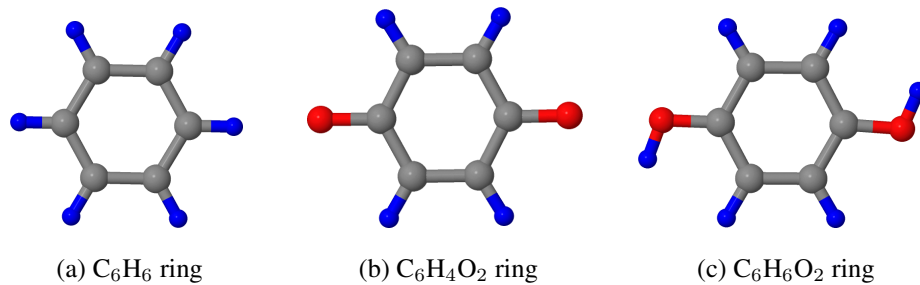
(c) $C_6H_6O_2$ ring

Figure 5.2: Geometries of (a) C_6H_6 ,(b) $C_6H_4O_2$, (c) $C_6H_6O_2$ molecules

(a) Initial

(b) 30° rotated

(c) 60° rotated
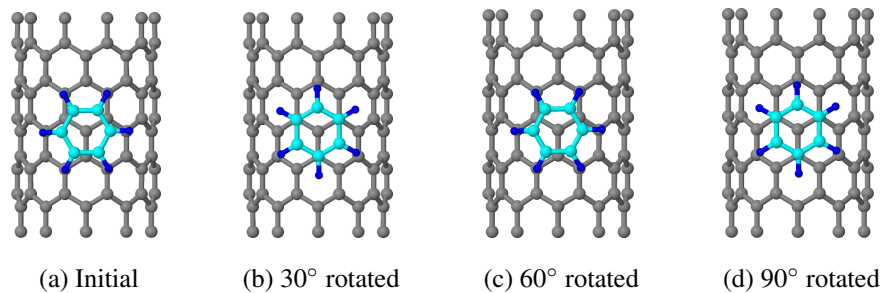
(d) 90° rotated

Figure 5.3: Initial, 30°, 60° and 90° rotated configurations of C_6H_6 ring on (10,0) zigzag CNT

ometry and almost same adsorption energy. Same conclusion can be made for 30° and 90° configurations as well.

Next, the adsorption energies of $C_6H_4O_2$ unit was calculated by using the same procedure. The results are given in Table 5.1. The initial configuration is the most favorable configuration for this case and adsorption energies are higher than that of benzene due to the existence of oxygen atoms.

(a) Initial   (b) 30° rotated   (c) 60° rotated   (d) 90° rotated
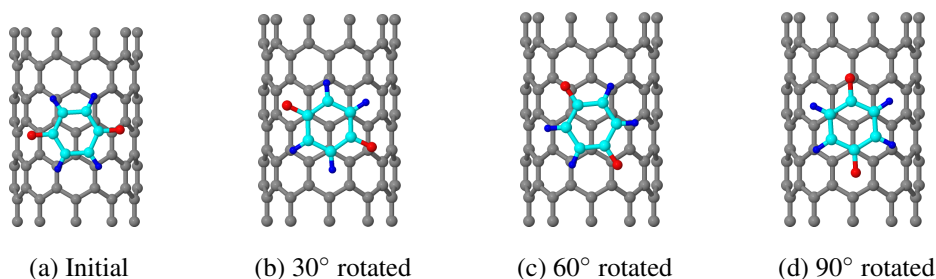
Figure 5.4: Initial, 30°, 60° and 90° rotated configurations of $C_6H_4O_2$ ring on (10,0) zigzag CNT

Last, $C_6H_6O_2$ sub-unit was placed on CNT as shown in Figure 5.5 to calculate adsorption energies. 90° rotated configuration is the favorable case and as compared with the other two sub-units, $C_6H_6O_2$ has highest adsorption energies in all its configurations due to its atom number. The adsorption energies of $C_6H_6O_2$ molecule are also given in Table 5.1.

(a) Initial   (b) 30° rotated   (c) 60° rotated   (d) 90° rotated
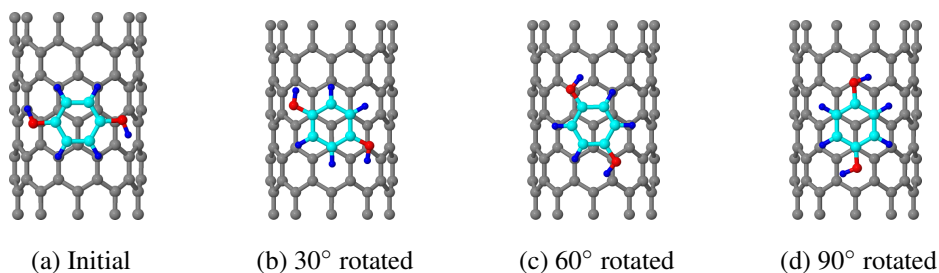
Figure 5.5: Initial, 30°, 60° and 90° rotated configurations of $C_6H_6O_2$ ring on (10,0) zigzag CNT

As evidenced by the significantly larger adsorption energies of the oxygen-containing sub-units, the adsorption geometries of the full PEEK polymers are expected to be dictated by the orientations of the oxygens. As expected, the interactions between the π-systems of the sub-units and the CNT result in rather high overall adsorption energy values. This tendency of the molecules to assume a flat orientation with respect to the

Table 5.1: Adsorption energies of C_6H_6, $C_6H_4O_2$ and $C_6H_6O_2$ ring on (10,0) zigzag CNT

	C_6H_6		$C_6H_4O_2$		$C_6H_6O_2$	
	E_A [meV]	d [Å]	E_A [meV]	d [Å]	E_A [meV]	d [Å]
0°	-447.3	3.4900	**-518.72**	3.4438	-539.11	3.4133
30°	-449.4	3.4917	-483.06	3.4684	-560.92	3.4033
60°	-446.9	3.4633	-516.00	3.4411	-576.32	3.4083
90°	**-450.2**	3.4067	-492.19	3.4822	**-580.33**	3.4133

CNT is expected to be in competition with the energy penalty to be paid when the H atoms of the neighboring subunits are in proximity to each other, as discussed in the previous section.

5.2.1 Full PEEK monomer on CNTs with different length, radius and chirality

The effect of length

In order to investigate the effect of length on the adsorption energies, PEEK monomer on (10,0) zigzag CNT with three different lengths are examined. Three different lengths used can be seen in Figure 5.6.

(a) PEEK on 13.05 Å CNT   (b) PEEK on 21.75 Å CNT   (c) PEEK on 26.01 Å CNT
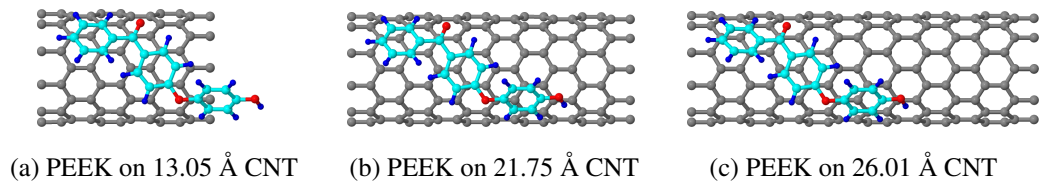
Figure 5.6: PEEK monomer on top of (10,0) CNT with 3 different length

The initial configuration of the PEEK is taken from a 1 ns MD simulations at 10K to reduce the computational cost of DFT simulations since the systems investigated

here have large number of atoms (156, 236 and 276 atoms). The adsorption energy results are given in the Table 5.2. Going from the smallest length to the next larger, we observe a decrease of approximately 0.08 eV in the adsorption energy. This is due to the reduction in the lateral interaction between the periodic copies of the molecule. For the two larger sizes, however, the lateral interactions have already been eliminated and there are no significant changes.

Table 5.2: Adsorption energies of full PEEK monomer on (10,0) zigzag CNT with three different lengths

System	156-atoms	236-atoms	276-atoms
L_z [Å]	13.05	21.75	26.01
E_A [eV]	-1.3518	-1.2743	-1.2841

The effect of radius

To investigate the effect of radius, adsorption energies of (10,0), (12,0) and (15,0) CNTs with length 26.01 Å, whos side and front views are given in Figures 5.7 and 5.8, are calculated and results are given in Table 5.3. Similarly, the initial configuration of the PEEK monomer on top of CNTs are taken from the MD simulations. Although increasing diameter appears to result in substantially increasing energies as shown in Figure 5.9, the difference may also be due to the different initial conditions determined by the MD calculation. Further study is needed to confidently establish the relation between the adsorption energies and radius.

(a) PEEK on (10,0) CNT   (b) PEEK on (12,0) CNT   (c) PEEK on (15,0) CNT
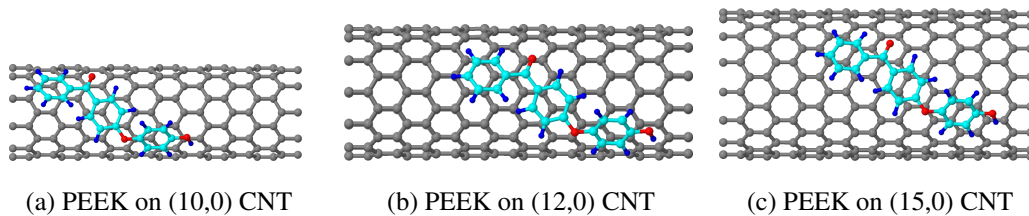
Figure 5.7: PEEK monomer on 3 different zigzag CNTs (side view)

(a) PEEK on (10,0) CNT   (b) PEEK on (12,0) CNT   (c) PEEK on (15,0) CNT
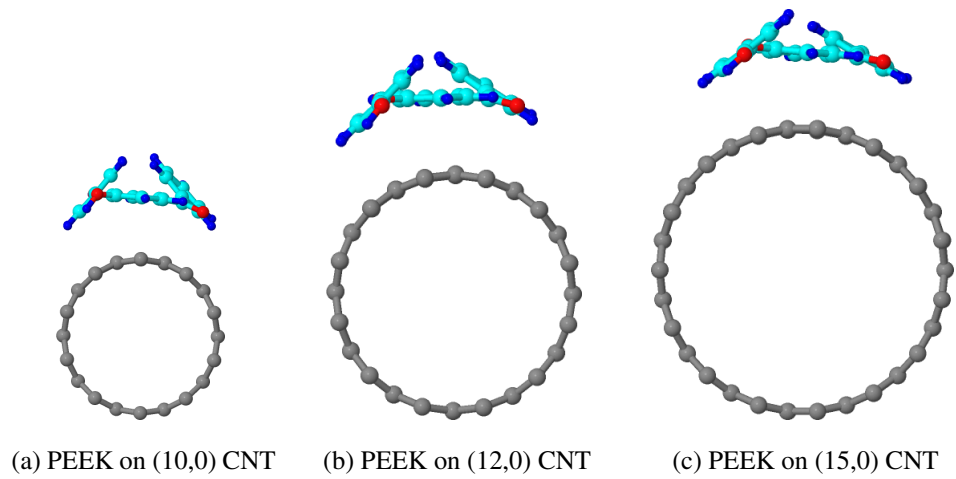
Figure 5.8: PEEK monomer on 3 different zigzag CNTs (front view)
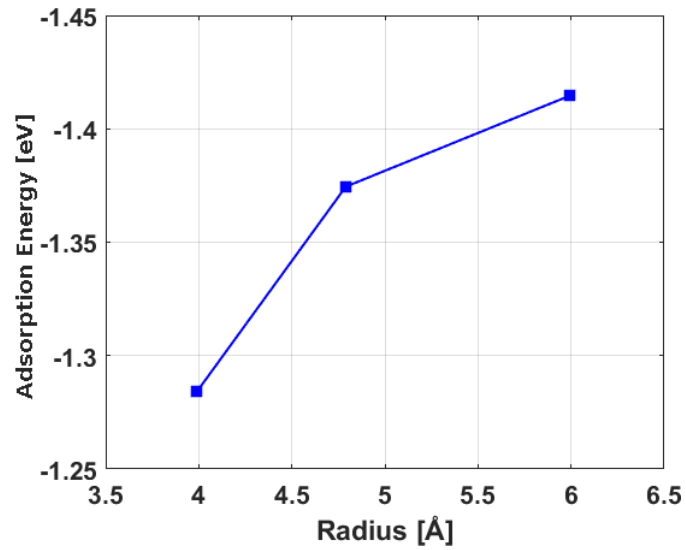
Figure 5.9: Radius versus adsorption energy graph of 3 different zigzag CNTs

Table 5.3: Adsorption energies of full PEEK monomer on (10,0) zigzag CNT with three different diameters

CNT	(10,0)	(12,0)	(15,0)
Radius [Å]	3.99	4.79	5.99
E_A [eV]	-1.2841	-1.3745	-1.4145

77

The effect of Chirality

The geometry of a CNT can also affect its interaction with molecules. To examine this effect, as well as validate the effect of radius, we select three armchair CNTs whose radii are nearly equal to that of previously studied (10,0), (12,0) and (15,0) respectively. The axial lengths are also kept the same. Side and front views of selected armchair CNTs can be seen in Figures 5.10 and 5.11. For both zigzag and armchair cases, results show clear dependence radius of CNTs as in Tables 5.3 and 5.4. Since CNTs of larger radii have larger surface area, polymer sustain larger surface that results in higher adsorption energies. Hence, one can make a conclusion that larger CNTs are more useful to be used as a reinforcer materials [95].

(a) PEEK on (6,6) CNT   (b) PEEK on (7,7) CNT   (c) PEEK on (8,8) CNT
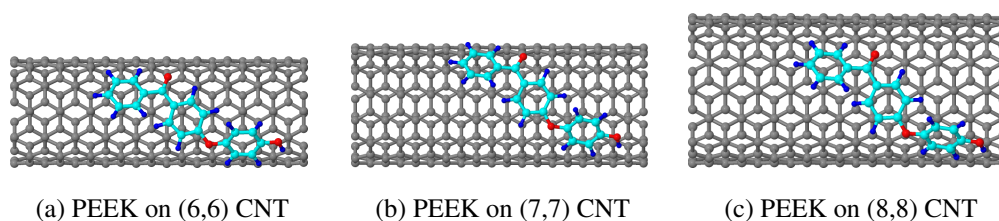
Figure 5.10: PEEK monomer on armchair CNTs with 3 different radius and length 25.01 Å (side view)

(a) PEEK on (6,6) CNT   (b) PEEK on (7,7) CNT   (c) PEEK on (8,8) CNT
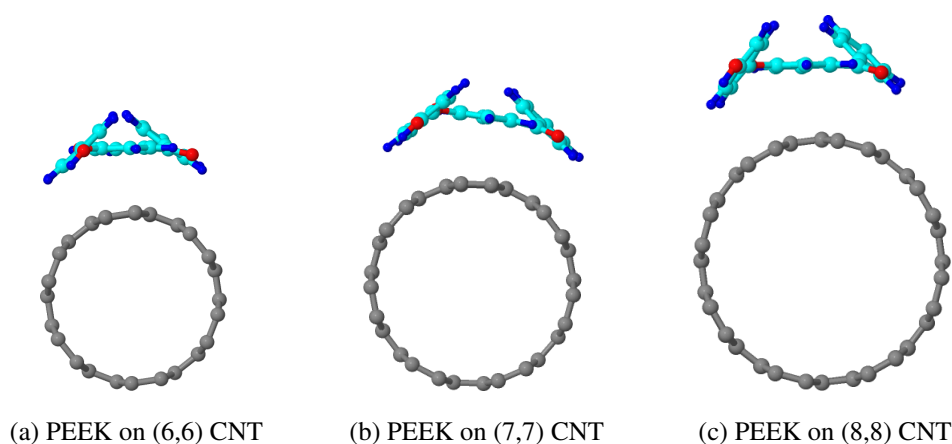
Figure 5.11: PEEK monomer on armchair CNTs with 3 different radius and length 25.01 Å (front view)

Table 5.4: Adsorption energies of full PEEK monomer on 3 different armchair CNTs

CNT	(6,6)	(7,7)	(8,8)
Radius [Å]	4.15	4.84	5.53
E_A [eV]	-1.3702	-1.555	-2.114

Because of the different geometry of zigzag and armchair CNTs, their diameters cannot exactly be the same. This small differences in their diameter cause difference in their adsorption energies [95].

Results indicate that adsorption energies of armchair CNTs are higher than the ones of zigzag type CNTs.

5.3 MD Calculations

5.3.1 CNT/Sub-units and CNT/PEEK-monomer Interfaces

In our CNT/PEEK interface MD calculations, first, sub-units on CNT and CNT/PEEK monomer adsorption energies were calculated at 0K, 100K and 300K. In the 0K calculations, after minimization of the system, final configurations of constitutive parts namely, the CNT and the adsorbate of the composite system were separated and their static energies at the final step are taken and adsorption energy was calculated by using the Eq. 5.1.

Following the static calculations, CNT/sub-units and CNT/PEEK monomer adsorption energy calculations at 100K and 300K were performed in the NVT ensemble by using the ReaxFF-lg [62] force field. Sub-molecules of PEEK and full PEEK monomer were allowed to interact with CNT during 200 ps with a 0.1 fs time step. Periodic boundary conditions were applied in all dimensions. All equation of motions were integrated by using a velocity Verlet algorithm in the LAMMPS code and constant temperature is achieved by the Berendsen thermostat algorithm with a damping factor of 100 (in time units) meaning that thermostat is activated every 10 fs during the simulation. The potential energy of the system is averaged using the last 50 ps

of the simulation and potential energies of the polymer and the CNT are taken from the last step of the simulation. This protocol will be called unfixed CNT case hereupon in the text for short. In Table 5.5, ReaxFF and DFT adsorption energy results of sub-molecules on 13.05 Å CNT is given.

Table 5.5: Adsorption energies (in meV) of sub-molecules on 13.05 Å (10,0) zigzag CNT

System	DFT	ReaxFF		
		T=0K	T=100K	T=300K
CNT/C_6H_6	-450.2	-590.8	-578.7	-361.19
CNT/$C_6H_4O_2$	-518.72	-578.1	-589.94	-716.76
CNT/$C_6H_6O_2$	-580.33	-597.38	-553.41	-352.01

The ReaxFF calculations at 0 K and 100 K gave quite similar results with the DFT, However, while the adsorption energy of $C_6H_4O_2$ molecule considerably increases with increasing temperature in the ReaxFF calculations, exactly opposite trend is observed for the other two molecules. Similarly, length, radius and chirality dependence of the full PEEK adsorption energies were computed at three temperatures mentioned and compared to our previous DFT results. The results are given in Table 5.6. According to this table, ReaxFF results at 0 K and 100 K show very good agreement with the DFT results. At the higher temperature of 300 K, the adsorption energy for the smallest length is significantly larger than the lower temperatures. This difference attributed to the increased mobility of the monomer and the resulting ability to find more stable adsorption configurations. For the two larger lengths, however, the adsorption energies (indicated bold in Table 5.6) were found to be much lower. The reasons behind this discrepancy will be discussed later in the text.

In Table 5.7, all adsorption energies were calculated with different chirality/radius are given. The zigzag and armchair CNTs are taken to be 26.01 Å and 25.1 Å in length, respectively, chosen so that these two types of CNTs are nearly equal in length. The ReaxFF results at 0 K and 100 K temperature show very good agreement with DFT results as shown in Figure 5.12 with a very slight overestimation. As in the previous calculations, there appear lower adsorption energy results at the temperature of 300

Table 5.6: Adsorption energies (in eV) of full PEEK monomer on (10,0) zigzag CNT (unfixed) with different lengths

L_{CNT}	DFT	ReaxFF		
		T=0K	T=100K	T=300K
13.05	-1.3518	-1.4207	-1.4241	-1.6526
21.75	-1.2743	-1.3548	-1.4128	**-0.9255**
26.01	-1.2841	-1.3520	-1.4137	**-0.9955**

K in some cases (shown in bold in Table 5.7). The reason behind this decrease will be discussed later.

Table 5.7: Comparison of the interaction energies of full PEEK monomer on unfixed CNTs with different radius calculated with DFT and MD techniques

	DFT	**ReaxFF**		
		T=0K	T=100K	T=300K
(10,0)	-1.2841	-1.3520	-1.4137	**-0.9955**
(12,0)	-1.3745	-1.4527	-1.5572	-1.5417
(15,0)	-1.4145	-1.5477	-1.6321	-1.8294
(6,6)	-1.3702	-1.4022	-1.4473	**-0.9801**
(7,7)	-1.555	-1.4844	-1.5466	**-1.0580**
(8,8)	-2.111	-1.5182	-1.5875	-1.5770

According to the results given in the Table 5.7, a dependence on the diameter of CNT in the adsorption energies is observed. As the radius of a CNT increases, its curvature decreases and provide a better settlement to the monomer on CNT that results in higher adsorption energies [94, 95, 96]. On the other hand, no direct temperature dependence is observed in some results. While adsorption energies increase with increasing temperature for the (15,0) CNT, for other CNTs a decrease in adsorption energy is observed from 100 K to 300 K. In Table 5.7, a different final configuration of PEEK monomer on top of CNT (shown in Figure 5.13) is observed in adsorption
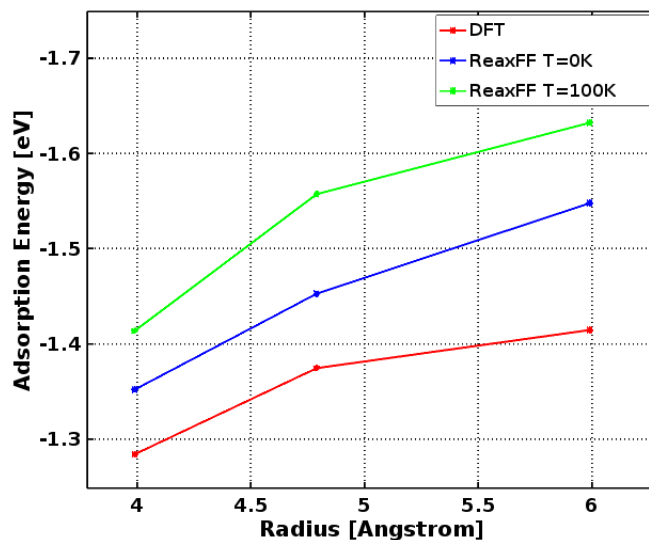
Figure 5.12: Adsorption energies of zigzag CNTs with increasing radius calculated by using DFT and ReaxFF

energies shown in bold. In the Mode 1 configurations, the ring in the middle of the PEEK monomer tends to align with the axial CNT axis and the position of other portions of the monomer are tilted. On the contrary, in the Mode 2 configurations, the middle ring of the PEEK monomer is also tilted. The distance between the Mode 2 configurations of PEEK monomer with CNT is larger than the Mode 1 ones, therefore, this can cause a decrease in the interaction energies. Here, we observe the competition between π-π interaction of between the CNT and the subunits of the monomer and the angular energy penalty associated with the relative orientation of the subunits with respect to each other. This issue was covered in Chapter 4. At 100 K, PEEK monomer on all different CNTs can be found in the configuration labeled Mode 1 in Figure 5.13 (a) while at 300 K some of the final configurations of PEEK are in Mode 2. Increase in temperature can trigger a new minimum configuration for these cases.

In MD calculations, performed with the Berendsen thermostat, temperatures of CNT and PEEK were monitored separately during the simulation. It was observed that while the temperature values of the system are around the desired values, the temperature of the PEEK monomer is much lower. As an example, when system is at 100K, temperature of the PEEK is around 20K. Nosé-Hoover and Langevin thermostats

(a) Mode 1	(b) Mode 2
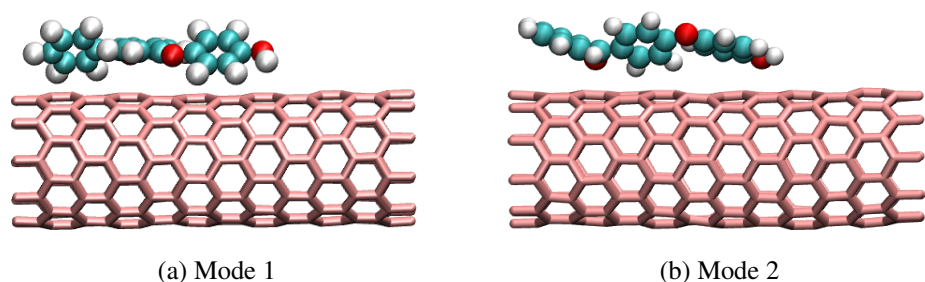
Figure 5.13: 2 different configuration of PEEK monomer on top of (10,0) CNT. Figure (a) shows the final configuration observed at 100 K and Figure (b) shows the one at 300 K

were also tested to check the separate temperatures of CNT and PEEK components. While the same behavior is observed in the Nosé-Hoover thermostat, in the Langevin thermostat both CNT and PEEK temperatures reach the desired values with very large fluctuations of the PEEK monomer. Temperature plots of these three thermostats are given in Figure 5.14. As a comparison, the adsorption energies of the PEEK monomer on top of (15,0) CNT is calculated by using these three thermostat algorithms and results are given in Table 5.8. It can be seen that the Langevin thermostat gives the lowest adsorption energy result while the Berendsen gives the highest. Since the Berendsen thermostat is the most commonly used temperature control algorithm with the ReaxFF and the Langevin thermostat cause restricted movements of atoms later result in no wrapping of PEEK chains around CNT, we proceed our MD calculations with the Berendsen thermostat and continue to address the temperature problem in different ways rather than switching to a different thermostat.

Table 5.8: Adsorption energies of full PEEK monomer on (15,0) zigzag CNT with different thermostats

Thermostat	E_b [eV]
Nosé-Hoover	-1.5242
Berendsen	-1.6321
Langevin	-1.4360

(a) Berendsen Thermostat (b) Nosé-Hoover Thermostat

(c) Langevin Thermostat
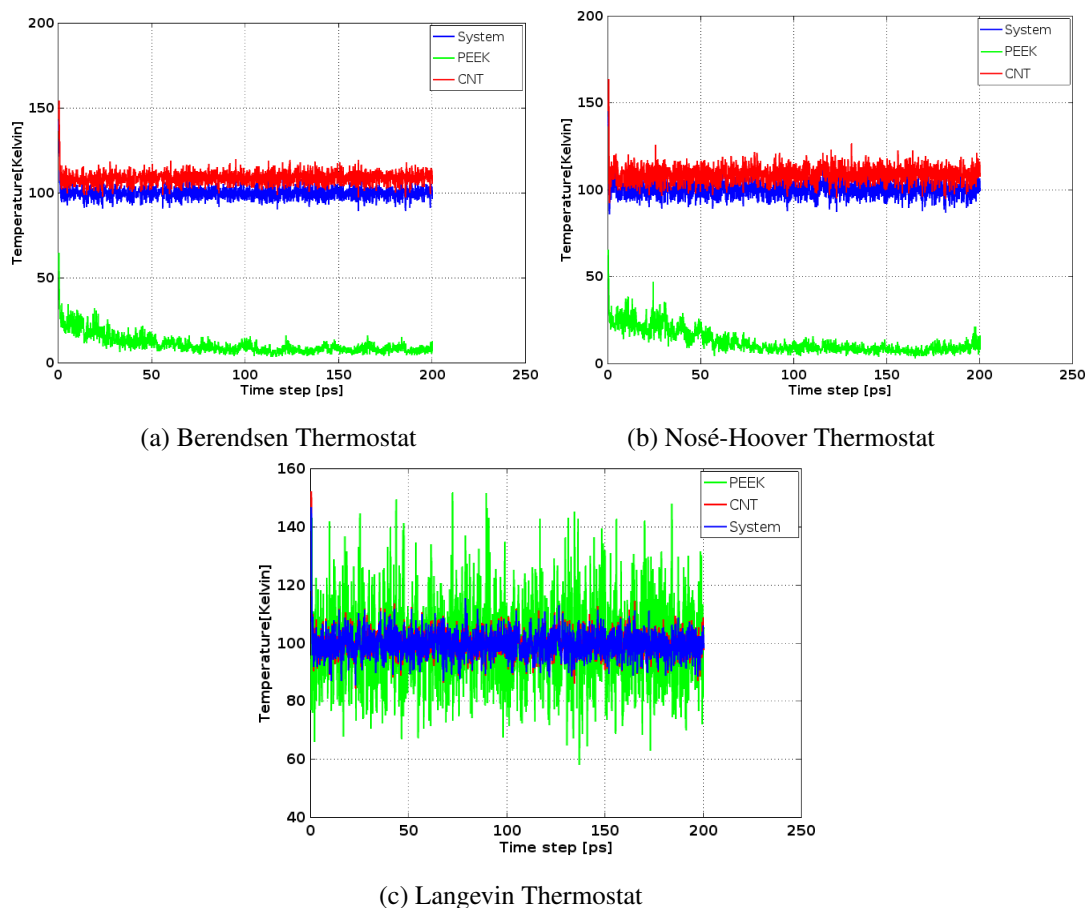
Figure 5.14: Temperatures of the system (shown with blue lines), CNT (with red lines) and PEEK monomer (with green lines)

In most of the studies concerning CNT and polymer interfaces, CNT is kept fixed during simulation due to its very small changes during simulation [97]. Since we have faced a temperature decrease in PEEK polymer during simulations, we also tested this protocol by treating atoms of CNT as frozen and compare with our previous results. This protocol guarantees that the molecule always remains at the target temperature with the payoff being that the CNT is effectively kept at zero. The results for the frozen CNT case are given in following Tables 5.9 and 5.10.

According to these results, a decrease in the adsorption energies are observed with respect to the previous protocol. However, the agreement with DFT results are still very good. In this case, only adsorption in the Mode 1 configuration is observed. Apart

Table 5.9: Adsorption energies (in eV) of full PEEK monomer on (10,0) zigzag fixed CNT with different lengths

L_{CNT}	DFT	ReaxFF		
		T=0K	T=100K	T=300K
13.05	-1.3518	-1.4207	-1.3184	-1.0292
21.75	-1.2743	-1.3548	-1.2549	-1.3265
26.01	-1.2841	-1.3520	-1.3946	-1.3864

Table 5.10: Comparison of the interaction energies of full PEEK monomer on fixed CNTs with different radius calculated with DFT and MD techniques

	DFT	ReaxFF		
		T=0K	T=100K	T=300K
(10,0)	-1.2841	-1.3520	-1.3946	-1.3864
(12,0)	-1.3745	-1.4527	-1.4666	-1.0924
(15,0)	-1.4145	-1.5477	-1.4882	-1.4210
(6,6)	-1.3702	-1.4022	-1.4673	-1.2171
(7,7)	-1.555	-1.4844	-1.3615	-1.3949
(8,8)	-2.111	-1.5182	-1.5179	-1.2048

from this observation, we conclude that the new protocol does not yield qualitative results that are significantly different from the previous protocol for the single PEEK monomer.

5.3.2 CNT/PEEK Wrapping

Various experimental [90, 91] and MD studies [95, 96, 97] reported the non-covalent wrapping of polymer chains around CNTs in literature. For polymers that have aromatic rings in their backbone, π-π stacking is the driving force [93]. After comparing the DFT and MD results of CNT/sub-molecule and CNT/PEEK monomer adsorption energies, we move on to study adsorption of the PEEK polymer with longer chain

lengths. We again used the 3, 6 and 9-monomer PEEK chains as shown before in Figure 4.5 and 4.24. In these calculations, we repeated the same protocol in the single PEEK monomer calculations. Just the simulation time is increased from 200 ps to 400 ps due to increase in the system size. Adsorption energies are calculated from snapshots taken every 10 ps during the last 100 ps. Adsorption energy versus time graphs are produced using the 10 adsorption energy results obtained in this way.

5.3.2.1 CNT and 3-monomer PEEK chain

First, 3-monomer length PEEK chain, created via random walk based configurational bias Monte Carlo option, was placed on top of a 10 nm long (8,8) armchair CNT as shown in Figure 5.15. In literature, armchair type CNTs have been reported to be preferable for reinforcement [92].

(a) side view   (b) front view
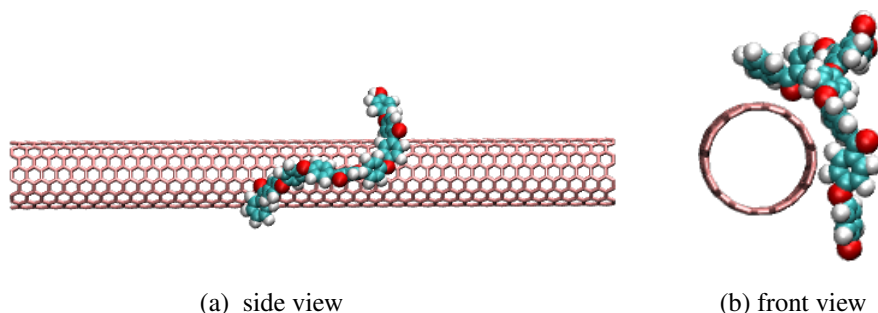
Figure 5.15: Initial configuration of 3-monomer PEEK on CNT (a) side view and (b) front view

Adsorption energies were calculated at three different temperatures 1K, 100K and 300K by using the MD protocol mentioned above as unfixed CNT case. Adsorption geometries and energies are given in Figure 5.16. As can be seen from these figures, aromatic rings of PEEK placed parallel to the CNT as a consequence of π-π stacking and result in higher adsorption energies as in Table 5.12.

T=1K (side view)　　　　　　　　　　T=1K (front view)

T=100K (side view)　　　　　　　　　T=100K (front view)

T=300K (side view)　　　　　　　　　T=300K (front view)
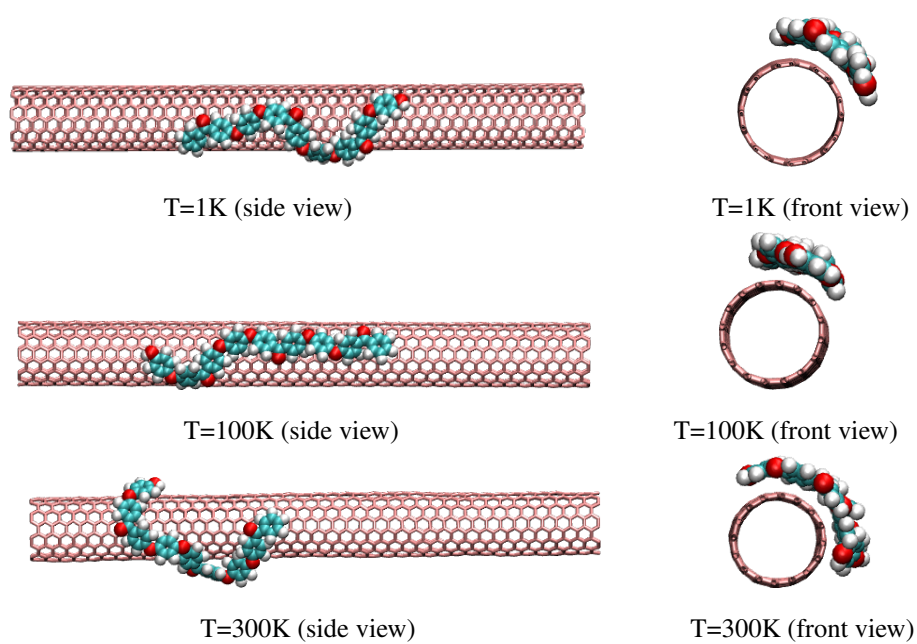
Figure 5.16: Final configurations of 3-monomer PEEK chain at different temperatures
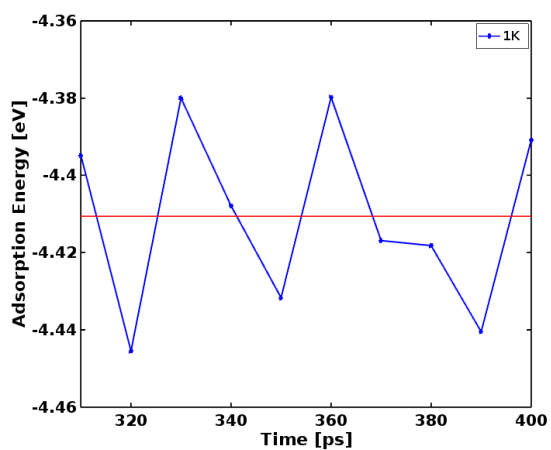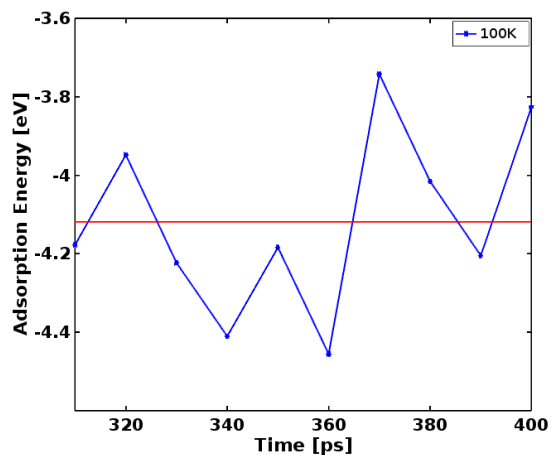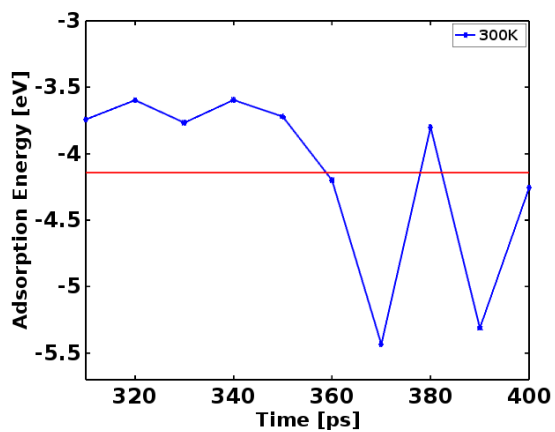
Figure 5.17: Adsorption energy graphs of 3-monomer PEEK chain on CNT at (a) 1 K, (b) 100 K and (c) 300 K. Blue lines show the 10 data and red lines are their averaged values.

5.3.2.2   CNT and 6-monomer PEEK chain

We continued our investigations by increasing repeat units of PEEK from three to six monomers. The PEEK chain was placed on CNT as shown in Figure 5.18.

t=0 ps (side view)   t=0 ps (front view)
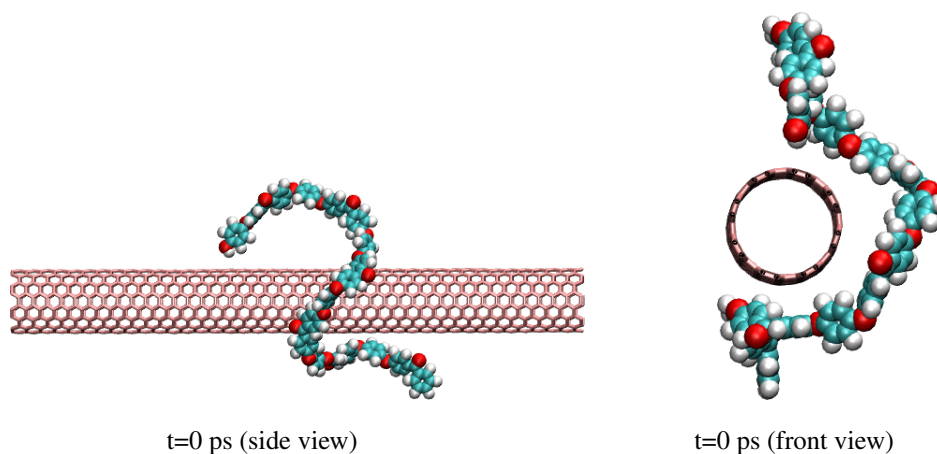
Figure 5.18: Initial configuration of 6-monomer PEEK on CNT

In this case, increase in the chain length yields more wrapped geometry around CNT. At 100 K temperature, PEEK chain fully wrapped around CNT as in Figure 5.19 and resulted with the highest adsorption energy.

Similarly to the case of the single monomer, two separate protocols (fixed and un-fixed) were both used. For the case of 6 -monomer PEEK at 300 K, apart from these two procedures, we tested another protocol by controlling temperature of CNT and PEEK components separately. In this case, CNT and PEEK both are at the temperature of 300 K. Final geometries of 6-monomer PEEK on top of CNTs using these 3 different procedures is given in Figure 5.21 and their adsorption energies is given in Table 5.11.

In Figure 5.21, it can be seen that when CNT is kept fixed, PEEK chain does not fully wrap around CNT. There is an interchain coiling in this case that causes a decrease in the adsorption energy. Rather than full wrapping, coiling of polymer chains is reported in literature as well [97]. Instead of interacting with surface of CNT, intramolecular interactions of polymer chains dominate causing lower adsorption energies.

89
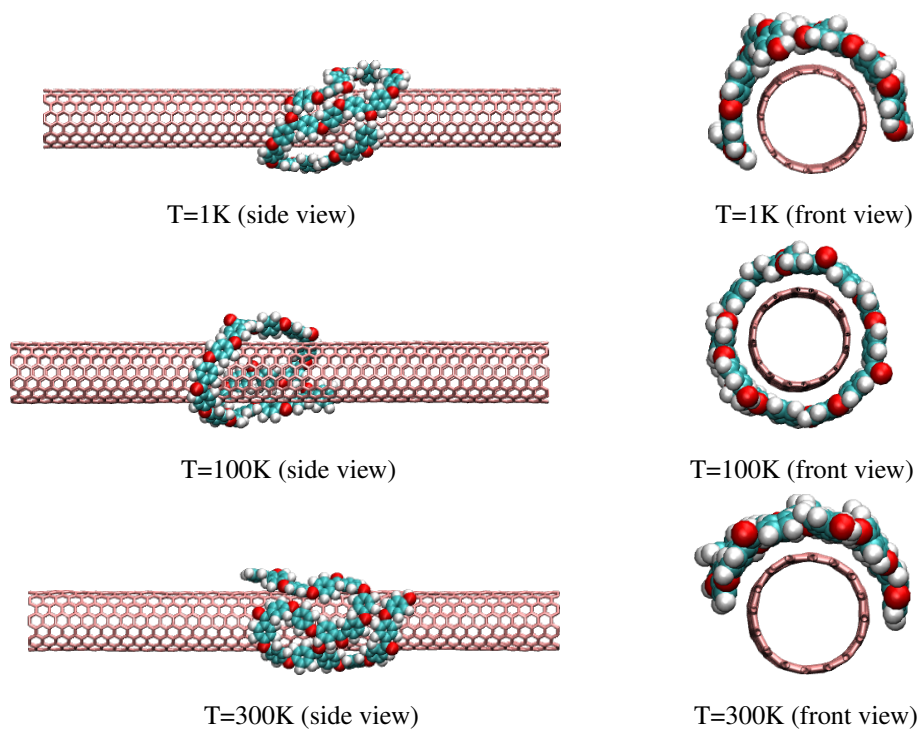
Figure 5.19: Final configurations of 6-monomer PEEK on CNT at 1K, 100K and 300K

Table 5.11: Comparison of the adsorption energies of 6-monomer PEEK calculated with three different protocols

	6-PEEK		
	Unfixed	Fixed	Heated separately
E_a	-7.5572	-5.4523	-6.0809
E_a/monomer	-1.2595	-0.9087	-1.0135
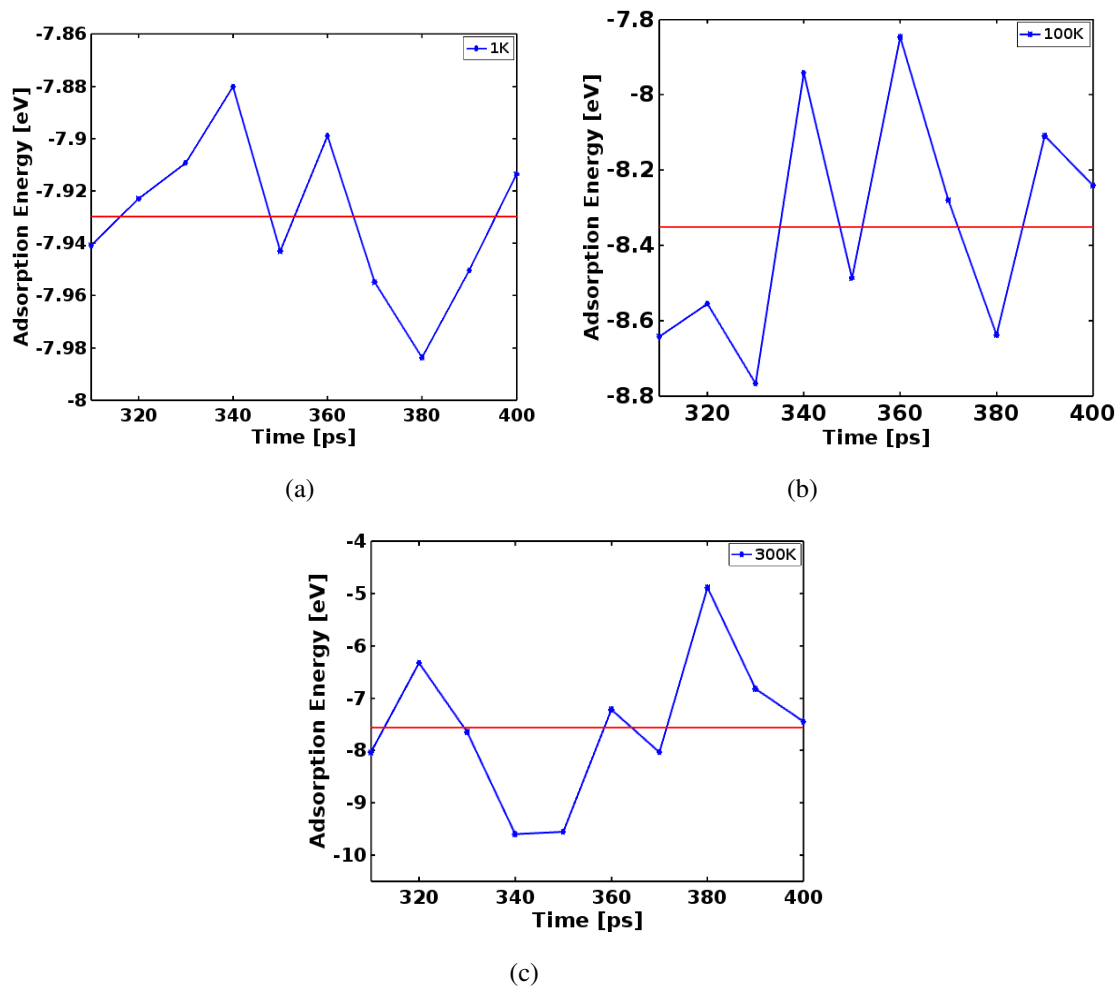
Figure 5.20: Adsorption energy graphs of 6-monomer PEEK chain on CNT at 1 K, 100 K and 300 K. Blue lines show the 10 data and red lines are their averaged values.

CNT fixed (side view)　　　　　　CNT fixed (front view)

Separately heated (side view)　　　Separately heated (front view)
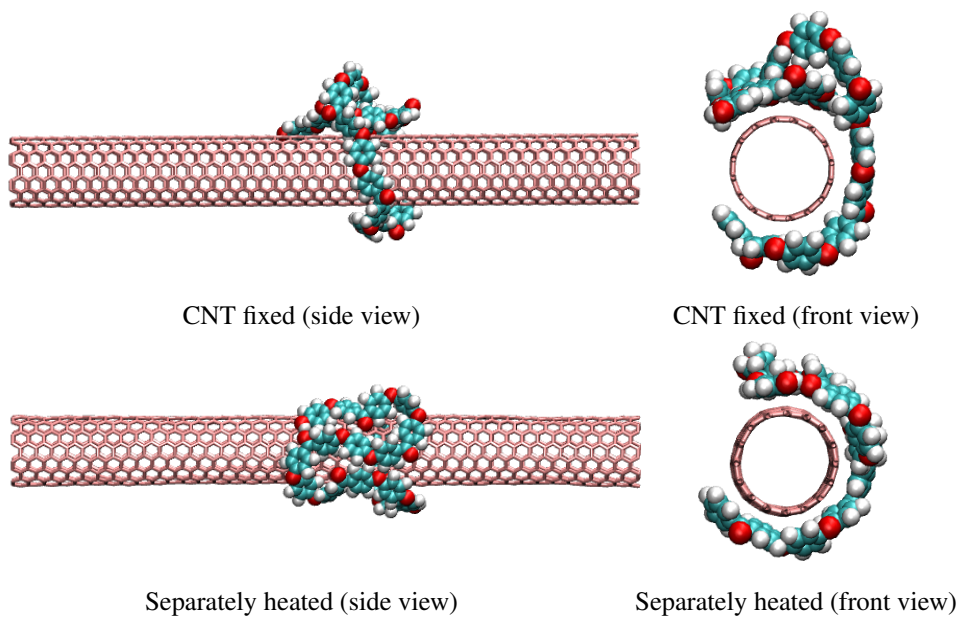
Figure 5.21: 300 K final configurations of 6-monomer PEEK chain on CNT when CNT is fixed and system is separately heated

5.3.2.3 CNT and 9-monomer PEEK chain

Finally, 9-monomer PEEK chain was placed on (8,8) CNT and was subjected to an MD process. Full wrapping of PEEK chain was observed most likely encouraged by the already somewhat wrapped initial configuration.

(a) side view   (b) front view
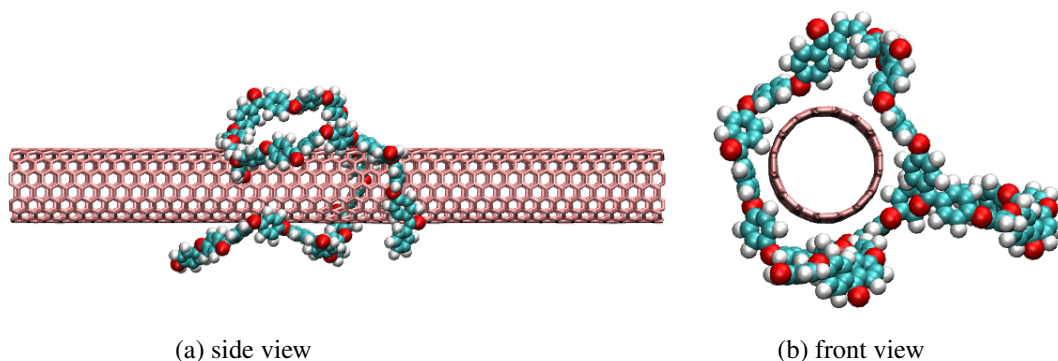
Figure 5.22: Initial configuration of 9-monomer PEEK chain on top of CNT

The results obtained in this subsection are summarized in Table 5.12. As seen in this table, the adsorption energies generally follow an increasing trend with increasing polymer length. This dependence trivially arises from the increasing contact area. A more adequate comparison can be made by considering the adsorption energies per monomer. As the length of the polymer increases, the self-coiling rate is also increased. As such, the fraction of aromatic chains (or equivalently atoms) in direct contact with the CNT decreases. These calculations fail to identify a concrete trend as a function of temperature.

T=1K (side view)　　　　　　　　　T=1K (front view)

T=100K (side view)　　　　　　　　T=100K (front view)

T=300K (side view)　　　　　　　　T=300K (front view)
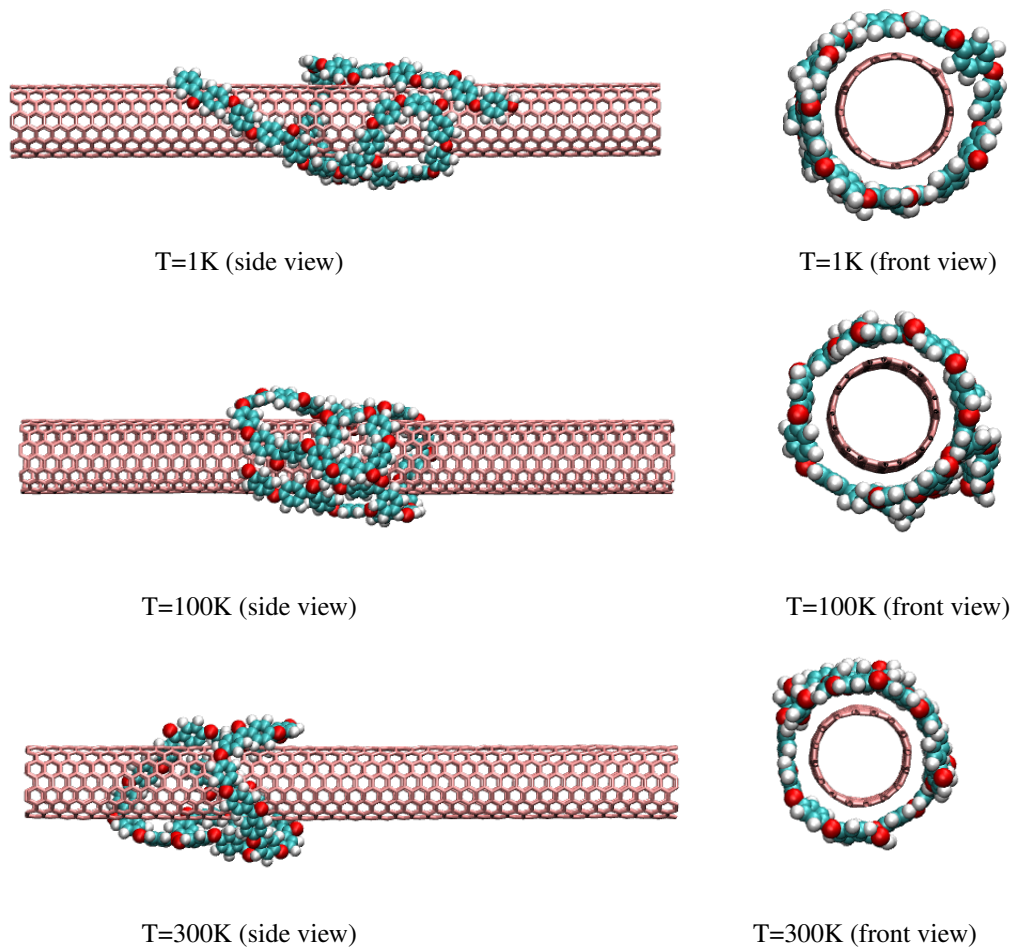
Figure 5.23: Final configurations of 9-monomer PEEK chain on CNT at 1K, 100K and 300K temperatures

Table 5.12: Average adsorption energies (in eV) and adsorption energies per monomer of 3, 6 & 9-monomer PEEK chain on (8,8) armchair CNT with 10 nm length at 1K, 100K & 300K

	CNT/3-PEEK	CNT/6-PEEK	CNT/9-PEEK
Temperature	E_a & E_a/monomer	E_a & E_a/monomer	E_a & E_a/monomer
T=1K	-4.4106 / -1.4702	-7.9298/ -1.3216	-11.0467/ -1.2274
T=100K	-4.1186 / -1.3728	-8.3505 / -1.3917	-10.8717 / -1.2079
T=300K	-4.1421 / -1.3807	-7.5572 / -1.2595	-11.5565/ -1.2840
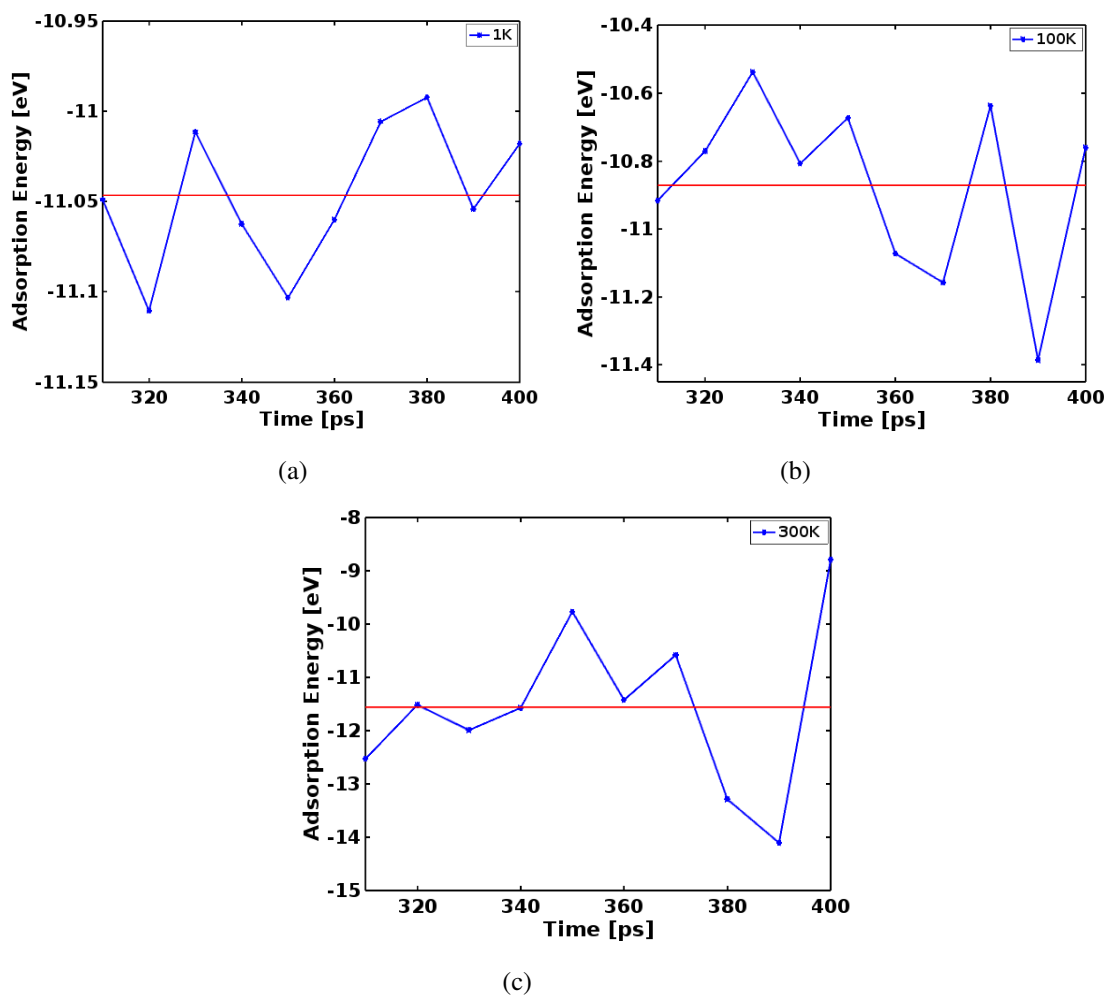
Figure 5.24: Adsorption energy graphs of 9-monomer PEEK chain on CNT at 1 K, 100 K and 300 K. Blue lines show the 10 data and red lines are their averaged values.

5.3.2.4 Rod-like PEEK Chains

During our calculations so far, it came to our attention that the final configuration of the polymer was heavily influenced by the initial configuration. As a means of lowering the bias towards wrapped configurations, we test a set of different initial configurations. In addition to 3, 6 and 9-monomer PEEK chains created via configurational MC option, we studied rod-like PEEK chains on top of (8,8) CNT. For these cases, we placed the chains on CNT with three different angles $0°$, $45°$ and $90°$ respectively. The schematic representation of initial configuration is given in Figure 5.25. This time, the length of CNT is taken as 5 nm for 3-monomer PEEK , 10 nm for 6-monomer PEEK and 15 nm for 9-monomer PEEK. First, we once again tested
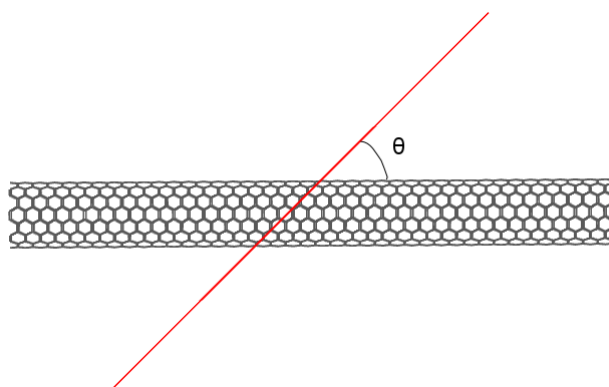
Figure 5.25: Schematic of initial configuration of rod-like PEEK chains on CNT

the fixed and unfixed protocols as described previously. Adsorption geometries are given in Figure 5.26 for comparison. The average adsorption energy was calculated as -4.55 eV for the fixed case and -10.29 eV for the other case. There is a significant difference between these two results. While interchain coiling of PEEK chain leads to a smaller degree of wrapping around CNT [97] when CNT is kept frozen, in the unfixed configuration, the polymer preferentially selects a larger extent of interfacial interaction. Since the assumption of fixing CNTs is widely preferred in literature to reduce computational cost and simplify the simulations [95] and we have faced with an artificial decrease in the temperature of PEEK during simulations, we present these final set of results by considering CNTs frozen in their original positions. The average adsorption energies for rod-like PEEK chains were calculated with this protocol and results are given in following Table 5.13.

96

(a) Fixed case   (b) Unfixed case
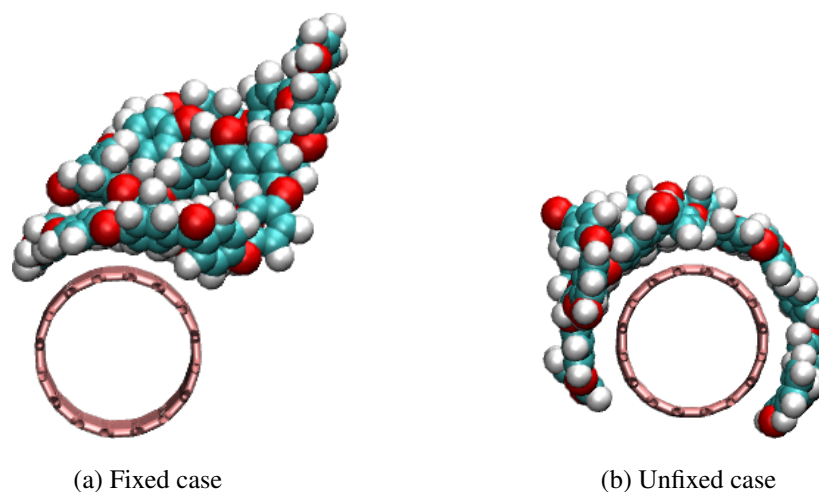
Figure 5.26: Final adsorption geometries (front views) of $45°$ rotated PEEK chain on CNT at T=100K

Table 5.13: Average adsorption energies (in eV) of rod-like PEEKs chain with different initials

	CNT/3-PEEK			CNT/6-PEEK			CNT/9-PEEK		
	$0°$	$45°$	$90°$	$0°$	$45°$	$90°$	$0°$	$45°$	$90°$
T=100K	-2.06	-1.44	-1.33	-3.35	-4.06	-5.09	-5.48	-4.56	-6.47
T=300K	-1.22	-1.36	-2.15	-3.20	-3.84	-5.99	-3.98	-4.49	-6.65

There is a significant decrease in the average adsorption energies of PEEK chains. According to our calculations, adsorption energies are clearly dependent on initial configuration of polymer. It is also observed that fixed CNTs increase interchain coiling in PEEK chains while decreasing the interaction of polymer and CNT. The coiled configurations of the chain found to be have significantly lower energy than the initial case, therefore, the chain prefers to found its lower energy configuration instead of interacting with the CNT.

CHAPTER 6

CONCLUSION

In this thesis, we investigated the interface between carbon nanotubes (CNTs) and an industrially important polymer, polyetheretherketone, abbreviated as PEEK. The motivation behind this study derives from the great interest in the use of carbon-based nanomaterials as reinforcing agents in polymer matrices. Since CNTs have remarkable mechanical properties, they are used very often for this purpose. Here, our main objective was to understand the interaction between CNT and PEEK to provide input for the development of their nanocomposites.

In Chapter 3, we studied the mechanical properties of various CNTs with Tersoff interatomic potential under static loading. We calculated a negative Poisson's ratio value for these CNTs, which is finding well documented in literature reported as a shortcoming of this potential [66]. Then, the mechanical properties were calculated with three different interatomic potentials developed for carbon systems namely AIREBO, $ReaxFF_{CHO}$ and $ReaxFF_{C2013}$. We found that $ReaxFF_{CHO}$ overestimates the Poisson's ratio of CNTs as also stated in literature [68]. Hence, we carried out our mechanical property investigations under dynamical loading with AIREBO and $ReaxFF_{C2013}$ potentials. For both Young's modulus and Poisson's ratio, good agreement was found with literature for these two potentials.

In Chapter 4, the Nosé-Hoover, Berendsen and Langevin thermostats were tested on isolated PEEK chains of three different lengths together with the two versions of the ReaxFF potential namely $ReaxFF_{CHO}$ and ReaxFF-lg. These benchmark studies were conducted to identify the most suitable thermostat and potential to be used in further calculations. In these simulations, performed in vacuum, we encountered

the so-called the flying ice cube artifact when we use the Nosé-Hoover and Berendsen thermostats. We prevented this artifact by demanding that the center of mass linear and angular momentum be zero. This option is readily available in the code suite used here, namely LAMMPS. Two important properties that give information about polymer chains namely end-to-end distance and radius of gyration were investigated during these simulations which were used to assess the degree of folding of the polymer chains. Based on the analysis of the results of this portion, the remaining calculations were carried out using the ReaxFF-lg version together with the Berendsen thermostat which is mostly widely used temperature control scheme used in the ReaxFF studies.

Finally, in Chapter 5, we investigated the interaction between CNT and PEEK with both DFT and MD techniques. Our interface calculations began by dividing the PEEK monomer into its sub-units and analyzing the interaction between these sub-units and CNT. The purpose of this preliminary study was to understand the driving forces between adsorption geometries of the full monomer by looking at the details of the π-π interaction with each aromatic ring and the CNT. Following this stage, the adsorption energies of PEEK monomer on different CNTs were calculated by using the ReaxFF-lg potential at 0 K temperature and the results showed very good agreement with the DFT results by proving the accuracy of the ReaxFF potential. We then continued the interface studies by examining the non-covalent wrapping mechanism of PEEK around CNT. We used two different protocols when calculating adsorption energies of PEEK chains. We adopted the common practice of keeping the CNT fixed during our calculations. For these calculations, we have found that the adsorption energies depend on the initial configuration of the polymer on CNT. For the two protocols that we use, there is a noteworthy difference in the adsorption energies due to different interaction mechanisms of the CNT and the polymer observed in these two cases.

REFERENCES

[1] Novoselov K. S., Geim A. K., Morozov S. V., Jiang D., Zhang Y., Dubonos S. V., Grigorieva I V., Firsov A. A., Electric field effect in atomically thin carbon films, *Science*, 306, 666–669 (2004)

[2] Iijima S., Helical Microtubules of Graphitic Carbon, *Nature*, 354, 56-58 (1991)

[3] Scarselli M., Castrucci P. and Crescenzi M.D, Electronic and optoelectronic nano-devices based on carbon nanotubes, *J.Phys.Condens.Matter*, 24, 313202 (2012)

[4] Bianco A., Kostas K., Maurizio P., Applications of carbon nanotubes in drug delivery, *Curr. Opin. Chem. Biol.*, 9, 6, 674-679 (2005)

[5] Fan S., Chapline M., Franklin N., Tombler T.W., Cassell A., Dai H., Self-oriented regular arrays of carbon nanotubes and their field emission properties, *Science*, 283, 5401, 512-514 (1999)

[6] Saito Y., Uemura S., Field emission from carbon nanotubes and its application to electron sources, *Carbon*, 38, 2, 169-182 (2000)

[7] Mittal G.,Dhand V., Rheea K.Y., Park S-J., Lee W.R., A review on carbon nanotubes and graphene as fillers in reinforced polymer nanocomposites, *Journal of Industrial and Engineering Chemistry*, 21, 11-25 (2015)

[8] Balandin A.A., Suchismita G., Wenzhong B., Irene C., Desalegne T., Feng M. and Chun NL., Superior Thermal Conductivity of Single-Layer Graphene , *Nano Letters*, 8, 3, 902–907 (2008)

[9] Novoselov K., Geim AK., Morozov S., Jiang D., Katsnelson M., Grigorieva I., et al. Two-dimensional gas of massless Dirac fermions in graphene, *Nature*, 438, 197-200 (2005)

[10] Potts J.R., Dreyer D.R., Bielawski C.W., and Ruoff Rodney R.S., Graphene-based Polymer Nanocomposites, *Polymer*, 52, 5-25 (2011)

[11] Wang X., Zhi L., Müllen K., Transparent, conductive graphene electrodes for dye-sensitized solar cells, *Nano Letters*, 8, 1, 323–327 (2008)

[12] Miao X., Tongay S., Petterson MK., Berke K., Rinzler AG., Appleton BR., et al. High efficiency graphene solar cells by chemical doping, *Nano Letters*, 12, 6, 2745–2750 (2012)

[13] Gohardani O., Elola M.C., Elizetxea C., Potential and prospective implementation of carbon nanotubes on next generation aircraft and space vehicles: A review of current and expected applications in aerospace sciences, *Progress in Aerospace Sciences*, 70, 42-68 (2014)

[14] Lee C., Wei X., Kysar J.W., Hone J., Measurement of the elastic properties and intrinsic strength of monolayer graphene, *Science*, 321, 385-388 (2008)

[15] Jiang J-W., Wang JS., and Li B., Young's modulus of graphene: A molecular dynamics study, *Phys.Rev.B*, 80, 113405 (2009)

[16] Meador M.A., Nanotechnology Roadmap Technology Area 10, *NASA*, (2012)

[17] Kis A., Zettl A., Nanomechanics of carbon nanotubes, *Phil. Trans. R. Soc. A*, 366, 1870 (2008)

[18] Choudhary V. and Gupta A., Carbon Nanotubes - Polymer Nanocomposites, Dr. Siva Yellampalli (Ed.), ISBN: 978-953-307-498-6, InTech (2011)

[19] Treacy M.M.J., Ebbesen T.W., Gibson J.M., Exceptionally high Young's modulus observed for individual carbon nanotubes, *Nature*, 381 (1996)

[20] Wong E.W., Sheehan P.E., Liebert C.M., Nanobeam Mechanics: Elasticity, Strength, and Toughness of Nanorods and Nanotubes, *Science*, 277 (1997)

[21] Yakobson B. I., Brabec C. J. and J. Bernholc, Nanomechanics of carbon tubes: Instabilities beyond linear response, *Physical Review Letters*, 76, 14 (1996)

[22] Brydson J.A. , Plastic Materials, 7th Edition, *Butterworth-Heinemann*, 604-606 (1999)

[23] Callister W.D.Jr., Materials Science and Engineering: An Introduction, 7th Edition, *John Wiley & Sons. Inc.*, 577-601 (2007)

[24] Pisani W.A., Radue M., Chinkanjanarot S., Klimek-McDonald D.R., Tomasi J.M., King J.A. and Odegard G., Predicting Thermo-Mechanical Properties of PEEK using Reactive Molecular Dynamics, *Proceeding of American Society for Composites*, 31st Technical Conference (2016)

[25] Born M. and Oppenheimer R., Zur quantentheorie der molekeln, *Ann.Phys*, 84:457 (1927)

[26] Hohenberg W. and Kohn W., Inhomogenous electron gas, *Phys. Rev.*, 136, B864 (1964)

[27] Kohn W. and Sham L.J., Self-consistent equations including exchange and correlation effects, *Phys.Rev.*, 140, 1133 (1965)

[28] Berland K., Cooper V.R., Lee K., Schröder E., Thonhauser T., Hyldgaard P. and Lundqvist B., van der Waals forces in density functional theory: a review of the vdW-DF method, *Reports on Progress in Physics*, 78, 6, 066501 (2015)

[29] Hepburn J., Scoles G. and Penco R., A Simple but Reliable Method for the Prediction of Intermolecular Potentials, *Chem. Phys. Lett.*, 36, 451 (1975)

[30] Ahlrichs R., Penco R. and Scoles G., Intermolecular Forces in Simple Systems, *Chem. Phys.*, 19, 119 (1977)

[31] Grimme S., Antony J., Ehrlich S., Krieg H., A consistent and accurate ab initio parametrization of density functional dispersion correction(dft-d) for the 94 elements h-pu, *J.Chem.Phys*, 132, 154104 (2010)

[32] Cooper V., van der Waals density functional: An appropriate exchange functionals, *Phys.Rev.B*, 21, 161104 (2010)

[33] Giannozzi P. et al., Quantum Espresso: a modular and open-source software project for quantum simulations of materials, *J.Phys.Condens.Matter*, 21, 395502 (2009)

[34] Allen M.P, Introduction to Molecular Dynamics Simulation, *Computational Soft Matter: From Synthetic Polymers to Proteins*, John von Neumann Institute for Computing Lecture Notes, NIC Series, 23, 1-28 (2004)

[35] Meller J., Molecular Dynamics, *Encyclopedia of Life Sciences* (2001)

[36] Dilrukshi K.G.S., Dewapriya M.A.N., Puswewala U.G.A., Size dependency and potential field influence on deriving mechanical properties of carbon nanotubes using molecular dynamics, *Theoretical and Applied Mechanics Letters*, 5, 167-172 (2015)

[37] Tserpesa K.I. and Papanikosa P., Finite element modeling of single-walled carbon nanotubes, *Composites: Part B* , 36, 468-477 (2005)

[38] Meo M. and Rossi M., Prediction of Young's modulus of single wall carbon nanotubes by molecular-mechanics based finite element modeling, *Composites Science and Technology*, 66, 1597-1605 (2006)

[39] Odegard G.M., Gates T.S., Wise K.E. , Park C., Siochi E.J., Constitutive modeling of nanotube–reinforced polymer composites, *Composites Science and Technology*, 63, 1671-1687 (2003)

[40] Rahmat M. and Hubert P., Carbon nanotube–polymer interactions in nanocomposites: A review, *Composites Science and Technology*, 72, 72-84 (2011)

[41] Verlet L., Computer Experiments on Classical Fluids. I. Thermodynamical Properties of Lennard-Jones Molecules, *Physical Review*, 159: 98-103 (1967)

[42] Frenkel D. and Smit B., Understanding molecular simulation from algorithms to applications, *Academic Press* (2002)

[43] Mylvagaham K. and Zhang L.C., Important issues in a molecular dynamics simulation for characterizing the mechanical properties of carbon nanotubes, *Carbon*, 42, 2025-2032 (2004)

[44] Finnis, M., Interatomic Forces in Condensed Matter. *Oxford University Press* (2003)

[45] Nosé S., A molecular dynamics method for simulations in the canonical ensemble, *Molec. Phys.*, 52, 255-268 (1984)

[46] Hoover W., Canonical dynamics: Equilibrium phase-space distributions, *Phys. Rev.*, A31, 1695-1697 (1985).

[47] Zhao Y., Brief introduction to the thermostats, Research Notes, `https://home.gwu.edu/~yxzhao/ResearchNotes/ResearchNote007Thermostat.pdf`. Last accessed on 26 July 2018

[48] Berendsen H. J. C., Postma J. P. M., van Gunsteren W. F., DiNola A., and Haak J. R., Molecular dynamics with coupling to an external bath, *J. Chem. Phys.*, 81, 8, 3684-90 (1984)

[49] Plimpton S., Fast Parallel Algorithms for Short-Range Molecular Dynamics, *J. Comp. Phys.*, 117, 1-19 (1995)

[50] Harvey S. C., Tan R. K-Z. and Cheatham III T. E., The flying ice cube: Velocity rescaling in molecular Dynamics leads to violation of energy equipartition, *Journal of Computational Chemistry*, Vol.19, No.7, 726-740 (1998)

[51] Andersen H. C. , Molecular dynamics simulations at constant pressure and/or temperature, *J. Chem. Phys*, 72, 2384 (1980)

[52] Jones J. E., On the determination of molecular fields.—I. From the variation of the viscosity of a gas with temperature, *The Royal Society Publishing*, 106, 738 (1924)

[53] Jones J. E., On the determination of molecular fields. —II. From the equation of state of a gas, *The Royal Society Publishing*, 106, 738 (1924)

[54] Tersoff J., New empirical approach for the structure and energy of covalent systems, *Physical Review B*, 37, 12 (1988)

[55] Tersoff J., Empirical Interatomic Potential for Carbon, with Applications to Amorphous Carbon, *Phys. Rev. Lett*, 61, 2879 (1988)

[56] Stuart J. S, Tutein A. B., Harrison A. J., A reactive potential for hydrocarbons with intermolecular interactions, *The Journal of Chemical Physics*, 112, 14 (2000)

[57] Brenner D. W., Shenderova O. A, Harrison J. A, Stuart S. J., Ni B., Sinnott S. B., A second-generation reactive empirical bond order (REBO) potential energy expression for hydrocarbons, *J Physics: Condensed Matter*, 14, 783-802 (2002)

[58] van Duin A. C. T., Dasgupta S., Lorant F., and Goddard III W. A., ReaxFF: A Reactive Force Field for Hydrocarbons, *Phys. Chem. A*, 105, 9393-9409 (2001)

[59] Chenoweth K., van Duin A. C. T., and Goddard, III W.A. , ReaxFF Reactive Force Field for Molecular Dynamics Simulations of Hydrocarbon Oxidation, *J. Phys. Chem. A* , 112, 1040-1053 (2008)

[60] Zhao H., Min K. and Aluru N. R., Size and chirality dependent elastic properties of graphene nanoribbons under uniaxial tension, *Nano Lett.*, 9, 8, 3012-3015 (2009)

[61] Srinivasan S.G., van Duin A.C. T., and Ganesh P., Development of a ReaxFF Potential for Carbon Condensed Phases and Its Application to the Thermal Fragmentation of a Large Fullerene, *J. Phys. Chem. A*, 119, 571-580 (2015)

[62] Liu L., Yi Liu, Zybin S.V, Sun H. and Goddard III W. A., ReaxFF-lg: correction of the ReaxFF reactive force field for london dispersion, with applications to the equations of state for energetic materials, *J. Phys. Chem. A*, 115, 11016-11022 (2011)

[63] Senftle T.P et al., The ReaxFF reactive force-field: development, applications and future directions, *npj Computational Materials*, 2, 15011 (2016)

[64] Liew K. M., He X. Q. and Wong C. H., On the study of elastic and plastic properties of multi-walled carbon nanotubes under axial tension using molecular dynamics simulation, *Acta Mater*, 52, 9, 2521-2527 (2004)

[65] Hernandez E., Goze C., Bernier P. and Rubio A., Elastic Properties of C and $B_x C_y N_z$ Composite Nanotubes, *Physical Review Letters*, 80, 20, 4502-4505 (1998)

[66] Kiselev S. P. and Zhirov E. V., Molecular dynamics simulation of deformation and fracture of graphene under unaxial tension, *Phys. Mesomech.*, 16, 1-8 (2013)

[67] Deb Nath S. K. and Kim S-G., Study of the Nanomechanics of CNTs under Tension by Molecular Dynamics Simulation Using Different Potentials, *ISRN Condensed Matter Physics*, Article ID 606017 (2014)

[68] Jensen B. D., Wise K. E. and Odegard G. M., Simulation of the Elastic and Ultimate Tensile Properties of Diamond, Graphene, Carbon Nanotubes, and Amor-

phous Carbon Using a Revised ReaxFF Parametrization, *J. Phys. Chem. A*, 119, 37, 9710-9721 (2015)

[69] Jensen B. D., Wise K. E. and Odegard G. M., The Effect of Time Step, Thermostat, and Strain Rate on ReaxFF Simulations of Mechanical Failure in Diamond, Graphene, and Carbon Nanotube, *Journal of Computational Chemistry*, 36, 1587-1596 (2015)

[70] Shima H., Buckling of Carbon Nanotubes: A State of the Art Review, *Materials*, 1-38 (2011)

[71] Feliciano J., Tang C., Zhang Y., Chen C., Aspect ratio dependent buckling mode transition in single-walled carbon nanotubes under compression, *Journal of Applied Physics*, 109, 084323 (2011)

[72] Wang C. M., Zhang Y. Y., Xiang Y., and Reddy J. N., Recent Studies on Buckling of Carbon Nanotubes, *Applied Mechanics Reviews*, 63, 030804 (2010)

[73] Pereira A. F. G., Fernandes J. V., Antunes J. M. and Sakharova N. A., Shear modulus and Poisson's ratio of single-walled carbon nanotubes: Numerical evaluation, *Phys. Status Solidi B*, 253, 2, 366–376 (2016)

[74] Rafiee R. and Moghadam R. M., On the modeling of carbon nanotubes: A critical review, *Composites B*, 56, 435-449 (2014)

[75] Wang Y., Wang X. X., and Ni X. G., Atomistic simulation of the torsion deformation of carbon nanotubes, *Modelling Simul. Mater. Sci. Eng.*, 12, 6, 1099-1107 (2004)

[76] Vijayaraghavan V. and Wong C. H., Torsional Characteristics of Single Walled Carbon Nanotube with Water Interactions by Using Molecular Dynamics Simulation, *Nano-Micro Lett.*, 6, 3, 268-279 (2014)

[77] Xiong Q. and Tian X.G., Torsional properties of hexagonal boron nitride nanotubes, carbon nanotubes and their hybrid structures: A molecular dynamics study, *AIP ADVANCES*, 5, 107215 (2015)

[78] Bialoskórski M. and Rybicki J., Mechanical Properties of Single-walled Carbon Nanotubes Simulated with AIREBO Force-Field, *Comp. Methods in Sci. and Tech.*, 18, 2, 67-77 (2012)

[79] Huang X., Yang H., van Duin A. C. T., Hsia K. J., Zhang S., Chemomechanics control of tearing paths in graphene, *Phys.Rev.B*, 85, 195453 (2012)

[80] Hu W., Polymer Physics A Molecular Approach, *Springer* (2013)

[81] Madhavan K., Zentner L., Farnsworth V., Shivarajapura S., Zentner M., Denny N. and Klimeck G., nanoHUB.org: Cloud-based Services for Nanoscale Modeling, Simulation, and Education, *Nanotechnology Reviews*, 2, 1, 107–117 (2013)

[82] Osuji C., Ideal Chain Conformations and Statistics, *ENAS 606:Polymer Physics, week 2 handouts*, `https://www.eng.yale.edu/polymers/docs/classes/polyphys/lecture_notes/2/handout2.pdf` . Last accessed on 11 July 2018

[83] Lindenmeyer P. H , Why Do Polymer Molecules Fold? , *Polymer Engineering and Science*, 14, 6 (1974)

[84] Rahmat M. , Carbon Nanotube-Polymer Interaction in Nanocomposites, *Ph.D thesis*, McGill University-Montreal (2011)

[85] Singh P., Campidelli S., Giordani S., Bonifazi B., Bianco A., Prato M., Organic functionalization and characterisation of single-walled carbon nanotubes, *Chem. Soc.Rev.*, 124, 5, 760–761 (2002)

[86] Jilili J., Abdurahman A., Gülseren O., Schwingenschlögl U., Non-covalent functionalization of single wall carbon nanotubes and graphene by a conjugated polymer, *Appl. Phys. Lett.*, 105, 013103 (2014)

[87] Tasis D., Tagmatarchis N., Bianco A., and Prato M., *Chem Rev.*, 106, 1105 (2006)

[88] Zaminpayma E., Mirabbaszadeh K., Interaction between single-walled carbon nanotubes and polymers: A molecular dynamics simulation study with reactive force field, *Comp. Mat. Sci.*, 58, 7-11 (2012)

[89] Senftle T. P., Hong S., Islam M. M., Kylasa S. B., Zheng Y., Shin Y. K., Junkermeier C., Engel-Herbert R., Janik M. J., Aktulga H. M. et al. The ReaxFF reactive force-field: development, applications and future directions, *Computational Materials*, 2, 15011 (2016)

[90] Dohi H., Kikuchi S., Kuwahara S., Sugai T., Shinohara H., Synthesis and spectroscopic characterization of single-wall carbon nanotubes wrapped by glycoconjugate polymer with bioactive sugars, *Chem. Phys. Lett* 428, 98-101 (2006)

[91] Yi W., Malkovskiy A., Xu Y., Wang X. Q, Sokolov A. P., Colon M. L., Meador M. A., Pang Y., Polymer conformation-assisted wrapping of single-walled carbon nanotube: The impact of cis-vinylene linkage, *Polymer*, 51, 475-481 (2010)

[92] Chen H., Xue Q., Zheng Q., Xie J., Yan K., Influence of Nanotube Chirality, Temperature, and Chemical Modification on the Interfacial Bonding between Carbon Nanotubes and Polyphenylacetylene, *J. Phys Chem. C*, 112, 16514–16520 (2008)

[93] Karnati K. R, Wang Y., Understanding the co-loading and releasing of doxorubicin and paclitaxel using chitosan functionalized single-walled carbon nanotubes by molecular dynamics simulation, *Phys. Chem. Chem. Phys*, 20, 9389–9400 (2018)

[94] Yang M., Koutsos V. and Zaiser M., Interactions between Polymers and Carbon Nanotubes: A Molecular Dynamics Study, *J.Phys.Chem.B*, 109, 10009-10014 (2005)

[95] Rouhi S., Alizadeh Y., Ansari R., On the interfacial characteristics of polyethylene/single-walled carbon nanotubes using molecular dynamics simulations, *Applied Surface Science*, 292, 958-970 (2013)

[96] Foroutan M. and Nasrabadi A.T., Investigation of the Interfacial Binding between Single-Walled Carbon Nanotubes and Heterocyclic Conjugated Polymers, *J.Phys.Chem.B*, 114, 5320-5326 (2010)

[97] Tallury S. S. and Pasquinelli M. A., Molecular Dynamics Simulations of Flexible Polymer Chains Wrapping Single-Walled Carbon Nanotubes, *J. Phys. Chem*, 114, 4122-4129 (2010)